

Atomic probe tomography and creep deformation studies of highly dynamic metallic systems: copper-zirconium based metallic glass alloys and tin-based alloy



A Dissertation Submitted in Partial Fulfillment of the Requirements
for the Degree of Doctor of Engineering in Metallurgical and Materials Engineering

Department of Metallurgical Engineering

Faculty of Engineering

Chulalongkorn University

Academic Year 2018

Copyright of Chulalongkorn University

การศึกษาของระบบโลหะที่มีพลวัตด้วยเทคนิคอะตอมมิกโพรบโทโมกราฟีและการแปรรูปแบบ
คืบ: โลหะผสมอสถุฐานที่มีทองแดงและเซอร์โคเนียมเป็นส่วนประกอบและโลหะผสมดีบุก



วิทยานิพนธ์นี้เป็นส่วนหนึ่งของการศึกษาตามหลักสูตรปริญญาวิศวกรรมศาสตรดุษฎีบัณฑิต
สาขาวิชาวิศวกรรมโลหการและวัสดุ ภาควิชาวิศวกรรมโลหการ
คณะวิศวกรรมศาสตร์ จุฬาลงกรณ์มหาวิทยาลัย
ปีการศึกษา 2561
ลิขสิทธิ์ของจุฬาลงกรณ์มหาวิทยาลัย

Thesis Title Atomic probe tomography and creep deformation studies
of highly dynamic metallic systems: copper-zirconium
based metallic glass alloys and tin-based alloy

By Miss Chetarpa Yipyintum

Field of Study Metallurgical and Materials Engineering

Thesis Advisor Assistant Professor Boonrat Lohwongwatana, Ph.D.

Accepted by the Faculty of Engineering, Chulalongkorn University in Partial
Fulfillment of the Requirement for the Doctor of Engineering

..... Dean of the Faculty of Engineering
(Professor SUPOT TEACHAVORASINSKUN, Ph.D.)

DISSERTATION COMMITTEE

..... Chairman
(Assistant Professor Mawin Supradist na ayudhaya, Ph.D.)

..... Thesis Advisor
(Assistant Professor Boonrat Lohwongwatana, Ph.D.)

..... Examiner
(Associate Professor TACHAI LUANGVARANUNT, Ph.D.)

..... Examiner
(Associate Professor PATAMA VISUTTIPITUKUL, Ph.D.)

..... External Examiner
(Associate Professor Jessada Wannasin, Ph.D.)

เชษฐอำภา ยิบยิณธรรม : การศึกษาของระบบโลหะที่มีพลวัตด้วยเทคนิคอะตอมมิกโพรบโทโมกราฟีและการแปรรูปแบบคืบ: โลหะผสมอสัณฐานที่มีทองแดงและเซอร์โคเนียมเป็นส่วนประกอบและโลหะผสมดีบุก. (Atomic probe tomography and creep deformation studies of highly dynamic metallic systems: copper-zirconium based metallic glass alloys and tin-based alloy) อ.ที่ปรึกษาหลัก : ผศ. ดร.บุญรัตน์ โล่ห์วงศ์วัฒน์

ศึกษากระบวนการตกผลึกของโลหะผสมอสัณฐานที่มีทองแดงและเซอร์โคเนียมเป็นส่วนประกอบด้วยกล้องจุลทรรศน์อิเล็กตรอนแบบส่องผ่านและเทคนิคอะตอมมิกโพรบโทโมกราฟี มีการวิเคราะห์โครงสร้างจุลภาคด้วยวิธีต่างๆเพื่อศึกษาผลขององค์ประกอบทางเคมี การวางตัวของอะตอมในระยะสั้นหลังจากผ่านกระบวนการอบในเครื่องตีฟอเรนเซี่ยลสแกนนิ่งแคลอริมิเตอร์ในชั้นบรรยากาศอาร์กอน การเรียงตัวของอะตอมในระบบโลหะผสมอสัณฐานที่แตกต่างกันนั้นมีความสำคัญต่อการศึกษาโครงสร้างจุลภาคและคุณสมบัติของวัสดุ การวิเคราะห์โครงสร้างจุลภาคที่มีความแตกต่างน้อยนั้นมีความยุ่งยากเนื่องจากผลของการเตรียมชิ้นงานก็สามารถส่งผลให้เกิดสิ่งแปลกปลอมในโครงสร้าง การเลือกตัวแปรในกระบวนการเตรียมชิ้นงานนั้นจึงส่งผลต่อโครงสร้าง โดยเฉพาะโลหะผสมอสัณฐานที่มีทองแดงและเซอร์โคเนียมเป็นส่วนประกอบที่ง่ายต่อการเกิดออกไซด์ ในการเตรียมชิ้นงานด้วยลำแสงไอออนที่เน้นเฉพาะจุดทำให้สามารถศึกษาออกไซด์บนผิวของวัสดุได้ ถึงแม้จะใช้พลังงานไอออนที่ต่ำร่วมกับแท่นวางชิ้นงานที่ระบบความเย็นด้วยไนโตรเจนเหลวก็ยังสามารถพบออกไซด์ได้

ศึกษาเปรียบเทียบการแปรรูปแบบคืบของโลหะผสมดีบุกด้วยการทดสอบแรงดึงและเครื่องกดในระดับนาโน (Nanoindentation) เพื่อหากลไกการแปรรูปและสมการการคืบ และสามารถนำมาประยุกต์ใช้อธิบายกระบวนการขัดผิวได้ การศึกษานี้คือเน้นให้เกิดความเข้าใจระบบโลหะที่มีพลวัต เช่น โลหะที่มีจุดหลอมเหลวต่ำและโลหะอสัณฐาน เพื่อนำไปประยุกต์ใช้ได้หลากหลายอุตสาหกรรม

จุฬาลงกรณ์มหาวิทยาลัย
CHULALONGKORN UNIVERSITY

สาขาวิชา วิศวกรรมโลหการและวัสดุ
ปีการศึกษา 2561

ลายมือชื่ออนิสิต
ลายมือชื่อ อ.ที่ปรึกษาหลัก

5671410221 : MAJOR METALLURGICAL AND MATERIALS ENGINEERING

KEYWORD: Metallic glass, atom probe tomography, creep deformation, tin based alloy, Cu-Zr

Chetarpa Yipyintum : Atomic probe tomography and creep deformation studies of highly dynamic metallic systems: copper-zirconium based metallic glass alloys and tin-based alloy. Advisor: Asst. Prof. Boonrat Lohwongwatana, Ph.D.

The early crystallization process of a Cu-Zr binary metallic glass was investigated by transmission electron microscopy (TEM) and atomic probe tomography (APT). The microstructural analysis was carried out using different characterization methods to see if the phase separation in different chemical compositions and chemical short-range orders were investigated by applying heat treatment under argon atmosphere in differential scanning calorimetry (DSC) chamber. Such a difference in the atomic arrangement of a given amorphous metallic structure is important, the actual characterization of such small difference is not practically easy. For the reason that there is an effect of the sample preparation method which could lead to a misinterpreted of the observation since it could cause artifacts. The selection of a appropriate sample preparation method is important in direct observation of the artifact-free amorphous microstructure, since Cu-Zr binary metallic glass is promptly oxidized and hydrogenated. By prepared the sample using focus ion beam scanning electron microscope (FIB-SEM) and ion milling, oxide and hydride contamination on the sample could observe. Even the low-energy ion milling with liquid nitrogen cooling without careful measured parameters of TEM and APT could also create oxide and hydride of the alloys.

Creep deformation of Sn-1 wt% Bi was studied and compared by conventional tensile creep and nanoindentation creep. The mechanisms corresponding to creep behavior were demonstrated from the two techniques. The creep equation was able to explain the lapping process parameters. The objective of this study is to understand highly dynamic metallic system such as low melting point alloy and metallic glass alloy. This could be further applied and explained in wide range of applications.

Field of Study: Metallurgical and Materials
Engineering

Student's Signature

Academic Year: 2018

Advisor's Signature

ACKNOWLEDGEMENTS

I would like to express my deepest appreciation to Associate Professor Dr. Boonrat Lohwangwatana for his continuous support, patient, advice and encouragement. Working under him has given me the opportunity to many new doors. There were many things that I could have learned and gained from him. Thank you for the opportunity to visit and work in renown labs at Northwestern University as well as Korea Institute of Science and Technology (KIST).

I would like to extend my gratitude to Prof. David N. Seidman, Prof. David Dunand and Prof. Jin-Yoo Suh for research collaborations, discussions and encouragement. I would like to thanks my thesis committee; Assoc. Prof. Dr. Mawin Supradist Na Ayudhaya, Assist. Prof. Dr. Tachai Laungvaranunt, Assist. Prof. Dr. Patama Visutti pitukul and Assist. Prof. Dr. Jessada Wannasin for spending the time on this thesis and the thesis defense.

I would like to acknowledge many magnificent and delightful people who make my PhD experience an exceptional and memorable one - Thanawat Phetrattanarangsi, Siri Nittayakasetwat, Punn Augsornworawat, Warakarnt Jaturasil, Pachara-on Srikajorn, Dr. Dieter Isheim, Dr. Sung-II Baik, Dong An, Anthony De Luca, Ha-Young Kim, Min-Gu Jo, Han-Jin Kim, Julien Fadonougbo, and Dr. Hye Jung Chang.

Lastly, a special thank you to my parents, my brother and my sister for always supporting me both physically and emotionally throughout my PhD journey. I thank my friends – Chane Surasondhi, Daocharad Burana, Leelada Rattanavija, Time Tuangsintanakul and Chinchai Udomtarak.

This thesis work is financially supported by the Thailand Research Funding (TRF) and Western digital corporation through Research and Researchers for Industries (RRI) fund.

Chetarpa Yipyintum

TABLE OF CONTENTS

	Page
ABSTRACT (THAI).....	iii
ABSTRACT (ENGLISH)	iv
ACKNOWLEDGEMENTS.....	v
TABLE OF CONTENTS.....	vi
LIST OF TABLES.....	ix
LIST OF FIGURES.....	x
Chapter 1 Introduction	1
1.1 Background and Significant of the Research Problem.....	1
1.2 Objectives.....	2
1.3 Scope of Project	2
1.4 Expected Benefits	2
Chapter 2 Literature Reviews	4
2.1 Cu-Zr based metallic glasses	4
2.2 Tin-based alloy	7
2.3 Atom Probe Tomography (APT)	10
2.3.1 Electropolishing	12
2.3.2 Focus Ion Beam (FIB) method.....	13
2.4 Creep deformation.....	14
2.4.1 Thermal cycling creep	17
2.5 Nanoindentation	18
2.5.1 Shape of Nanoindentation's tip	22

2.5.2	Limitations and factors affecting nanoindentation	23
2.6	Nanoindentation Creep	25
Chapter 3 Atomic arrangement evolution of binary Cu-Zr based metallic glass		29
3.1	Study of atomic diffusion	29
3.1.1	Methodology	29
3.1.2	Result and discussion.....	31
3.1.3	Conclusion	48
3.2	Kinetic Study of Binary Cu-Zr metallic glasses.....	49
3.2.1	Methodology	51
3.2.2	DSC scans on different locations of melt spun ribbons	53
3.2.3	Shear strain rate in melt spinning and planar flow casting (PFC)....	57
3.2.4	Temperature dependent kinetic (Isochronal transformation).....	58
3.2.5	Time dependent kinetic (Isothermal transformation).....	61
3.2.6	Conclusions	66
3.3	Observation of hydrogen artefacts during sample preparation and atomic probe tomography.....	67
3.3.1	Results and Discussion	68
3.3.2	Conclusions	73
Chapter 4 Creep deformation investigation on tin-based alloys		75
4.1	Physical property of lapping plate	75
4.1.1	Microstructure of Sn-Bi alloy.....	75
4.1.2	Anisotropic property of lapping plate.....	81
4.2	Mechanical property of lapping plate	83

4.2.1	Micro-Vicker Hardness measurement.....	83
4.2.1.1	Effect of varying hold time.....	83
4.2.1.2	Effect of varying applied load.....	84
4.2.1.3	Effect of different composition of Sn.....	85
4.2.2	Nanoindentation.....	86
4.3	Conventional Creep.....	98
4.3.1	Isothermal Creep.....	99
4.3.2	Thermal Cycling Creep.....	101
4.4	Nanoindentation creep.....	105
4.4.1	Methodology.....	105
4.4.2	Results and Discussion.....	106
Chapter 5	Applications of atomic diffusion in lapping process.....	113
5.1	Evolution of abrasive particles on lapping plate during charging process.....	115
5.2	Evolution of lapping plate during lapping process.....	116
5.3	Lapping plate model.....	128
5.4	Model Validation.....	130
Chapter 6	Conclusion.....	132
Chapter 7	Appendix.....	134
REFERENCES	144
VITA	157

LIST OF TABLES

	Page
Table 3.1: Specific transition temperature of $\text{Cu}_{64}\text{Zr}_{36}$, $\text{Cu}_{56}\text{Zr}_{44}$ and $\text{Cu}_{50}\text{Zr}_{50}$	31
Table 3.2: Chemical composition of $\text{Cu}_{64}\text{Zr}_{36}$, $\text{Cu}_{56}\text{Zr}_{44}$, and $\text{Cu}_{50}\text{Zr}_{50}$ at different heat treatment temperature	33
Table 3.3: Glass transition temperature, T_g and crystallization temperatures, T_c of amorphous $\text{Cu}_x\text{Zr}_{100-x}$ alloys of different processing history were reported in various values as obtained from DSC experiments	50
Table 3.4: The hydrogen contents of $\text{Cu}_{56}\text{Zr}_{44}$ nanotips prepared by cryogenic stage FIB and conventional FIB (all numbers are expressed in atomic weight)	71
Table 4.1: Dimension of creep specimen following ASTM E8 standard	99
Table 4.2: Stress exponent, hardness and elastic modulus of Sn-1 wt% Bi at different temperature	110
Table 5.1: Measurement data of groove dimension	123
Table 5.2: Area fraction and average diamond size of ID, MD and OD from various processes	126
Table 6.1: Observed phase during devitrification under different techniques	133

LIST OF FIGURES

	Page
Figure 2.1: Time-temperature-crystallization curve (TTT-diagram) of general metallic glass	5
Figure 2.2: Phase diagram of Cu-Zr binary system [10]	7
Figure 2.3: Phase diagram of Sn-Bi binary alloy system [11].....	8
Figure 2.4: Microstructure of a) Sn-3 wt.% Bi b) Sn-10 wt.% Bi c) Sn-50 wt.% Bi d) Sn-57 wt.% Bi e) Sn-70 wt.% Bi [11].....	9
Figure 2.5: Schematic view of an Atomic probe tomography [12].....	11
Figure 2.6: a) Wire of metal in Cu-clamp b) Electropolishing.....	12
Figure 2.7: Lift out process a) removal of material around the interested area b) attachment of the Omniprobe	13
Figure 2.8: a) Atomic probe tip after shaping b) sample holder for Atomic probe.....	14
Figure 2.9: Stages of creep behavior.....	15
Figure 2.10: Load-displacement curves from nanoindentation of a) eutectic Sn-Bi b) Sn-3 wt.% Bi c) Pure Bi at three strain rates [13]	17
Figure 2.11: P is applied load, h is indenter displacement, h_p is plastic deformation after load removal and h_e is the surface displacement at the contact perimeter [18]	18
Figure 2.12: Schematic steps of typical indentation experiment [18]	19
Figure 2.13: a) Relationship between indentation stress and indentation strain for spherical indenter. b) Schematic development of plastic region [19]	20
Figure 2.14: Load-displacement curve for Berkovich indenter on fused silica. Also included with the calculated and measured value from nanoindentation [20]	21
Figure 2.15: Schematics of indenter tips [18].....	22

Figure 2.16: a) TEM of Berkovich indenter tip b) High-magnification SEM scan of Berkovich indenter tip c) Schematic of indenter geometry [18, 19].....	22
Figure 2.17: a) TEM of piling-up on Berkovich indenter tip b) sided view of piling-up c) Top view of piling-up d) TEM of sinking-in e) Sided view of sinking-in f) Top view of sinking-in [18].....	25
Figure 3.1: X-ray diffraction traces of the as-receive Cu-Zr binary metallic glass ribbons	32
Figure 3.2: Thermal behavior of amorphous Cu-Zr binary alloys	32
Figure 3.3: Reconstructed volume at different temperatures with compositions of a) $\text{Cu}_{64}\text{Zr}_{36}$, b) $\text{Cu}_{56}\text{Zr}_{44}$, and c) $\text{Cu}_{50}\text{Zr}_{50}$. The left column shows the superimposed of all major elements	35
Figure 3.4: Atomic concentration of ZrH, H, ZrO and O in a) $\text{Cu}_{50}\text{Zr}_{50}$ b) $\text{Cu}_{56}\text{Zr}_{44}$ c) $\text{Cu}_{64}\text{Zr}_{36}$ at different annealing temperatures	36
Figure 3.5: Frequency distribution functions of a) $\text{Cu}_{64}\text{Zr}_{36}$, b) $\text{Cu}_{56}\text{Zr}_{44}$, and c) $\text{Cu}_{50}\text{Zr}_{50}$ metallic glass ribbon at different heat treatment temperature.....	39
Figure 3.6: a) Reconstructed volume of $\text{Cu}_{64}\text{Zr}_{36}$ annealed at T_2 b) Proximity histogram concentration profiles from selected volume of Cu cluster c) Proximity histogram concentration profiles from selected volume of ZrO cluster d) Proximity histogram concentration profiles from selected volume of Zr cluster e) Proximity histogram concentration profiles from selected volume of ZrH cluster.....	40
Figure 3.7: a) reconstructed APT of $\text{Cu}_{64}\text{Zr}_{36}$ b) TEM bright field of $\text{Cu}_{64}\text{Zr}_{36}$ c) EDS pattern of $\text{Cu}_{64}\text{Zr}_{36}$ d) HRTEM of $\text{Cu}_{64}\text{Zr}_{36}$ of the area enclosed in a box in b) and an inset is an FFT pattern of the Cu-rich region e) HRTEM of $\text{Cu}_{64}\text{Zr}_{36}$ of the Zr-rich region and an inset is an FFT pattern of the corresponding area.....	41
Figure 3.8: Poxigram of reconstructed volume of $\text{Cu}_{64}\text{Zr}_{36}$ annealed at 823 K a) Proximity histogram concentration profiles from selected volume of ZrO cluster b)	

Proximity histogram concentration profiles from selected volume of Sn cluster	c)
Proximity histogram concentration profiles from selected volume of ZrH cluster	42
Figure 3.9: a) Reconstructed volume of $\text{Cu}_{56}\text{Zr}_{44}$ annealed at T_2 with Proximity histogram concentration profiles from selected volume of ZrH cluster b) Reconstructed volume of $\text{Cu}_{56}\text{Zr}_{44}$ annealed at 823 K with Proximity histogram concentration profiles from selected volume of ZrO cluster and Proximity histogram concentration profiles from selected volume of ZrH cluster	44
Figure 3.10: a) reconstructed APT of $\text{Cu}_{56}\text{Zr}_{44}$ b) TEM bright field of $\text{Cu}_{56}\text{Zr}_{44}$ c) EDS pattern of $\text{Cu}_{56}\text{Zr}_{44}$ d) HRTEM of $\text{Cu}_{56}\text{Zr}_{44}$ of the area enclosed in a box 1 in b) and an inset is an FFT pattern of the corresponding area. e) HRTEM of $\text{Cu}_{56}\text{Zr}_{44}$ of the area enclosed in a box 2 in b) and an inset is an FFT pattern of the corresponding area	45
Figure 3.11: a) Reconstructed volume of $\text{Cu}_{50}\text{Zr}_{50}$ annealed at T_2 b) Proximity histogram concentration profiles from selected volume of ZrO cluster c) Proximity histogram concentration profiles from selected volume of ZrH cluster.....	46
Figure 3.12: a) reconstructed APT of $\text{Cu}_{50}\text{Zr}_{50}$ b) TEM bright field of $\text{Cu}_{50}\text{Zr}_{50}$ c) EDS pattern of the area enclosed in a box 1 in b) d) HRTEM of $\text{Cu}_{50}\text{Zr}_{50}$ of the area enclosed in a box 2 in c) and an inset is an FFT pattern of the corresponding area. e) HRTEM of $\text{Cu}_{50}\text{Zr}_{50}$ of the area enclosed in a box 3 in c) and an inset is an FFT pattern of the corresponding area	47
Figure 3.13: a) Schematic of melt spinning process with fluid flow in x and y directions with designated locations: (i) 2 mm away from the edge, (ii) midway between the edge and the center, and (iii) the center of the ribbon b) Side view schematic of spinning melt process at nozzle area (adapted from [65])	52
Figure 3.14: DSC heating curves from different locations of melt spun ribbons are displayed for the three Cu-Zr compositions: a) $\text{Cu}_{50}\text{Zr}_{50}$ b) $\text{Cu}_{56}\text{Zr}_{44}$ c) $\text{Cu}_{64}\text{Zr}_{36}$. The insets show the enlargement of region near T_g	55

Figure 3.15: Characteristic temperatures: glass transition temperature (T_g), onset temperature of crystallization (T_x), crystallization peak (T_c) of $\text{Cu}_{64}\text{Zr}_{36}$ and enthalpy change of crystallization (ΔH_c) against various heating rate were recorded from DSC isochronal experiments. Lines are used for guide.....	58
Figure 3.16: a) Calculation of activation energy for glass transition and crystallization of $\text{Cu}_{64}\text{Zr}_{36}$ using Kissinger Plot from T_g and T_c . b) Crystallized fraction curves as a function of temperature at different heating rates	60
Figure 3.17: a) Crystallization peaks during Isothermal heat treatment in DSC of $\text{Cu}_{64}\text{Zr}_{36}$ at different annealing temperatures. b) Isothermal temperature against incubated time under isothermal transformation	62
Figure 3.18: a) Calculation of activation energy for crystallization in isothermal annealing using Arrhenius equation. b) Crystallization fraction under different isothermal annealing temperature starting from the left at 783 K and decreasing at 5 K increment.	63
Figure 3.19: Johnson-Mehl-Avrami analysis at different annealing temperatures with crystallization fraction ranging from 0.2-0.8 under isothermal conditions.	65
Figure 3.20: $\text{Cu}_{64}\text{Zr}_{36}$ annealed at 770 K a) Atom probe reconstruction b) Concentration profile c) HAADF-STEM image.....	66
Figure 3.21: a) HRTEM image of $\text{Cu}_{64}\text{Zr}_{36}$ heat treated at 768 K prepared by FIB before running a LEAP experiment. b) TEM micrograph $\text{Cu}_{64}\text{Zr}_{36}$ annealed at 768 K prepared by FIB after running a LEAP experiment. c) FFT pattern obtained from the box shown in figure 1b. d) Reconstruction APT of $\text{Cu}_{64}\text{Zr}_{36}$ heat-treated at 768 K	69
Figure 4.1: Dimensional presentation of sample with directions: A as surface facet, B as longitudinal facet and C as cross-sectional facet.....	75
Figure 4.2: Average grain size in different direction and different area on the plate.....	76
Figure 4.3: LG Sn-1 wt.% Bi plate under optical microscope	77
Figure 4.4: SG Sn-1 wt.% Bi plate under optical microscope	77

Figure 4.5: EDS mapping area scan of SG Sn-1 wt.% Bi	78
Figure 4.6: Image of SG Sn-1 wt.% Bi plate under FE-SEM in BSE mode	78
Figure 4.7: EDS line scan of SG Sn-1wt.%Bi	78
Figure 4.8: EDS point scan of SG Sn-1 wt.% Bi	79
Figure 4.9: Image of LG Sn-1 wt.% Bi plate under FE-SEM in BSE mode	80
Figure 4.10: EDS point scan of LG Sn-1 wt.% Bi	80
Figure 4.11: XRD plot in arbitrary unit (A.U.)	82
Figure 4.12: Hardness value of Sn alloy with varying holding period (s)	83
Figure 4.13: Hardness value of Sn alloy with varying load (kgf)	84
Figure 4.14: Varying hold time in Micro Vicker Hardness test at 100 kgf	85
Figure 4.15: Varying loading force in Micro Vicker Hardness test	86
Figure 4.16: Load and displacement curve at different maximum load ranging from 10 to 400mN. Hold time and lodging rate were set as 20s and 4.5 mN/s respectively	87
Figure 4.17: Load-displacement curve at different loading rate ranging from 1 to 50mN/s. Hold time and lodging rate were set as 20s and 4.5 mN/s respectively	88
Figure 4.18: Calculated hardness from varying loading rate and strain rate	89
Figure 4.19: Calculated elastic modulus from varying loading rate and strain rate	90
Figure 4.20: Average hardness of a) SG Sn-1wt%Bi plate and b) LG Sn-1wt%Bi plate of different casting direction and region on the lapping plate	92
Figure 4.21: Average hardness of Sn-1 wt% Bi between small grain size sample (left-handed column) and large grain size sample (right-handed column) at inner diameter a) and d), middle diameter b) and e), and outer diameter c) and f)	93
Figure 4.22: Average reduced young modulus of a) SG Sn-1wt%Bi plate and b) LG Sn-1wt%Bi plate of different casting direction and regions on the lapping plate	95

Figure 4.23: Average reduced elastic modulus of Sn-1 wt% Bi between small grain size sample (left-handed column) and large grain size sample (right-handed column) at inner diameter a) and d), middle diameter b) and e), and outer diameter c) and f)	96
Figure 4.24: Creep frame	98
Figure 4.25: Creep specimen following ASTM E8 Standard	99
Figure 4.26: Creep behavior of forging Sn-1%Bi at 298, 343 and 393 K.....	100
Figure 4.27: Creep behavior of thermal cycling between 298 and 353 K of forging Sn-1 wt% Bi.....	102
Figure 4.28: Superimposed of creep data from isothermal experiment and thermal cycling experiment.....	102
Figure 4.29: Creep rate and reciprocal of the absolute temperature with activation energy from low stress and high stress region.....	103
Figure 4.30: Minimum strain rate against applied stress of LG Sn-1%Bi specimen at 343 and 393 K	104
Figure 4.31: Plot of minimum strain rate with a function of temperature	105
Figure 4.32: Calculated hardness and elastic modulus at different maximum load.....	107
Figure 4.33: Adjusted displacement against time during dwell period.....	108
Figure 4.34: Fitted function of $h(t) = h_i + a(t-t_i)^b + kt$ with dwell time	108
Figure 4.35: Strain rate as a function of stress at various temperature.....	109
Figure 4.36: Log strain rate against reciprocal temperature of Sn-1%Bi at 40 MPa.....	111
Figure 4.37: Superimposed of conventional creep and nanoindentation creep.....	112
Figure 5.1: System of lapping process	113
Figure 5.2: A 17-inch diameter experimental lapping plate	115
Figure 5.3: Evolution of diamond on lapping plate during charging process.....	115

Figure 5.4: Sn-1%Bi plate after facing, taken from optical microscope at 50X magnification b) topography of Sn-1%Bi plate after facing	117
Figure 5.5: Groove shaped of Sn-1%Bi plate after shaving from Profilometer	117
Figure 5.6: Sn-1%Bi plate after shaving taken from optical microscope with 50X magnification a) taken from inner diameter (ID) of lapping plate b) taken from middle diameter (MD) of lapping plate c) taken from outer diameter (OD) of lapping plate.....	118
Figure 5.7: Groove shaped of Sn-1%Bi plate after charging from Profilometer a) taken from inner diameter (ID) of lapping plate b) taken from middle diameter (MD) of lapping plate c) taken from outer diameter (OD) of lapping plate	119
Figure 5.8: Sn-1%Bi plate after charging taken from optical microscope with 50X magnification a) taken from inner diameter (ID) of lapping plate b) taken from middle diameter (MD) of lapping	119
Figure 5.9: Groove shaped of Sn-1%Bi plate after 1 HR lapping from Profilometer a) taken from inner diameter (ID) of lapping plate b) taken from middle diameter (MD) of lapping plate c) taken from outer diameter (OD) of lapping plate	120
Figure 5.10: Sn-1%Bi lapping plate after 10 bars lapping taken from optical microscope with 50X magnification a) taken from inner diameter (ID) of lapping plate b) taken from middle diameter (MD) of lapping plate c) taken from outer diameter (OD) of lapping plate	121
Figure 5.11: Groove depth of lapping plate after facing, shaving, charging and 1-hour lapping.....	121
Figure 5.12: Dimension of groove plate from ID, MD and OD.....	122
Figure 5.13: Roughness, Ra, of lapping plate	122
Figure 5.14: SEM image of lapping plate (MD) a) shaving b) charging c) 1-hour lapping	125
Figure 5.15: Diamond density on lapping plate.....	126

Figure 5.16: AFM scan of lapping plate after charging 127

Figure 5.17: AFM scan of lapping plate after 20 minutes of lapping 128

Figure 5.18: Plot of creep equation in a) low stress region and b) high stress region . 129

Figure 5.19: Diamond density with varied charging process parameter 131



Chapter 1

Introduction

1.1 Background and Significant of the Research Problem

One of the greatest challenges in materials development is to understand and comprehend the relationships between the processing, properties and its structure. The physical and mechanical properties due to the changes in the structure of materials are the main interested and concerned where diffusion play a crucial role. It is commonly known that it is thermally activated phenomenon where it is increased with temperature. Hence, the atoms in a material with high diffusion coefficient have greater tendency to move around. This would allow the phase transformation and deformation.

There are two types of dynamic metallic systems being investigated here. Tin-based alloy is considered a highly dynamic metallic system due to its low melting point. It has regained its attention in the past decades for solder application and microelectronics industry since lead-contained solder has been precluded in many industries due to its health issues. Sn-Bi alloys has gain interests due to its low processing temperature, good bonding properties with metal and comparable mechanical properties with lead-contained solder. The low Bi contents was being investigated since the Bi atoms could allow the improvement of mechanical property and creep resistance.

Metallic glasses have remarkable chemical, mechanical and physical properties. Composite of amorphous and crystalline have attracted considerable attention in order to gain most of its. They can be produced by partially crystallize the amorphous. This leads to better mechanical properties depending on the phase that was devitrified. The investigation of amorphous devitrification allows prediction and control phase stability. Cu-Zr binary system have great potentials since it is a good glass former and consists of various metastable and stable phases that could diversify property of the composite.

A fundamental investigation of the structure allows a better understanding of its properties. Atomic probe tomography (APT) was exploited for a direct observation of spatial atomic position. APT provides three-dimensional mapping of materials in atomic-scale resolution and information of the chemical composition and atomic structure.

In order to systematically applying and developing this atomic diffusion process in dynamic metallic system, understanding of the in-depth and fundamental of the process is significantly essential. The purpose of this thesis is mainly to understand highly dynamic metallic system. This study is emphasized on plastic deformation of tin-alloy and phase transformation of Cu-Zr metallic glasses. It is expected that this understanding could be used to explained various applications.

1.2 Objectives

1. Investigate plastic and creep deformation of tin alloy and relate to the understanding of atomic diffusion
2. Understand change in properties and relationship to phase transformation at different temperature
3. Able to explain the relationship between properties based on the engineering applications and fundamental knowledges such as atomic diffusion

1.3 Scope of Project

1. Literature reviews
2. Characterization of tin-based and copper-based alloys
3. Mechanical properties test of tin-based alloys

1.4 Expected Benefits

1. Understand in-depth analysis of atomic diffusion

2. Be able to apply this study into other type of industry
3. Be able to apply and relate between conventional technique and cutting-edge technique



Chapter 2

Literature Reviews

2.1 Cu-Zr based metallic glasses

Metallic glasses were discovered in 1960 by Duwez and Klement [1]. Metallic glasses also known as amorphous metals, have gained much attention due to its outstanding properties such as high yield strength, and excellent soft magnetic behavior [1]. This has opened new opportunities for numbers of applications [2]. The lack of crystallization leads to the absence of grain boundaries which allows better in resistant to corrosion and wear. They can be obtained by rapid cooling of the molten metal to the temperature below its melting point in order to avoid crystallization. The first metallic glass, $Au_{80}Si_{20}$ was undercooled at rate of 1×10^6 K/s [1]. Rather than forming a perfect crystal, the atoms do not have enough time and energy to rearrange themselves for nucleation and growth. Therefore, beyond the glass transition temperature, T_g , they usually further solidifies as metallic glass with amorphous structure. The undercooled process of metallic glass can be understood by considering time-temperature-crystallization curve as shown in figure 1. The curves indicate the time when crystallization start and finish if the liquid is undercooled under its melting point. The nose of the curve is the point of minimum time for crystallization to begin. As the temperature increases above the nose, the undercooling gets smaller and therefore takes longer time to begin crystallization. On the other hand, when the temperature is lowered below the nose, the viscosity of the liquid increases and leads to the longer time for crystallization. Accordingly, in order to avoid crystallization and obtain amorphous, cooling time must be lower than the time at which the nose is positioned. Numerous efforts have been done to lower the critical cooling rate of metallic glass which would in turn increase the critical casting thickness and therefore widen the applications. The larger size of metallic glasses usually refers to as bulk metallic glasses (BMG).

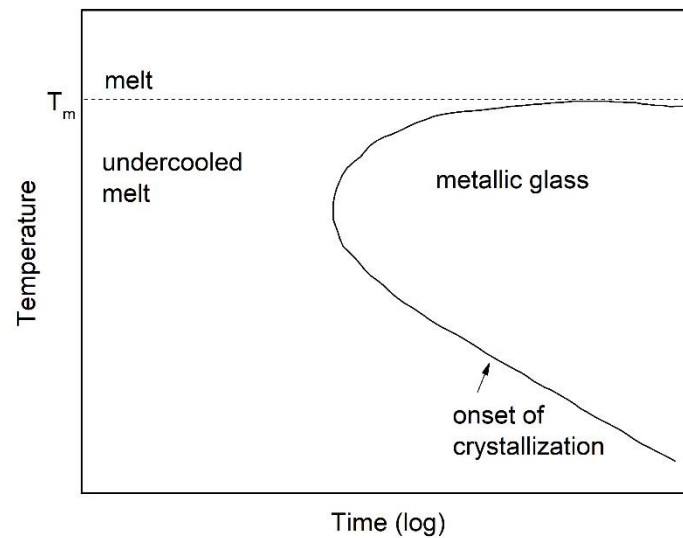


Figure 2.1: Time-temperature-crystallization curve (TTT-diagram) of general metallic glass

Metallic glasses also known as amorphous metals, have gained much attention over the past decades due to its outstanding properties such as high yield strength, and excellent soft magnetic behavior. Metallic glasses with a thickness larger than 1 mm are categorized as bulk metallic glasses (BMG). The crucial point that indicates ability of metallic glasses to form bulk metallic glasses is glass forming ability (GFA). GFA could be understand through thermal stability and crystallization kinetics in term of chemical short-range order. The discovery of BMG in binary systems alloys could provide important guidance to the finding and developing of new good BMG with good GFA. Moreover, BMG in simple binary systems alloys could lead to understanding of fundamental problems of BMG in that family alloys.

Binary Cu-Zr alloy system have been reported from computational simulation and physical experiments to be a material with outstanding properties and good structural stability [3]. They can be prepared by rapid quenching form the melt in a wide composition range especially between 30-70 at.% Zr composition [4-8]. This is because

of their difference in atomic size (Cu 0.128 nm and Zr 0.160 nm) which could obstruct the atomic diffusion to reach the phase-diagram stable phase. This allows the wide range of alloy compositions in binary Cu-Zr alloy system to form metallic glasses with wide variety of method such as splat quench and melt spinning. The best GFA with a two-mm critical casting thickness was $\text{Cu}_{64}\text{Zr}_{36}$ [7]. Crystallization of amorphous $\text{Cu}_{64}\text{Zr}_{36}$ leads to $\text{Cu}_{10}\text{Zr}_7$ and Cu_8Zr_3 as the final phases according to phase diagram of binary Cu-Zr system. $\text{Cu}_{51}\text{Zr}_{14}$ was suggested to be the early crystallization phase during the early stages of crystallization. Icosahedra concept were also proposed in the structure models for metallic glasses as a main building block. According to molecular dynamic (MD) simulation of binary Cu-Zr MG, Cu-centered icosahedra is suggested as the basic structural unit. During annealing of $\text{Cu}_{64}\text{Zr}_{36}$, Zr-centered CN16 Frank-Kasper polyhedral becomes the dominant local arrangement around Zr atoms, where the Cu-centered icosahedra start to be arranged themselves and formed Cu_2Zr . Alternatively, during cooling, the fraction of icosahedra correspondingly increases and forms icosahedral short-range order (SRO). In the case of $\text{Cu}_{64}\text{Zr}_{36}$, MD simulations shows its structure is full of network-like icosahedra where it would impede the nucleation and growth by stabilize the amorphous structure.

The atomic arrangements in binary Cu-Zr MG system were intensively studied using simulation methods and experimental methods such as high-energy X-ray diffraction, and neutron diffraction. The information on interatomic distances and coordination numbers were determined from the experiments. However, there are some drawback on this information, not only that they merely provide the information just for the first pair coordination, the complication of getting this information are proportionally increasing with the number of elements. Additionally, the relationships between the structure, thermodynamic properties and its characteristic temperature of many MG were successfully analyzed in a microscopic level.

The Cu-Zr binary system is one of the most extensively studied due to its simplicity and good glass forming ability. According to Cu-Zr phase diagram [9, 10],

there are eight intermetallic compounds in the system namely CuZr_2 , CuZr , $\text{Cu}_{10}\text{Zr}_7$, Cu_8Zr_3 , $\text{Cu}_{51}\text{Zr}_{14}$, Cu_5Zr , Cu_2Zr and Cu_5Zr_8 as shown in figure 2.2.

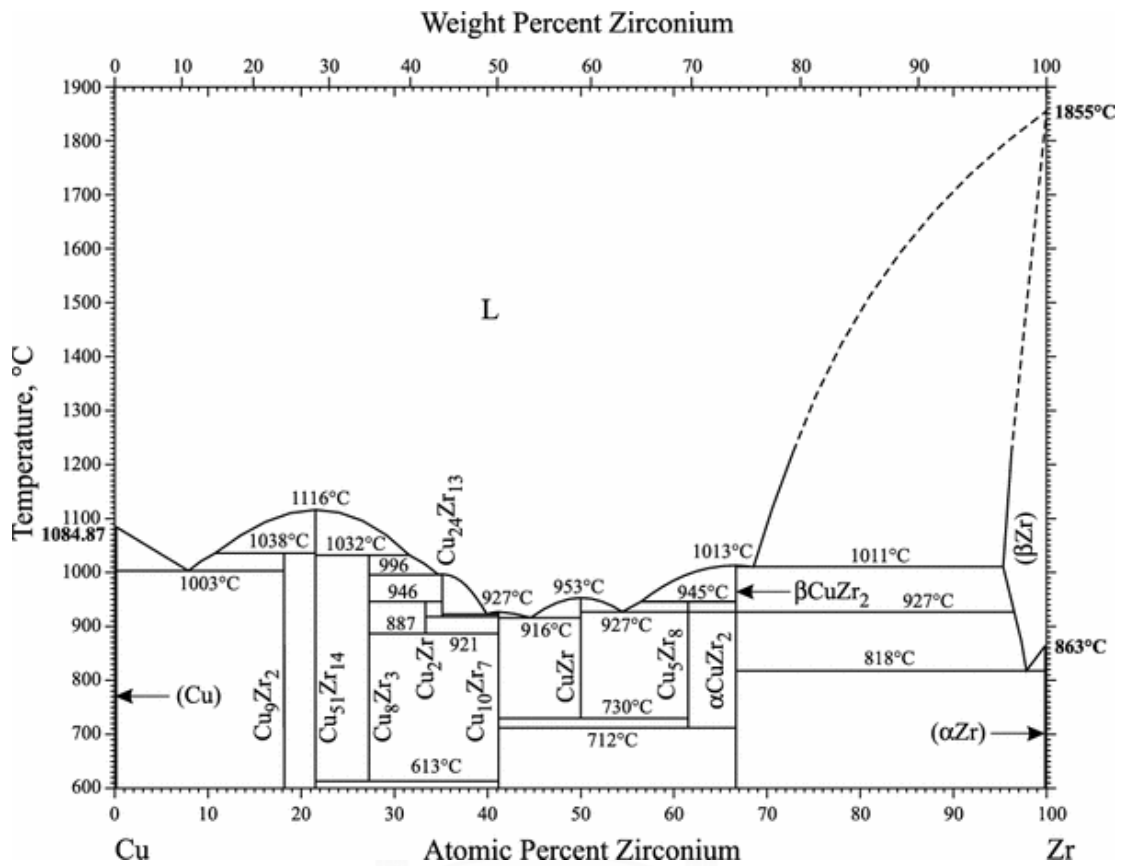


Figure 2.2: Phase diagram of Cu-Zr binary system [10]

CHULALONGKORN UNIVERSITY

2.2 Tin-based alloy

Tin is a malleable, ductile, and silvery-white metal with a symbol Sn. It is easily deformed under applied force. Under large strains, tin is regularly deformed in a form of slip and twinning in the crystals due to its low stacking fault energy. It is considered as a very low melting point metal with melting temperature of 286 °C. There are two allotropes of tin namely, α -tin and β -tin. α -tin is commonly known as gray tin. It is considered brittle compared to β -tin. It is stable at very low temperature. The latter one is commonly known as white tin. It is stable around room temperature. It is highly malleable and exists

in diamond cubic crystal structure. At low temperature, a large number of favorable oriented crystal structures are involved in slip process. Moreover, tin itself has high corrosion resistance because its oxide film protects it. It is often used in food containers industry. However, tin alloy can be employed in many ways such as solder in electric circuits.

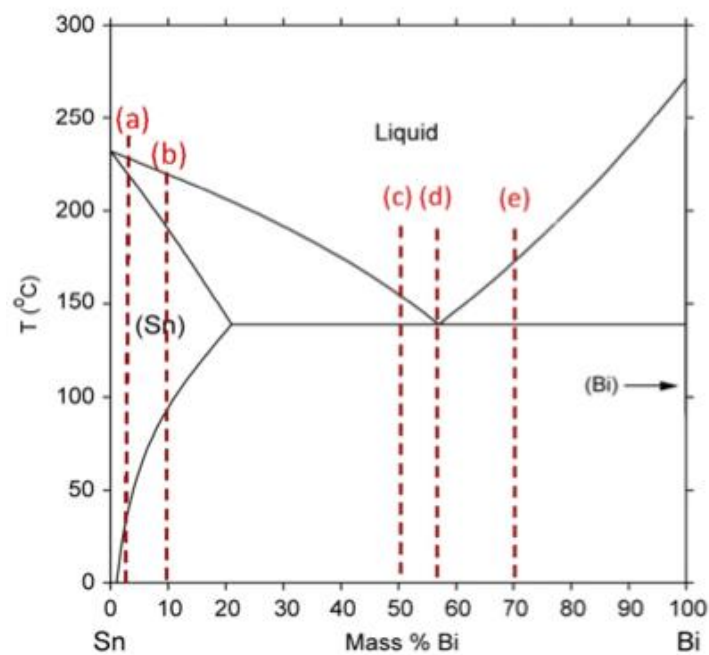


Figure 2.3: Phase diagram of Sn-Bi binary alloy system [11]

Tin-Bismuth (Sn-Bi) alloy has drawn attention over the past decade as it has been used in many solder joints applications due to its outstanding electrical and mechanical properties. Figure 2.3 and figure 2.4 show phase diagram of Sn-Bi alloy and its corresponding microstructure, respectively [11].

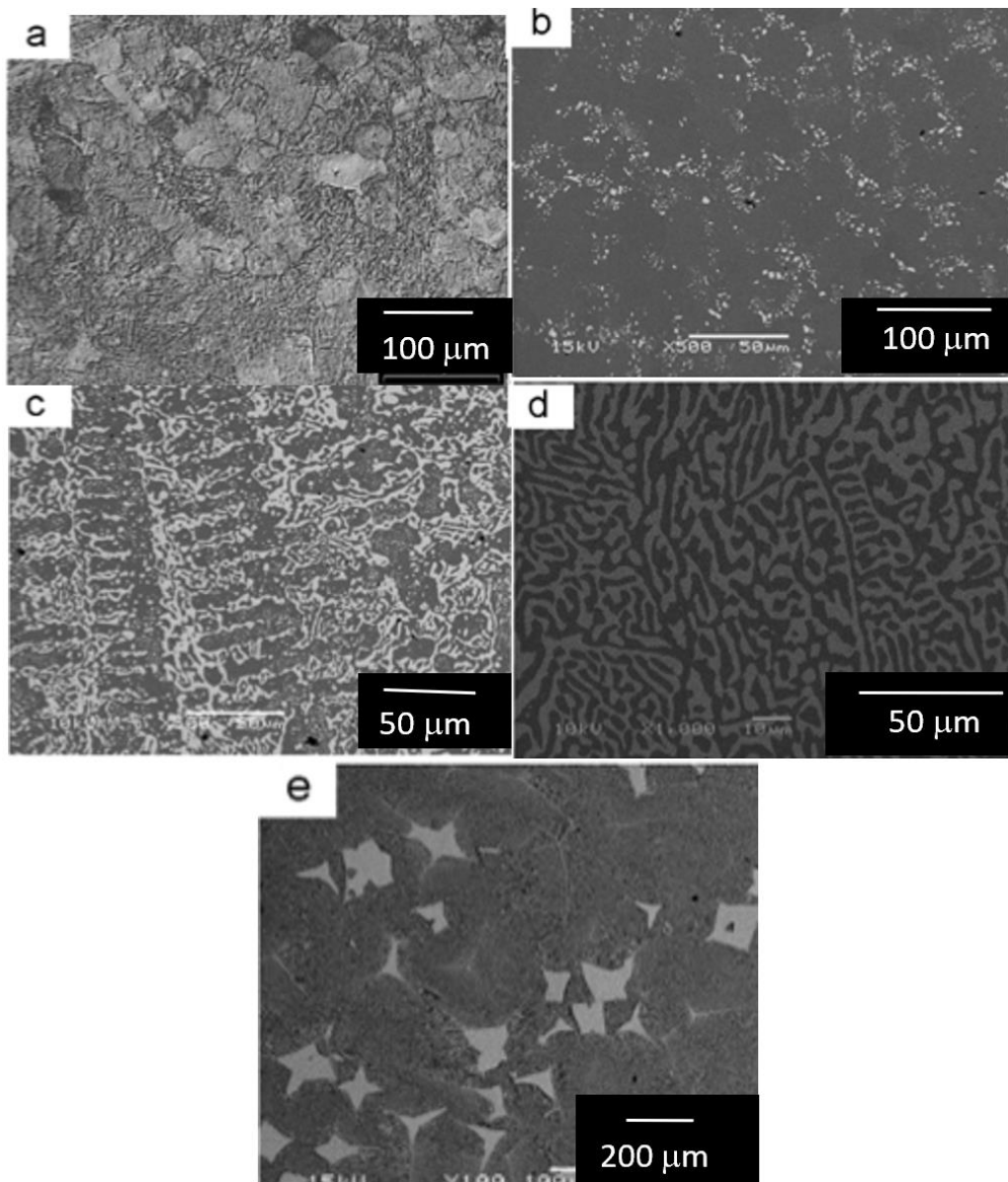


Figure 2.4: Microstructure of a) Sn-3 wt.% Bi b) Sn-10 wt.% Bi c) Sn-50 wt.% Bi d) Sn-57 wt.% Bi e) Sn-70 wt.% Bi [11]

Microstructure of Sn-Bi alloy at different composition was shown in figure 2.4. It is to be seen that at Sn-3 wt.% Bi, its microstructure is a solid solution with polycrystalline structure. As Bi content increased to 10 wt.%, there is a white precipitated phase in figure 2.4b which are Bi particles. When the percent of Bi increased to 50 wt.%, the microstructure showed eutectic phase with distributed fine Bi precipitates in figure 2.4c.

As it reached eutectic composition at figure 2.4d, it can be seen that only the lamellar structure can be found where they formed a continuous network. Lastly in figure 2.4e, Bi content reached 70 wt.%, which cause the distinct large Bi islands.

2.3 Atom Probe Tomography (APT)

The Atom Probe Tomography (APT) is considered as a recent and young technique. This microanalytical technique determined the spatial coordination and elemental identities of each individual detected atoms within a small volume at near atomic resolution. The individual detected atoms and ions were acquired and reconstructed as three-dimensional images of the materials. Each detected atoms and ions can be identified based on mass-to-charge ratio and time of flight. Concentration profile can be calculated in any direction. The reconstructed data is in the formed of interatomic distribution functions where it leads to studying atomic arrangement such as ordering, dopant interactions, cluster formation, crystal structure, diffusion, and early stages of precipitation. This technique allows the observation of compositional information along the structure at sub-nanometer levels.

Atoms and ions were detected from the process known as field evaporation where they were ionized by high electric field at the surface of material. The high electric field induces the ionization and desorption even at cryogenic temperature and high-power vacuum. The field is typically created by applying a voltage, approximately around 5-10 kV, to a specimen. The ionized positive ions are attracted and accelerated away from the sharp nanotip towards the detector and counter which also known as counter electrode. The electric field is related to the applied voltage and radius of curvature of the nanotip. A detector records the hit position of the ionized ions in x-y plane. These ionized ions together with the sequence of evaporation events were used to forms reconstructed data in three-dimensional space.

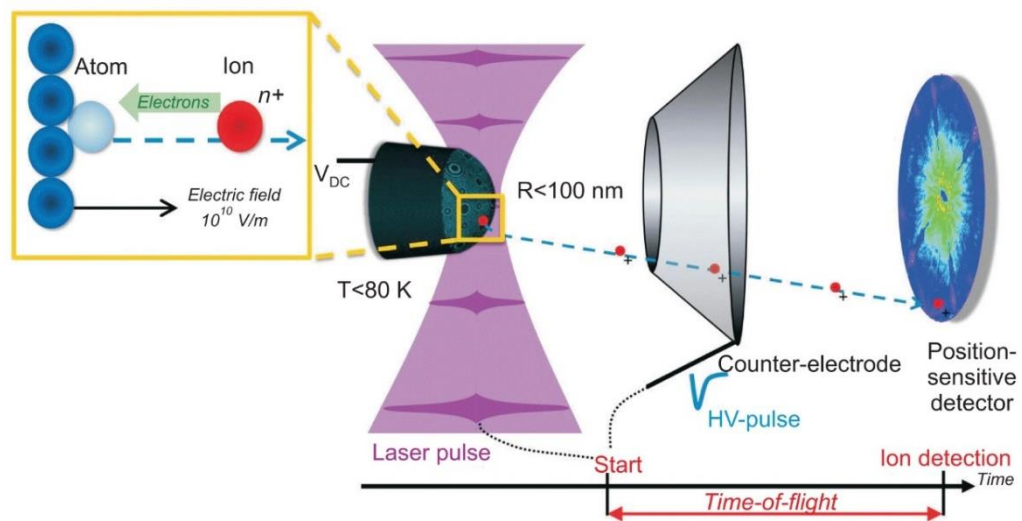


Figure 2.5: Schematic view of an Atomic probe tomography [12]

Time-of-flight (TOF) mass spectrometry was used to identify an atom by exploiting the time atom/ion take to travel the known distance from the specimen to the detector. Since accelerated ions under electric fields depends on the mass. Therefore Mass-charge ratio could be used to identify. An accurate departure time can be obtained by limiting a short time window for evaporation process. The specimen required a good electrical conductivity as it was use under electric field. In a semiconductor and insulators, thermal pulsing also known as laser pulsing has been used to energize the specimen.

In order to get a good reliable result from APT, the specimen preparation is a critical step. The criteria for good specimen for APT analysis is 1) the specimen must allow field evaporation and 2) the specimen must be very sharp. There are two main popular methods of specimen preparation: electropolishing and focused ion beam (FIB) milling.

2.3.1 Electropolishing

This method is considered relatively easy and fast. It does not require expensive and complicated instrumentation.

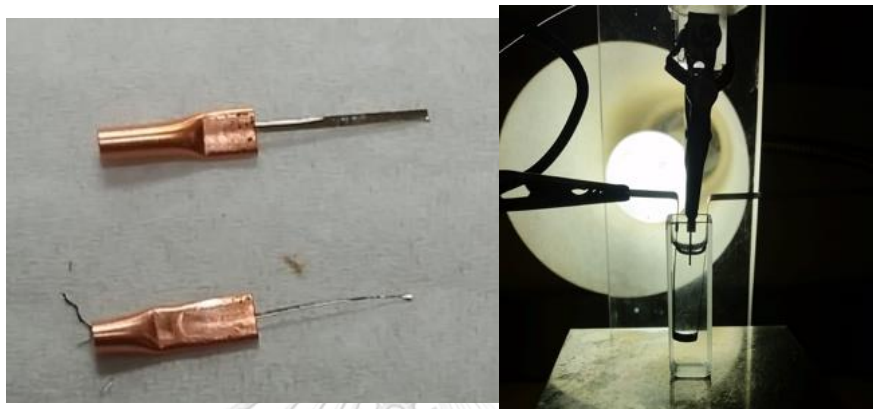


Figure 2.6: a) Wire of metal in Cu-clamp b) Electropolishing

The wire specimens can be prepared by cut from the bulk into appropriate sized pieces, usually around $0.5 \times 0.5 \text{ mm}^3$, by using a diamond or a rotating wire saw as shown in figure 2.6. It is important that the cross section is symmetric. Asymmetric specimen would lead to distort the ion trajectories toward the detector. The electropolishing gives two roughly needle-shaped specimens from removing the materials. The setting is shown in figure 2,6b. Blank is connected to positive DC voltage and a metal electrode is connected to the negative polarity and placed inside a container with a dense inert liquid and a layer of electrolyte. Electrolyte was another important criteria in given the optimized shape of nanotip. After the completion of this process, samples should be rinsed in distilled water and ethanol in order to remove any residual electrolyte and prevent deposition of any residue that might be dissolved in water remaining on the tip surface. The material can be mounted into a small copper tube prior to electropolishing as shown in figure 2.6a to enable easier handling and transfer for APT analysis.

2.3.2 Focus Ion Beam (FIB) method

This is a method that uses ions in preparation of specimens for APT. The process can be divided into two main parts namely, lift-out and sharpening. The lift-out was done by attaching a material, where the surrounding bulk area was dug out, to the end of a needle. The sharpening can be done by using annular milling methods which gradually improved the sharpness of the tip. This method is applicable to almost all materials. Care should be taken during the final steps of sharpening process in order to prevent ion-induced damage. This enables removal of a small region of material.

The detail steps of FIB lift-out procedure are as follows. First, the protective layer is applied over the region of interest. Platinum is usually used. Then material around three sides of the interest region is then removed by ion milling as shown in figure 2.7a. The wedge is removed by using an in-situ micromanipulator also known as omniprobe by attaching the wedge to the end of the probe then cutting the wedge free from the bulk material as shown in figure 2.7b. This probe is used to position the wedge above the carrier tip and mounted the section using platinum deposition.

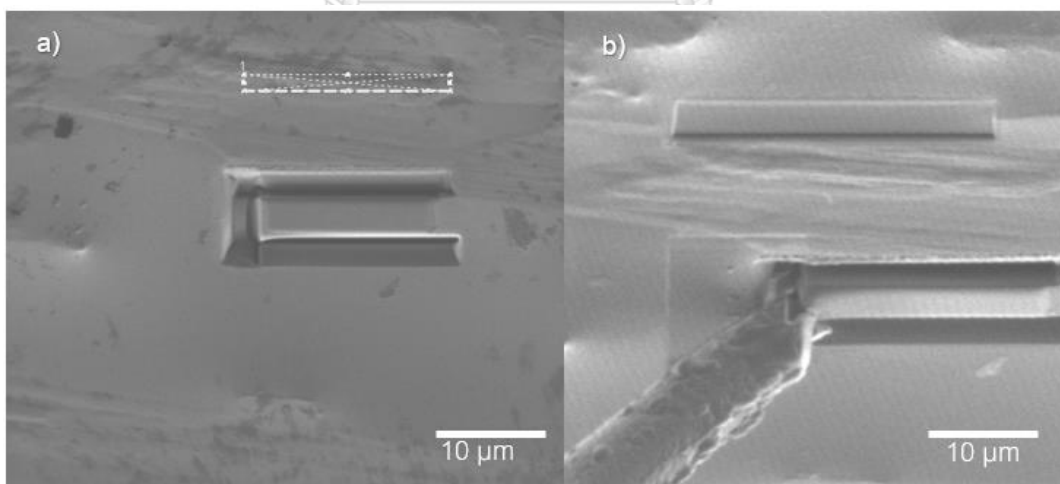


Figure 2.7: Lift out process a) removal of material around the interested area b) attachment of the Omniprobe

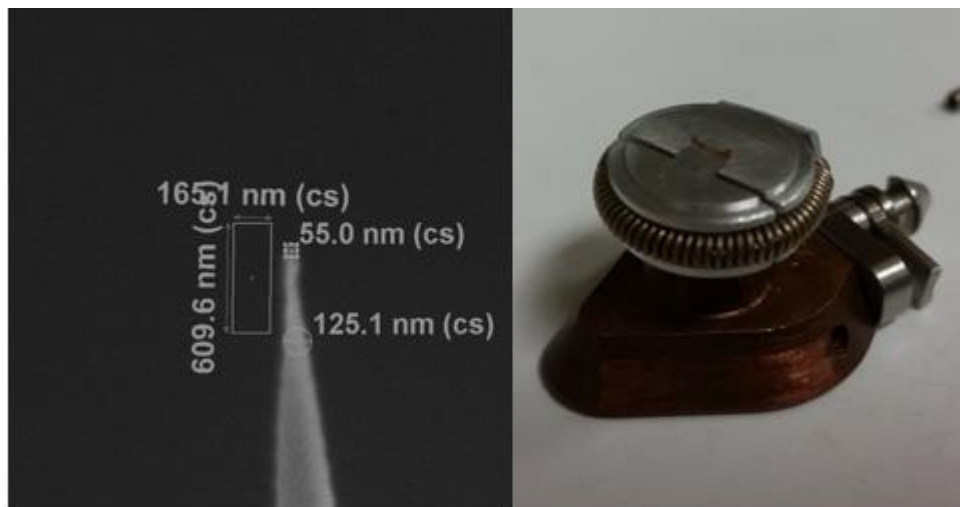


Figure 2.8: a) Atomic probe tip after shaping b) sample holder for Atomic probe

The series of annular milling steps are used in order to change the shape from wedge into a sharp needle with 100 nm curvature and followed by a low-energy FIB cleanup step. The outer diameter of the annular milling pattern during tip shaping is usually 4 μm with decreasing inner diameter at a beam current of 0.28 nA. The milling proceeds from the outer diameter of the pattern to the inner diameter of the pattern to carefully control any potential redeposition of removed material. Figure 2.8a shows tip after with diameter of 55 nm at the end. Figure 2.8b shows the tip holder that will be put into the Local Electrode Atomic Probe (LEAP) chamber.

2.4 Creep deformation

Creep behavior is defined as tendency of a solid material to move slowly or deform permanently under the influence of mechanical stresses. It is considered as a time-dependent deformation. This deformation is a result of long-term exposure to stress that is below their yield strength of the material. Often, $0.5T_m$ is considered as critical temperature for creep. In lapping process approach, the deformation may deform differently depending on the magnitude of the applied stress and its duration. Thus the

deformation may become so large that abrasive particles could no longer perform their function as they embedded onto lapping plate [13].

Stages of creep are shown in figure 2.9. In the initial stage, it is known as primary creep, the strain rate is relatively high, but slowly increasing with time. This is due to work hardening of the material. This initial strain is usually pure elastic. The secondary or steady state creep reaches when the strain rate is at its minimum and become constant as a result of balance between work hardening and recrystallization or annealing. As dislocation density is increased due to deformation hardening, dislocation annihilation causes the balance in deformation hardening and allow constant of dislocation density. Lastly, it is known as tertiary stage. The strain rate is exponentially increasing with stress. The load carrying area decreased as the specimen elongated and eventually rupture of the specimen.

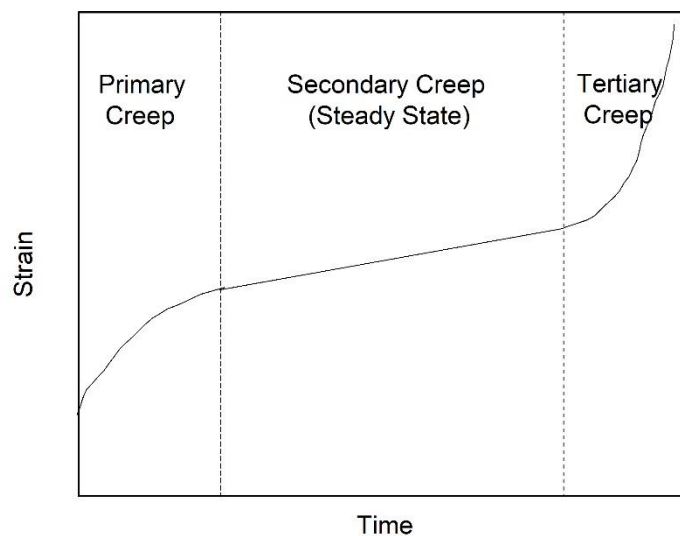


Figure 2.9: Stages of creep behavior

There are many mechanisms of creep, which are bulk diffusion (Nabarro-Herring creep), Climbing, Climb-assisted glide, grain boundary diffusion (Coble creep) and

thermally activated glide. The creep deformation mechanism is able to change due to the applied stress.

- Bulk lattice diffusion (Nabarro-Herring creep)

The motions of dislocations are controlled by atomic self-diffusion. This generates vacancies thus this mechanisms also known as vacancies assisted movement.

- Climb-assisted glide (Power-law creep)

Dislocations can climb and glide. The effect is more imminent at high temperature. Climbing can decrease accumulated stress from dislocation held up at obstacles. The speed of the mechanism can be determined by the climb step.

- Grain boundary diffusion (Coble creep)

This mechanism usually dominant at low temperature and fine-grained materials. The dislocation moves along its grain boundaries.

There are many research groups who reported that tin is strongly affected by creep behavior. Sn-Bi alloy system also exhibits creep behavior. Shen et al [11, 13, 14] investigated Sn-Bi alloy system and concluded that the main mechanism for creep in Sn-Bi alloy system is dislocation climb which is the rate-limiting mechanism in the nonlinear region. It is shown in figure 2.10 as a result from Shen et al [13] that the stress increases for all three composition of Sn-Bi when deformed at a higher strain rate.

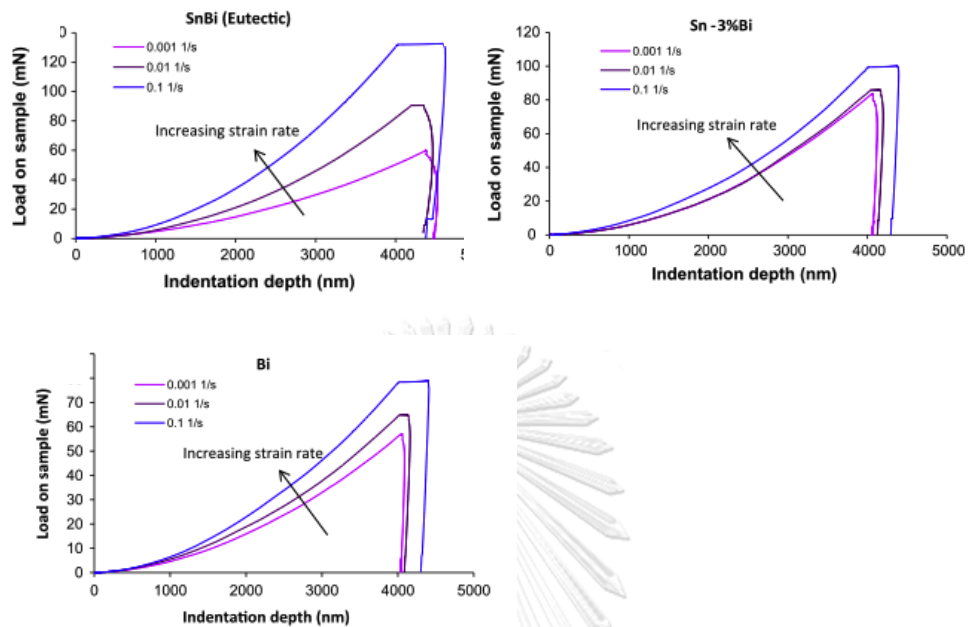


Figure 2.10: Load-displacement curves from nanoindentation of a) eutectic Sn-Bi b) Sn-3 wt.% Bi c) Pure Bi at three strain rates [13]

2.4.1 Thermal cycling creep

The strain measured by the extensometer is the total strain where it usually the sum of thermal, elastic and plastic strains.

$$\varepsilon_{total} = \varepsilon_{elastic} + \varepsilon_{thermal} + \varepsilon_{plastic}$$

The alloy can undergo internal stress when the alloy is subjected to thermal cycling under the presence of a small applied stress. The difference in coefficient of thermal expansion (CTE) behavior between the constituent phases could cause the internal stress. The deformation that combine both an external stress and repeated internal stress is called “thermal-cycling creep”. It is commonly observed in polycrystalline single-phase materials with anisotropic thermal expansion or thermal cycling of two-phase materials. The internal stress can be generated by thermal

expansion mismatch or thermal cycling of allotropic materials, where phase transformation produces internal mismatch stresses [16]. During thermal cycling, the larger strain than normal creep mechanism is expected due to the internal mismatch stresses

2.5 Nanoindentation

Instead of using large amount of sample and long-time creep experiment, one approach is to do strain rate sensitivity test. Nanoindentation method has gained popularity over the past decades. It is commonly used for the study of mechanical properties of materials. It is able to record small load and displacement with very high accuracy and precision. These data are used for obtaining physical parameter of materials like elastic modulus, hardness, residual stresses and viscous parameters such as creep. These parameters can be obtained by calculation from load and depth of penetration under the assumption that the material behaves in an elastic-plastic manner [17].

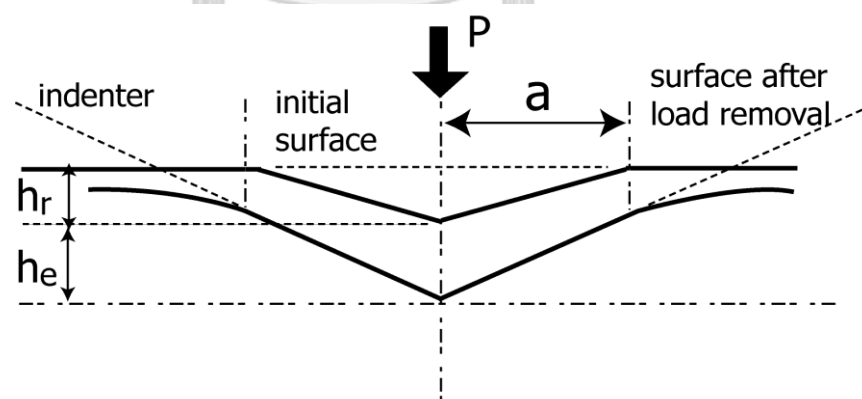


Figure 2.11: P is applied load, h is indenter displacement, h_r is plastic deformation after load removal and h_e is the surface displacement at the contact perimeter [18]

Principle of nanoindentation is based on the indenter tip of a known force that being use to apply on the specimen's surface, either bulk or thin film, and displacement

as well as dislocation while the penetration depth is measured. Loading and unloading profile is constructed from the continuously records of loads and displacement. The area of contact at full load is then determined by the depth of the impression and known angle of indenter as shown in figure 2.11.

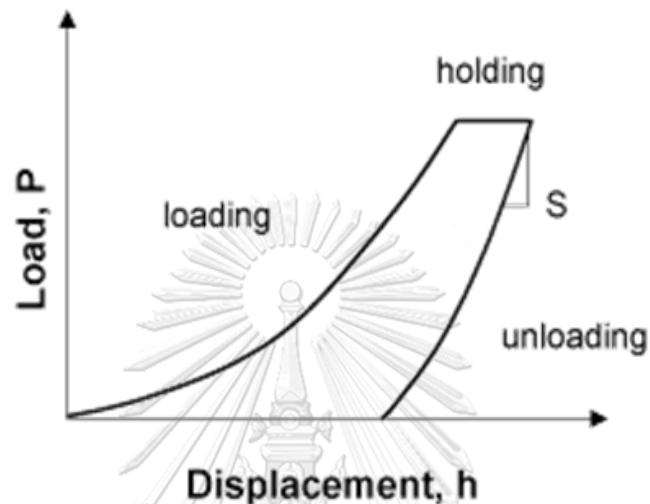


Figure 2.12: Schematic steps of typical indentation experiment [18]

From the records during the nanoindentation process, the load-displacement curve is established as shown in figure 2.12. During the loading steps, indenter tip creates elastic contact on sample's surface [19]. Later on, the transition from elastic to plastic contact was established as load was further applied into the sample's surface. The plastic region is growing as loading is increased. As shown in figure 2.12 that there is a holding period when maximum load is reached. Shape of the indenter tip usually overcome the mean contact pressure and cause the deformation that cause geometrical shape of the indenter tip to dominate on the surface of sample. However, this hold period is optional. It is usually hold for creep investigation.

Finally, when fully plastic region is established, further increased in load, would not increase in the mean contact pressure as shown in figure 2.13 [19-21]. In other word, the maximum load is reached when a fully developed a plastic region has been established. This could be used to define as hardness of material.

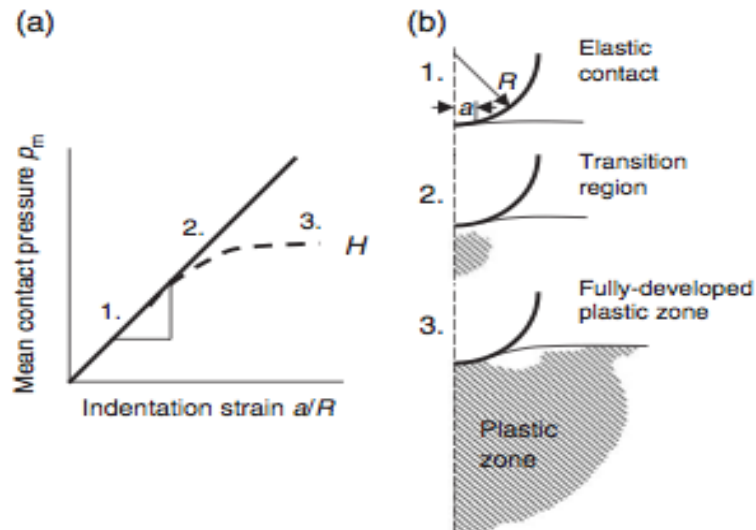


Figure 2.13: a) Relationship between indentation stress and indentation strain for spherical indenter. b) Schematic development of plastic region [19]

Lastly, after the load had reached its maximum, the applied load is reduced. During this step, elastic recovery usually occurs [22]. As it shows evidenced on the load-displacement curve where there is a reduction in displacement with decreasing load. This unloading data is ultimately used to determine the contact area. The slope of the unloading curve at any point is also used to calculate for stiffness and further used to calculate for elastic modulus of the system. Figure 2.14 shows the actual calculated and measured value from nanoindentation using Berkovich indenter on fused silica including each step of the indentation occur on the load-displacement curve.

Many analytical models have been developed by many research groups in order to calculate the hardness. The most widely accepted model is Oliver and Pharr method. The slope of the tangent at unloading data from maximum load with the derivation of the elastic equations of the contact is used to determine elastic modulus and hardness of the sample. The elastic modulus, hardness and stiffness can be found using equation 2.1, 2.2, 2.3 and 2.4 respectively [23-25].

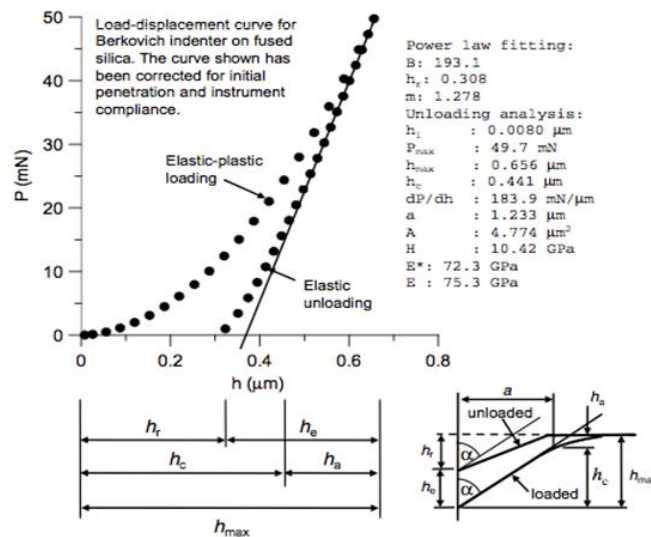


Figure 2.14: Load-displacement curve for Berkovich indenter on fused silica. Also included with the calculated and measured value from nanoindentation [20]

$$E = \frac{dP}{dh} \frac{1}{2} \frac{\sqrt{\pi}}{\sqrt{A}} \quad \text{Equation 2.1}$$

$$H = \frac{P}{A} \quad \text{Equation 2.2}$$

$$\frac{1}{S} = Cs = \frac{dh}{dP} = \frac{\sqrt{\pi}}{2} \cdot \frac{1}{\sqrt{A}} \cdot \frac{1}{Er} \quad \text{Equation 2.3}$$

$$\frac{1}{Er} = \frac{(1-\nu^2)}{E} + \frac{(1-\nu_1^2)}{E_1} \quad \text{Equation 2.4}$$

where E , P , h , A , H , Er and ν represent elastic modulus, load, displacement, projected area of contact, hardness, reduced modulus and Poisson's ratio respectively. The projected area of each different type of indenter tip is shown in figure 2.15.

New coming technique of nanoindentation is continuous stiffness measurement (CSM) that improves significantly on quality of data and ease of getting perfect values. Main principal of CSM is imposing a small sinusoidal signal on top of a conventional DC signal that cause the movement at indenter tip [25]. This technique gains advantage over conventional one as it provides a continuous results as a function of depth, the time required for calibration and testing steps since there's no need to multiple indentation or

unloading and the most important reason is that it prevent the thermal drift and time-dependent plasticity [24].

2.5.1 Shape of Nanoindentation's tip

Diamond is commonly used as an indenter tip. Different kinds of probes can be used for making an imprint onto material surface, see figure 2.15. Various shapes of probes have their own specific purposes [18].

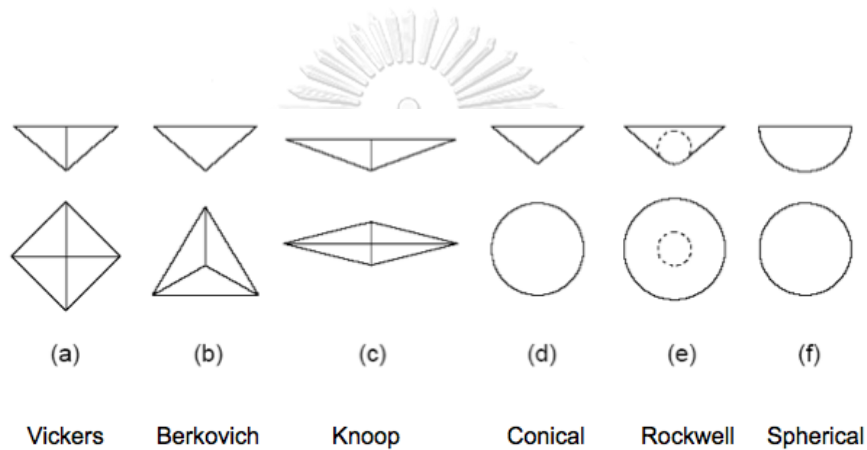


Figure 2.15: Schematics of indenter tips [18]

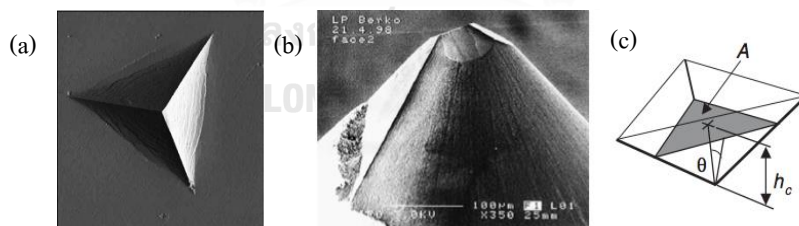


Figure 2.16: a) TEM of Berkovich indenter tip b) High-magnification SEM scan of Berkovich indenter tip c) Schematic of indenter geometry [18, 19]

1. Berkovich is one of the most commonly use indenter for measuring modulus and hardness values. As shown in figure 2.16, that it has three-sided pyramid

shaped with sharp and well-defined tip geometry with face angle of 65.3 degree and 50-150 nm tip radius in size [20]. Figure 2.16c shows that A is the projected contact area, which is the observed image at perpendicular to the surface of specimen without regard to the sloping side area, θ is the face angle and finally, h_c is the depth of the circle of the contact. This indenter tip leads to well-defined plastic deformation into the surface. However, it has poor elastic-plastic transition [18]. Blunt indenter has a spherical tip. It gains advantage in extended elastic-plastic deformation and yield point determination.

2. Vickers, four-sided pyramid with square base, is very useful in determining hardness for very shallow indentations.

3. Conical or cono-spherical, which has tip angle either at 60 or 90.
4. Cube corner is used to fracture toughness determination
5. Cylindrical punch.
6. Knoop, four-sided pyramid with rectangular base

2.5.2 Limitations and factors affecting nanoindentation

The load-displacement curve must be correctly investigated for contact depth determination, instrument compliance, and indenter tip shape in order to receive correct value of elastic modulus and hardness. Unfortunately, there are various sources of error in an achieved data. Therefore, some corrections are needed to get more precise data.

1. Thermal drift

Thermal drift is one of the most important factors especially when studying time dependent material or creep. It can be due to the different expansion in the machine or heat generation in the electronic devices. It usually causes the error in penetration depth data. It is hardly predicted since it could be either increasing or decreasing the penetration depth value. Thermal drift can generally minimized by using an insulation system or waiting to allow thermal equilibrium to reach before beginning the test [19]. However, the latter case is quite time-consuming method.

2. Initial penetration depth or layer thickness

Initial penetration defines as the initial contact between the indenter and the sample. This contact point is used as a reference point in displacement measurement. The basic concept of determining this reference point is that the indenter tip approaches the sample's surface and wait it is registered by software and the depth sensor is zeroed [20]. This is very crucial effect since this is the beginning of the test that could change the computed values of elastic modulus hardness. One of the most accurate methods of determining the initial penetration is to set an initial contact force and zeroed the depth sensor then start loading [19]. The initial set of data is achieved.

3. Piling-up and sinking-in

The elastic equation derives from many models mention above commonly assume that the contact circle is beneath the specimen surface which is call sinking-in. Unfortunately, sample may be pushed upwards, instead of sinking-in, and piling-up around the edges of the indentation. The main course of both piling-up and sinking-in is linked to the dislocation slip systems of the crystal [22]. As a result, the sample appears to be stiffer and harder, the penetration depth is less than it really is. Since the calculated contact area takes the depth penetration as an input, the calculated contact area is also less than expected and thus, hardness value and reduced elastic modulus are overestimated. The main reason that causes the false outcome is the piling-up material is supporting the indenter load, which make it harder for the indenter to penetrate [19]. Figure 2.17 illustrates the behaviors of piling-up and sinking-in. Currently, there is no method for correcting data for piling-up. The best solution is to avoid.

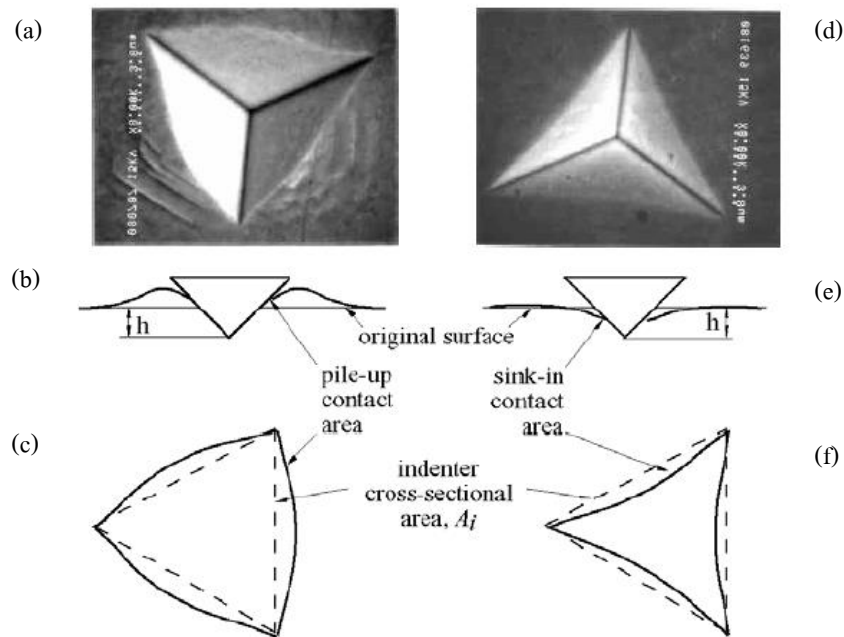


Figure 2.17: a) TEM of piling-up on Berkovich indenter tip b) sided view of piling-up c) Top view of piling-up d) TEM of sinking-in e) Sided view of sinking-in f) Top view of sinking-in [18]

4. Specimen preparation

During Nanoindentation, the theoretical equations assume a perfectly flat surface thus any abnormality on the surface profile will cause the misunderstood readings. Specimen preparation is a main influence on the quality of nanoindentation test data and its final value. Therefore, cleaning and polishing surface of the sample to reduce its surface roughness is significant.

2.6 Nanoindentation Creep

Nanoindentation has become popular technique for the investigation of the behavior of materials. Nanoindentation analysis method based on the assumption that the material behaves in an elastic-plastic manner. In general, creep deformation must be examined using specimens with shapes corresponding to the national standards

organizations such as JIS or ASTM. However, during the hold period of nanoindentation, the displacement is continuously increased, which is equivalent to creep. Therefore, the establishment of small specimens for creep study has emerged. However, not all materials exhibit an increase in displacement during the hold period. The displacement is dependent on the loading rate, hold period, and creep rate of the material.

By observing the increase in displacement with the hold value of applied load, this is called constant load indentation creep test (CL). This method can be used to study the time-dependent properties of crystalline materials and to find the value of the stress exponent [26].

The stress causes the material below the indenter to creep, and the indenter penetrates further into the material. It can be assumed that the creep has reached its steady state of creep rate in nanoindentation. Therefore, the power law creep equation can be used to determine the relationship between indentation strain rate and the hardness.

$$\dot{\epsilon} = A\sigma^n \exp\left(-\frac{Q}{RT}\right) \quad \text{Equation 2.5}$$

Where A is a constant, n is the stress exponent, Q is the activation energy for creep and R is the gas constant.

Based on the Oliver and Pharr method, hardness and elastic modulus values can be extracted from the experimental data (or load-displacement curves). Elastic modulus from indentation can be expressed based on Sneddon's elastic contact theory:

$$E_r = \frac{S\sqrt{\pi}}{2\beta\sqrt{A(h_c)}} \quad \text{equation 2.6}$$

Where S is the unloading stiffness (which can be found from the initial slope of the unloading load-displacement curve at the maximum displacement penetration), A is the projected contact area between the tip and the sample and β is the geometry of the indenter constant (β for Berkovich is 1.034). Hardness (H_c) is equivalent to the mean contact pressure where it is dependent upon the geometry of the indenter:

$$H_c = \frac{F}{A(h_c)} \quad \text{Equation 2.7}$$

$$A(h_c) = 24.5h_c^2 + a_1h_c + a_{\frac{1}{2}}h_c^{1/2} + \dots + a_{\frac{1}{16}}h_c^{1/16} \quad \text{Equation 2.8}$$

$$h_c = h_m - \varepsilon \frac{P_m}{S_m} \quad \text{Equation 2.9}$$

Where h_m is the total penetration displacement of the indenter at peak load, P_m is the peak load at the indenter displacement h_m , and ε is an indenter geometry constant (ε for Berkovich is 0.75). First term of projected contact area equation is the area function of the indenter, while the second term and latter terms are experimentally determined for correcting the projected contact area function. In this study, indenter tip is assumed to be in perfect shaped.

In the constant load method [27], the displacement is collected as a function of time during the load hold. The calculated hardness would decrease as the indenter further penetrate into the specimen since the contact area will increase during the hold period. To calculate the displacement rate (Strain rate), \dot{h} , the indenter displacement versus time curve at constant indentation load was fitted with the following empirical equation:

$$h(t) = h_i + \beta(t - t_i)^m + kt \quad \text{Equation 2.10}$$

The stress defined as the pressure underneath the indenter

$$\sigma = \frac{\text{Load}}{\text{Projected area}} = \frac{L}{Kh^2} \quad \text{Equation 2.11}$$

where K is a constant parameter depending on the shape of the indenter and h is the depth of the indenter in the material.

Indentation strain rate defined as penetration rate of the indenter divided by its current depth

$$\dot{\epsilon} = \frac{1}{h} \frac{dh}{dt}$$

Equation 2.12

The calculated stress-strain rate data is similar to conventional creep test, therefore it is possible to determine the stress exponent in the same manner. The methodology of nanoindentation creep analysis can be found elsewhere [26-28].

Regarding thermal drift during creep measurement during holding period, the correction of displacement data is needed as it could lead to a larger displacement. The thermal drift rate was measured for all experiments and each displacement data were corrected according to each thermal drift rate. It was measured at the 10% of the maximum hold load.



Chapter 3

Atomic arrangement evolution of binary Cu-Zr based metallic glass

3.1 Study of atomic diffusion

The atomic arrangements in binary Cu-Zr based MG were intensively studied using simulation methods and experimental methods such as high-energy X-ray diffraction, and neutron diffraction. The information on interatomic distances and coordination numbers were determined from the experiments. However, there are some drawback on this information, not only that they merely provide the information just for the first pair coordination, the complication of getting this information are proportionally increasing with the number of elements.

The aim of this chapter is to study the structural behavior of binary Cu-Zr metallic glasses during devitrification. The analysis of structural behavior should give evidence whether or not phase separation in CuZr glass exists as well as nanocrystal during crystallization of metallic glass.

3.1.1 Methodology

The Cu-Zr binary alloy ingot of nominal compositions $\text{Cu}_{64}\text{Zr}_{36}$, $\text{Cu}_{56}\text{Zr}_{44}$, and $\text{Cu}_{50}\text{Zr}_{50}$ were prepared by a melt-spinning technique with Cu roll at Eco-FM Company (Incheon, Korea). 75 mm wide with 75 μm thickness amorphous ribbons were produced. The amorphous structure was verified using XRD with Synchrotron X-rays source at Pohang Light Source, Korea. To analyze the structural transition behavior in detail, samples were heat treated in the DSC (NETZSCH5 STA 449F3) at a rate of 20 K/min to different transition temperatures such as temperature between glass transition temperature, T_g , and crystallization temperature, T_c , depending on the compositions as shown in table 3.1, followed by cooling down to room temperature at a rate of 20 K/min.

To observe phase evolutions during devitrification process, heat was discontinued at 50% between T_g and onset temperature, T_x , 10% between T_x and T_c along with temperature beyond T_c . They will be referred to as T_1 and T_2 , respectively onward. The partially crystallized specimens were heated in DSC chamber and interrupted at a specific temperature as shown in table 3.1. The fully crystalline structure of all compositions was heat-treated up to 823 K to ensure that all the amorphous and meta-stable phase were in the equilibrium state and fully crystallized.

Chemical compositions were detected using laser-assisted local electrode atom probe (Cameca LEAP 4000X Si). The LEAP specimens were prepared by standard focused ion beam-based (FIB) lift out and annular milling protocols with a radius of curvature at the tip of 100 nm using a FEI Helios Nanolab 600 dual-beam SEM/FIB. The final FIB clean-up procedure was carried out at 5, 3.5 and 1 kV to ensure the minimum Ga impurities. The operation parameters of the LEAP were set at temperature of 54 K, pulse rate of 250 kHz, pulse energy of 10 pJ and detection rate from 0.5-2%. The data were collected up to 20 million ions. The detail of the set-up was described elsewhere [29]. The corresponding mass spectra was normalized to the counts of the $^{63}\text{Cu}^+$ peak. Basic tomographic reconstruction was performed using the Integrated Visualization & Analysis Software (IVAS 3.6.8, by Cameca, USA, formatting). SEM images were utilized to access the details of sample apex geometry for data reconstruction. High resolution transmission electron microscope (HRTEM) observation were performed using a TALOS F200X, FEI. TEM specimens were prepared by Precision Ion Polishing System (PIPS, GATAN Model 691) with argon ion beam energy of 3 keV and the incident angle of 5° on liquid nitrogen stage to prevent unwanted artifacts. Crystallographic information was obtained Fast Fourier Transformation (FFT) image processing of High Resolution TEM (HRTEM) images.

	Glass transition temperature, T_g (K)	Onset temperature, T_x (K)	Crystallization temperature, T_c (K)	50% between T_g and T_x (T_1)	10% between T_x and T_c (T_2)
$\text{Cu}_{64}\text{Zr}_{36}$	748.15	788.3	790.45	768.15	788.5
$\text{Cu}_{56}\text{Zr}_{44}$	701.65	757.6	760.05	729.63	757.8
$\text{Cu}_{50}\text{Zr}_{50}$	683.85	735.95	739.65	709.9	736.32

Table 3.1: Specific transition temperature of $\text{Cu}_{64}\text{Zr}_{36}$, $\text{Cu}_{56}\text{Zr}_{44}$ and $\text{Cu}_{50}\text{Zr}_{50}$

3.1.2 Result and discussion

The amorphous state of the as-received $\text{Cu}_{64}\text{Zr}_{36}$, $\text{Cu}_{56}\text{Zr}_{44}$, and $\text{Cu}_{50}\text{Zr}_{50}$ ribbons were confirmed by the presence of the only broad diffraction maxima in the XRD pattern at 40 degrees as shown in figure 3.1. All as-received specimens were x-ray amorphous with first maxima marginally shifting to lower angles as Zr concentration increased. This suggests that the specimen with lower concentration of Zr has smaller atomic distance. This could imply that the atomic arrangement is loosely pack in a specimen with lower Zr concentration.

The thermal behavior of the amorphous Cu-Zr binary alloys is shown in figure 3.2. The glass transition and the crystallization temperatures are observed by the respective endothermic and exothermic heat flow events. The insets showed the temperatures at the onset of the endothermic reactions resulting from the glass transition. Glass transition temperature T_g , onset temperature of the crystallization event T_x , crystallization temperature T_c , are shown in table 3.1. These obtained values are in good agreement with other splat quenched and melt-spun ribbons [30]. The presence of ZrO and Sn could cause an increase in T_g and T_x since it alters the local chemical order. This would lead to an inhibition of atomic diffusion therefore the T_g and T_x increases [31].

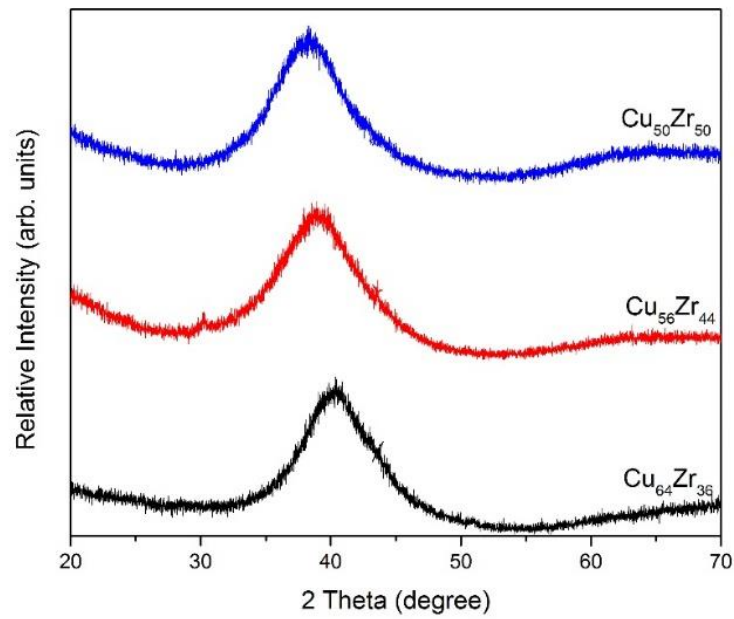


Figure 3.1: X-ray diffraction traces of the as-receive Cu-Zr binary metallic glass ribbons

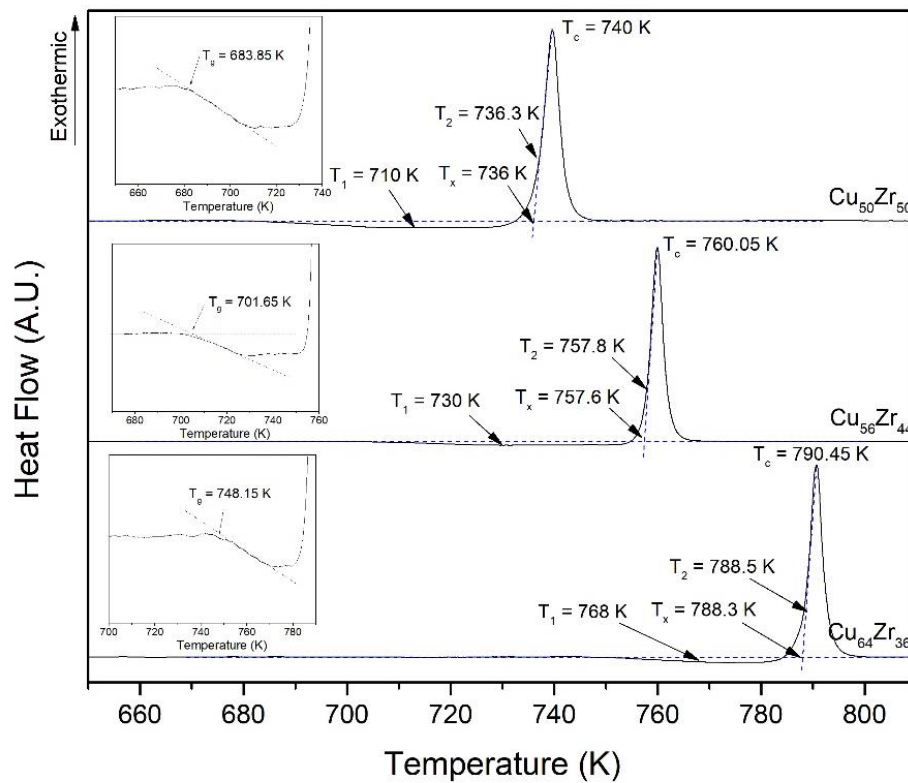


Figure 3.2: Thermal behavior of amorphous Cu-Zr binary alloys

The full constructed volume with compositions of $\text{Cu}_{64}\text{Zr}_{36}$, $\text{Cu}_{56}\text{Zr}_{44}$, and $\text{Cu}_{50}\text{Zr}_{50}$ at studied transition temperatures were analyzed by LEAP and displayed in figure 3.3. The specific nominal composition of Cu-Zr binary alloy is mainly reproduced well by the LEAP measurement at most transition temperature stages and shown in table 3.2. However, there are some unexpected off-composition such as heat treatment of $\text{Cu}_{56}\text{Zr}_{44}$ at T_2 and heat treatment of $\text{Cu}_{50}\text{Zr}_{50}$ at 823 K. As the area that was being investigated with APT was genuinely small together with the heat treatment condition, it could imply that there's a phase separation which caused the inhomogeneous of composition. This issue will be further elaborated in TEM section. There is a present of Sn in all compositions. However, the composition of Sn has increased from 0.3 at.% at $\text{Cu}_{64}\text{Zr}_{36}$ to 0.8 at.% at $\text{Cu}_{50}\text{Zr}_{50}$, where it does not depend on the temperature. In addition, the Sn impurity could be traced back to the Cu roll during sample fabrication as it is common for Sn to dissolve in Cu-roll. Hydrogen was found at the average of 3 at.%. To be noted, hydrogen that were considered here is only associated with Zr in the form of ZrH, free hydrogen that were diffused through surface of the tip from the freely-Hydrogen inside the APT chamber and environment while transferring the tips from SEM-FIB chamber, were excluded here. The study of hydride will be discussed later.

T (K)	$\text{Cu}_{64}\text{Zr}_{36}$			$\text{Cu}_{56}\text{Zr}_{44}$			$\text{Cu}_{50}\text{Zr}_{50}$		
	T_1	T_2	823 K	T_1	T_2	823 K	T_1	T_2	823 K
Cu	60.24	65.42	61.23	52.68	41.52	52.99	44.58	50.36	38.03
Zr	38.55	32.55	35.54	39.69	53.39	44.91	45.62	46.99	54.84
Sn	0.43	0.31	0.32	0.41	0.58	0.40	0.83	0.59	1.03
H	0.45	1.36	2.44	6.84	3.94	1.25	8.12	1.47	4.06
O	0.33	0.36	0.47	0.38	0.57	0.45	0.85	0.59	2.04
Cu ratio	60.98	66.78	63.27	57.03	43.75	54.13	49.43	51.73	40.95
Zr ratio	39.02	33.22	36.73	42.97	56.25	45.87	50.57	48.27	59.05

Table 3.2: Chemical composition of $\text{Cu}_{64}\text{Zr}_{36}$, $\text{Cu}_{56}\text{Zr}_{44}$, and $\text{Cu}_{50}\text{Zr}_{50}$ at different heat treatment temperature

Figure 3.3 shows full reconstructed volume analyzed by APT with average of 20 million ions per tip. Atomic maps of $\text{Cu}_{64}\text{Zr}_{36}$ were shown in figure 3.3a, where the superimposed of all the elements are shown on the left. The as-receive specimen is fully amorphous as confirmed by XRD in figure 3.1. As the specimen were heat-treated up to T_1 , it still showed atomic-scale homogeneity. There is no fluctuation of the concentration and long-range order detected. This clearly indicates that there is no chemical decomposition or cluster in this stage. The evidence of clustering in $\text{Cu}_{64}\text{Zr}_{36}$ was appeared above the crystallization onset temperature, T_x . The specimen distinctly showed atomic-scale heterogeneity after temperature increased to crystallization temperature as illustrated in the reconstructed atom maps. Oxygen is appeared in the form of ZrO, afterwards ZrO clusters grew larger as temperature increased. Due to the high reactivity of Zr for O, the ZrO is prematurely formed. Similarly, specimens were hydrogenated and formed ZrH as shown in figure 3.3a. However, ZrH does not show any sign of growing with increasing temperature. Moreover, Sn also show parallel trend with ZrO. This verified that the T_1 annealing specimen is an amorphous alloy while the T_2 and 823 K annealing specimen shows cluster ions which signify phase separation events. Similar trend was also found in $\text{Cu}_{56}\text{Zr}_{44}$ and $\text{Cu}_{50}\text{Zr}_{50}$, though $\text{Cu}_{50}\text{Zr}_{50}$ is more prominent in term of phase separation and oxide growth. Keep in mind that the difference temperature between T_c and 823 K of $\text{Cu}_{50}\text{Zr}_{50}$ is larger than in $\text{Cu}_{56}\text{Zr}_{44}$, which could imply that it has longer time for atomic diffusion. Thus, ZrO and ZrHg grows larger in $\text{Cu}_{50}\text{Zr}_{50}$.

Oxygen could be introduced during FIB process where it could associate with Zr to form ZrO or it could also stay in the form of oxygen ion. Amount of ZrO and O are consistent as temperature increased for all three compositions as shown in figure 3.4. Atomic concentration of hydrogen is unusually high as shown in table 3.2. Freely hydrogen in the chamber could diffuse into the specimen tip in the form of H^+ during each laser pulse where it will be discussed later in section 3.3. However, only $\text{Cu}_{64}\text{Zr}_{36}$ shows inverse concentration between ZrH and H, which could imply that the free hydrogen in the tip associate with Zr as temperature increase.

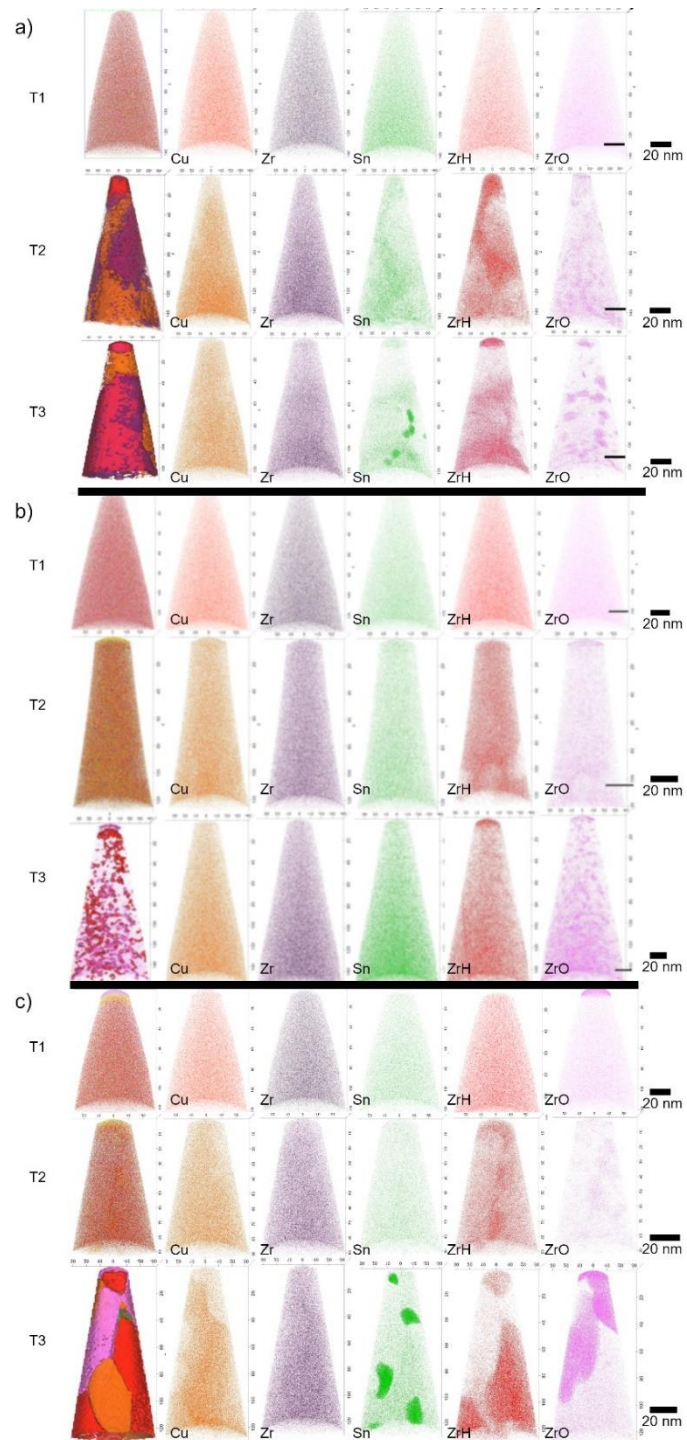


Figure 3.3: Reconstructed volume at different temperatures with compositions of a) $\text{Cu}_{64}\text{Zr}_{36}$, b) $\text{Cu}_{56}\text{Zr}_{44}$, and c) $\text{Cu}_{50}\text{Zr}_{50}$. The left column shows the superimposed of all major elements

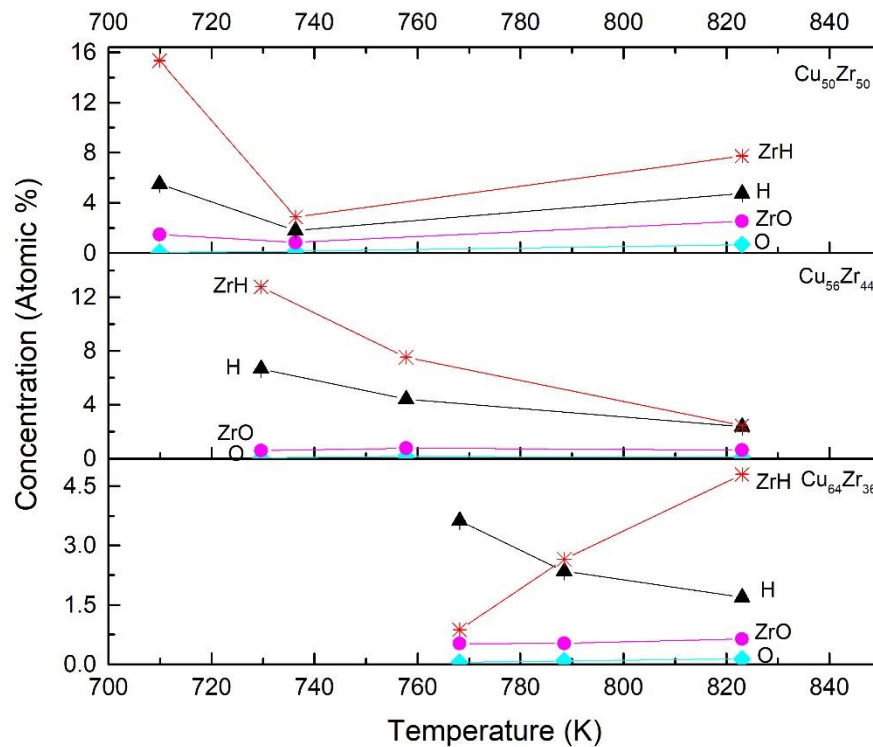
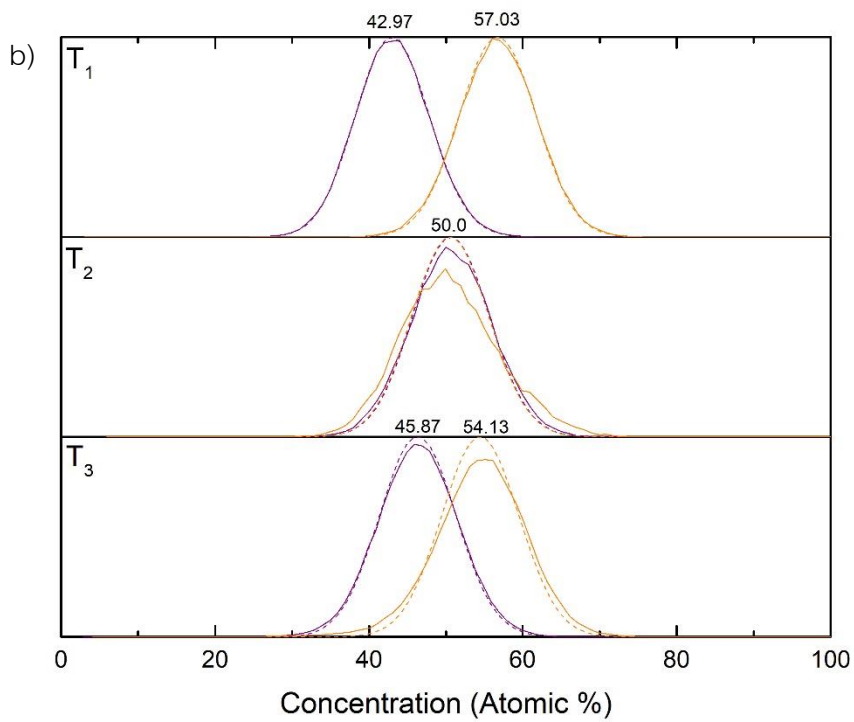
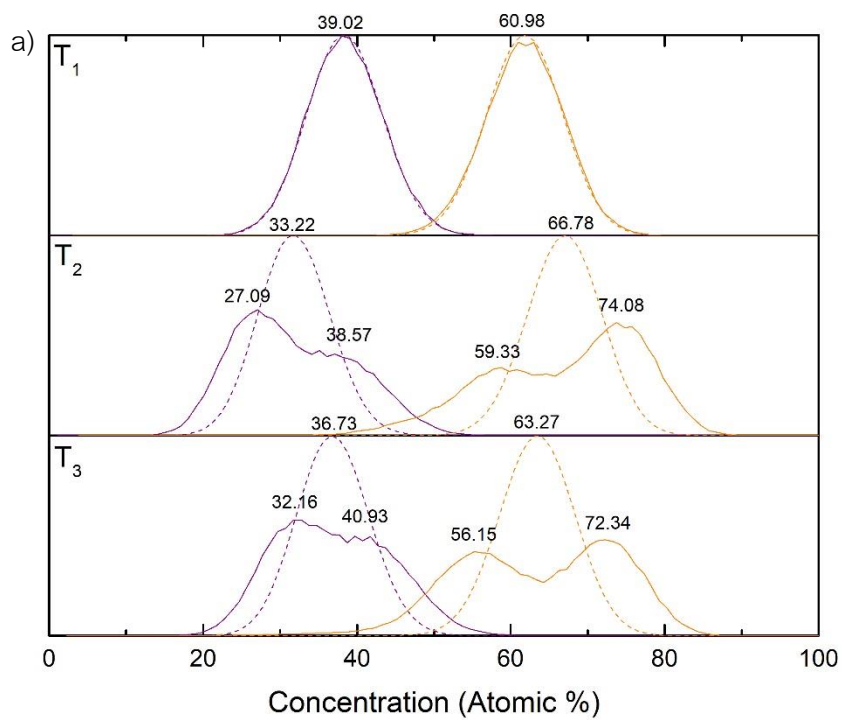


Figure 3.4: Atomic concentration of ZrH, H, ZrO and O in a) $\text{Cu}_{50}\text{Zr}_{50}$ b) $\text{Cu}_{56}\text{Zr}_{44}$ c) $\text{Cu}_{64}\text{Zr}_{36}$ at different annealing temperatures

Reconstructed volume of the as-receive specimen in figure 3.3 shows uniform distribution of composition elements of all studied specimens which indicating no phase separation.

The frequency distributions are commonly used to quantify compositions. The reconstructed data was divided into equal blocks of 100 ions then accumulated to form a frequency distribution as shown in figure 3.5. The frequency distributions were partitioned into Cu and Zr peak around their specific nominal concentration follow the probability distribution where the maximum corresponding to their average chemical compositions. The binomial distribution is plotted as a solid line in direct comparison to the frequency distribution of the as-receive specimen in order to evaluate how the solutes are distributed compared to the homogeneous distribution of atom. The Cu and Zr are shown in orange and purple, respectively. There is no obvious difference

between the composition distributions around the Cu and Zr atoms at the temperature close to T_1 for all three compositions, this indicated that there is no chemical order clusters. As the annealing temperature increases to T_2 in $\text{Cu}_{50}\text{Zr}_{50}$, both Cu and Zr peaks show minor deviations from the binomial distributions where they started to develop a longer tail in the distribution which could indicate the segregation effect or depleted matrix. Moreover, a right skew has been observed in the Cu peak which could indicate that Cu has segregated at around 30 at.%. $\text{Cu}_{56}\text{Zr}_{44}$ also shows minor deviations from the binomial distributions and a longer tail in the Cu peak. However, the Cu and Zr peaks do not gather around their specific nominal concentration. For $\text{Cu}_{64}\text{Zr}_{36}$ annealed at T_2 , the Zr peak of frequency distribution has divided into 2 consecutive peaks around 27 and 39 at.%, while the Cu peak has also divided into 2 consecutive peaks around 60 and 74 at.%. This could imply that Cu and Zr segregated and formed Cu_8Zr_3 and $\text{Cu}_{10}\text{Zr}_7$ where the amount of Cu_8Zr_3 is greater. As the temperature increases above T_c , the phase segregation becomes more prominent for all compositions except for $\text{Cu}_{56}\text{Zr}_{44}$ where only a minor deviation from the binomial distribution was observed. Since, $\text{Cu}_{56}\text{Zr}_{44}$ grain might be larger than an APT tip, where it could be assumed that only one intermetallic phase was being investigated. This will be clarified later in the TEM section. Figure 3.5b and 3.5c have shown that as the annealing temperature is above T_c , $\text{Cu}_{64}\text{Zr}_{36}$ and $\text{Cu}_{50}\text{Zr}_{50}$ have fully recrystallized and formed intermetallic phases. Specifically, the Cu peak of $\text{Cu}_{50}\text{Zr}_{50}$ has divided into 36 and 49 at.% where the Zr peak showed a smaller peak from the distribution with a longer tail. This could imply that Cu and Zr are in the form of $\text{Cu}_{10}\text{Zr}_7$. Similarly, the Cu peak of $\text{Cu}_{64}\text{Zr}_{36}$ has divided into two peaks at 56 and 72 at.% while the Zr peak has divided into two peaks at 32 and 40 at.%. This could imply that Cu and Zr are in the form of $\text{Cu}_{10}\text{Zr}_7$.



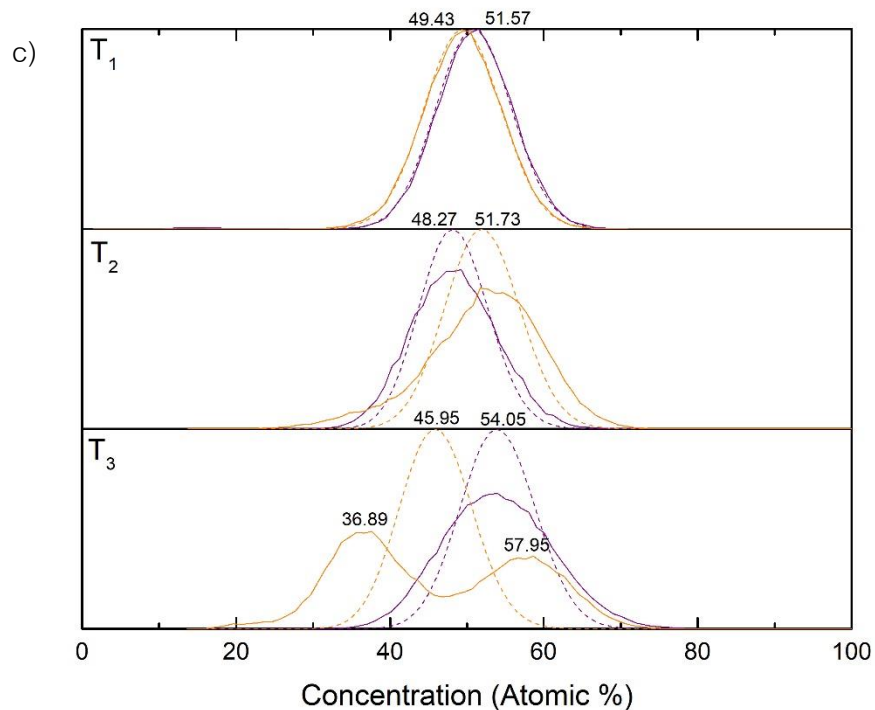


Figure 3.5: Frequency distribution functions of a) $\text{Cu}_{64}\text{Zr}_{36}$, b) $\text{Cu}_{56}\text{Zr}_{44}$, and c) $\text{Cu}_{50}\text{Zr}_{50}$ metallic glass ribbon at different heat treatment temperature

Apart from the calculations, phase separations and clusters were directly observed under TEM and reconstructed volumes. However, only the fully crystallized specimens (annealed at 823 K) were observed under TEM due to the difficulty of TEM preparation where it's a challenging to disrupt and prevent a further process of crystallization at specific step [32]. Figure 3.6 shows reconstructed volume of $\text{Cu}_{64}\text{Zr}_{36}$ annealed at T_2 . The concentration of Cu in Cu-concentrated area is approximately 70 at.% while Zr is depleted to 30 at.%. The concentration of Cu in Zr-concentrated area is approximately 50 at.% while Zr is depleted to 40 at.%. From these proxigrams, it could be concluded that the Cu-concentrated area is Cu_3Zr_3 and the Zr-concentrated area is $\text{Cu}_{10}\text{Zr}_7$. It is clearly shown that a certain amount of H has dissolved into the Zr-concentrated area with an approximate content of 6 at.% and into Cu-concentrated area with an amount of 3 at.%. The concentration of Sn and O were slightly increased around

boundaries of Zr-concentrated area and ZrH while they were depleted around Cu-concentrated area. In some cases, phases found to crystallize from amorphous matrix are not stable at their crystallization temperature and therefore decompose into the corresponding equilibrium. This finding is in good agreement with other cooling rate in term of $\text{Cu}_{10}\text{Zr}_7$. For the reason that the most stable phase according to phase diagram is $\text{Cu}_{10}\text{Zr}_7$ phase since it is more thermodynamically favored. Kneller et al [33] found that $\text{Cu}_{62}\text{Zr}_{38}$, which is comparable to $\text{Cu}_{64}\text{Zr}_{36}$, primarily crystallizes at T_x as $\text{Cu}_{24}\text{Zr}_{13}$. However, it is unstable at this temperature and decomposes into $\text{Cu}_{51}\text{Zr}_{14}$ and $\text{Cu}_{10}\text{Zr}_7$, which are the equilibrium phase at that temperature. M Apreutesei et al [34] has found that $\text{Cu}_{51}\text{Zr}_{14}$ and $\text{Cu}_{10}\text{Zr}_7$ slowly crystallized in a small amount at 10 K below T_g .

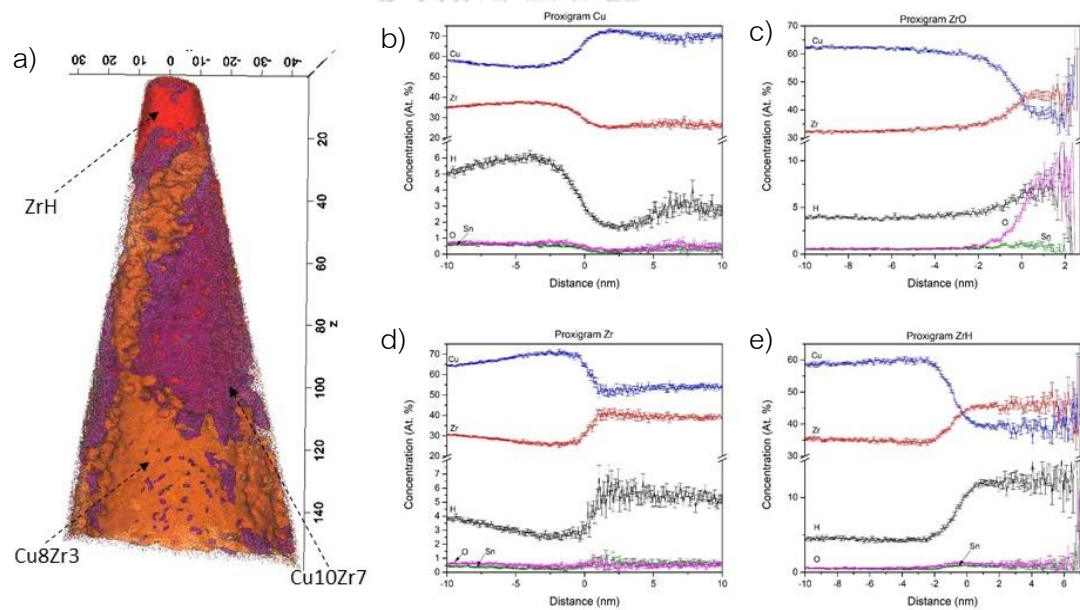


Figure 3.6: a) Reconstructed volume of $\text{Cu}_{64}\text{Zr}_{36}$ annealed at T_2 b) Proximity histogram concentration profiles from selected volume of Cu cluster c) Proximity histogram concentration profiles from selected volume of ZrO cluster d) Proximity histogram concentration profiles from selected volume of Zr cluster e) Proximity histogram concentration profiles from selected volume of ZrH cluster

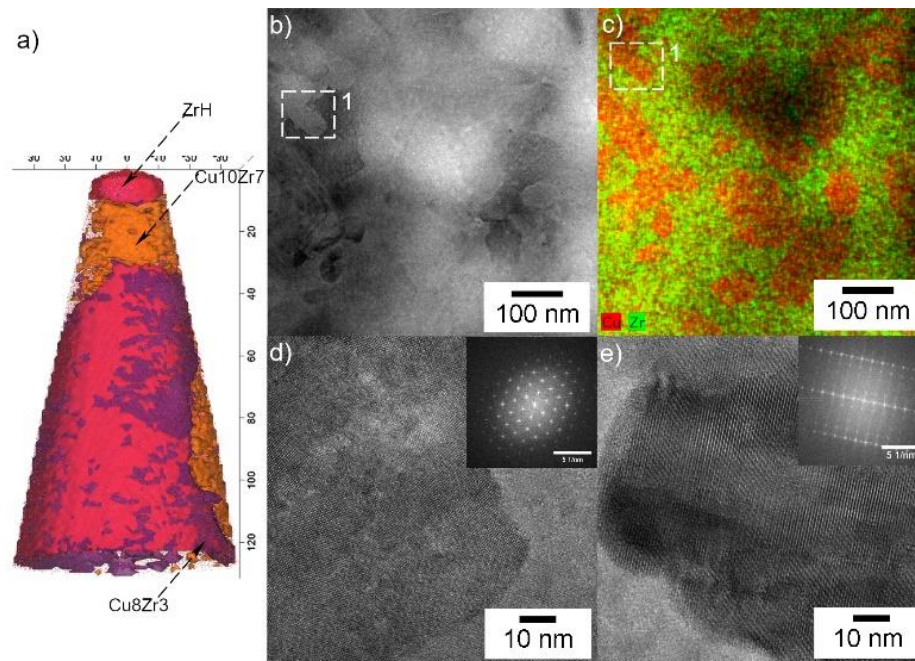


Figure 3.7: a) reconstructed APT of $\text{Cu}_{64}\text{Zr}_{36}$ b) TEM bright field of $\text{Cu}_{64}\text{Zr}_{36}$ c) EDS pattern of $\text{Cu}_{64}\text{Zr}_{36}$ d) HRTEM of $\text{Cu}_{64}\text{Zr}_{36}$ of the area enclosed in a box in b) and an inset is an FFT pattern of the Cu-rich region e) HRTEM of $\text{Cu}_{64}\text{Zr}_{36}$ of the Zr-rich region and an inset is an FFT pattern of the corresponding area

From the 823 K annealing specimen, there are two distinct phases which are Zr-concentrated and Cu-concentrated as shown in figure 3.7a. From TEM diffraction pattern and proxigrams in figure 3.8, it can be concluded that the Zr-concentrated area is $\text{Cu}_{10}\text{Zr}_7$, while the Cu-concentrated area are combined between two difference phase which are $\text{Cu}_{51}\text{Zr}_{14}$ and Cu_8Zr_3 . From TEM observation, Cu-rich area are in a net-shape like superimposed on the Zr-rich area in the background. The final stable crystallization phases above T_x were $\text{Cu}_{51}\text{Zr}_{14}$ and $\text{Cu}_{10}\text{Zr}_7$ compounds similar to other research group [34]. On the other hand, Cu_2Zr , Cu_8Zr_3 and $\text{Cu}_{10}\text{Zr}_7$ were presented with the cooling rate of 40 K/min [30].

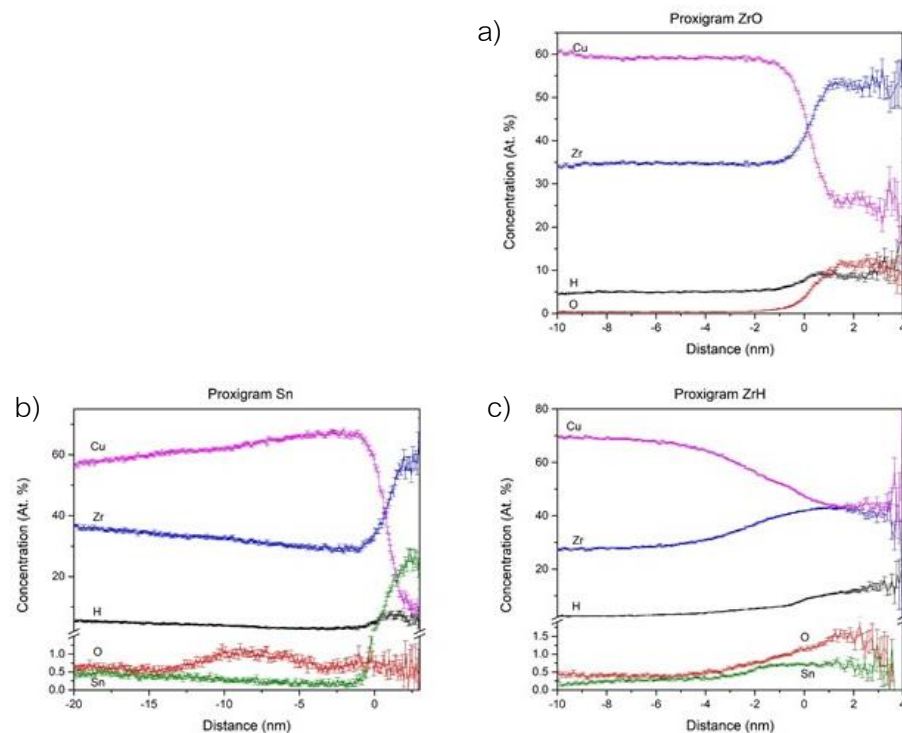


Figure 3.8: Proximity histogram of reconstructed volume of $\text{Cu}_{64}\text{Zr}_{36}$ annealed at 823 K
 a) Proximity histogram concentration profiles from selected volume of ZrO cluster
 b) Proximity histogram concentration profiles from selected volume of Sn cluster
 c) Proximity histogram concentration profiles from selected volume of ZrH cluster

Considering that Zr has a strong affinity with oxygen where it is known as an excellent oxygen getter material, certain number of oxygen is expected in Zr-based amorphous alloys. These oxygens maybe dissolved into the melt from the atmosphere. As can be seen from the reconstructed tips in figure 3.3 that Zr oxide has agglomerated after the specimen was heat treated above T_1 , then growing in size after continuing the heat treated. These oxides formed on the surface are due to the poor vacuum in the DSC chamber during annealing, leading to a loss of Zr atoms available in the structure. Zr is easily oxidized due to the well-known affinity of Zr for Oxygen. Oxide of Zr can be occurred in two formed which are monoclinic phase and tetragonal phase. Internal oxidation of ZrO in all three compositions presented in the form of nanosized grains where it can be concluded that they are presented in the tetragonal phase [34]. Those

small oxide clustered could acts as a nucleating site with a crystallite growing around it. As mentioned earlier that primary crystallized phase could be a meta-stable phase since the coordination of oxygen atoms could leave the sites around them unoccupied. Therefore, it leads in unstable phase or meta-stable phase where it could transform into the stable phase later according to kinetics or thermodynamics.

Figure 3.9a shows reconstructed volume of $\text{Cu}_{56}\text{Zr}_{44}$ annealed at T_2 . Cu and Zr have atomic ratio of 50:40 according to proxigrams. The nominal concentration of Zr-rich area indicated that it is a CuZr_2 while the nominal concentration of Cu-rich area indicated that it is a $\text{Cu}_{10}\text{Zr}_7$. In the area of inspection using TEM as shown in figure 3.10, two phases were found and identified in the $\text{Cu}_{56}\text{Zr}_{44}$ sample: $\text{Cu}_{10}\text{Zr}_7$ and CuZr_2 . The microstructure was predominantly occupied by $\text{Cu}_{10}\text{Zr}_7$ with grain size in range of 200-400 nanometers. CuZr_2 phase was formed near triple junctions and along grain boundaries with grain size less than 50 nanometers. Reconstructed atomic probe tomography was used to reconfirm the findings and to shed more lights on the formation of these two phases, however due to size of CuZr_2 phase in comparison to the APT tip size, such phase could not be captured in two APT tips that were investigated. From TEM, the most striking feature of the crystallization microstructure is $\text{Cu}_{10}\text{Zr}_7$. This agrees well with XRD experiments where they suggested that $\text{Cu}_{10}\text{Zr}_7$ is firstly crystallized then further decomposed into CuZr_2 with traces of $\text{Cu}_{10}\text{Zr}_7$ [33]. Although, with 10K/min cooling rate, the Zr-rich region seem to be CuZr rather than CuZr_2 [35, 36]. This could denote that $\text{Cu}_{10}\text{Zr}_7$ is the main crystallized phase where secondary phase is determined by the cooling rate of devitrification.

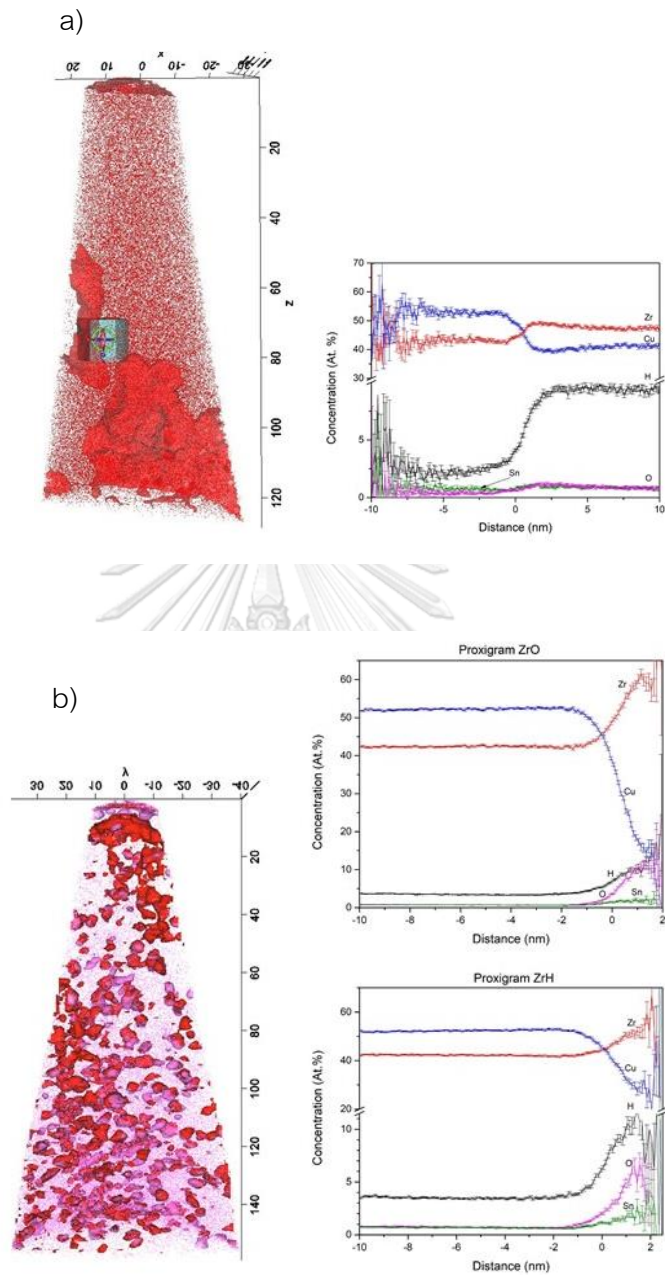


Figure 3.9: a) Reconstructed volume of $\text{Cu}_{56}\text{Zr}_{44}$ annealed at T_2 with Proximity histogram concentration profiles from selected volume of ZrH cluster b) Reconstructed volume of $\text{Cu}_{56}\text{Zr}_{44}$ annealed at 823 K with Proximity histogram concentration profiles from selected volume of ZrO cluster and Proximity histogram concentration profiles from selected volume of ZrH cluster

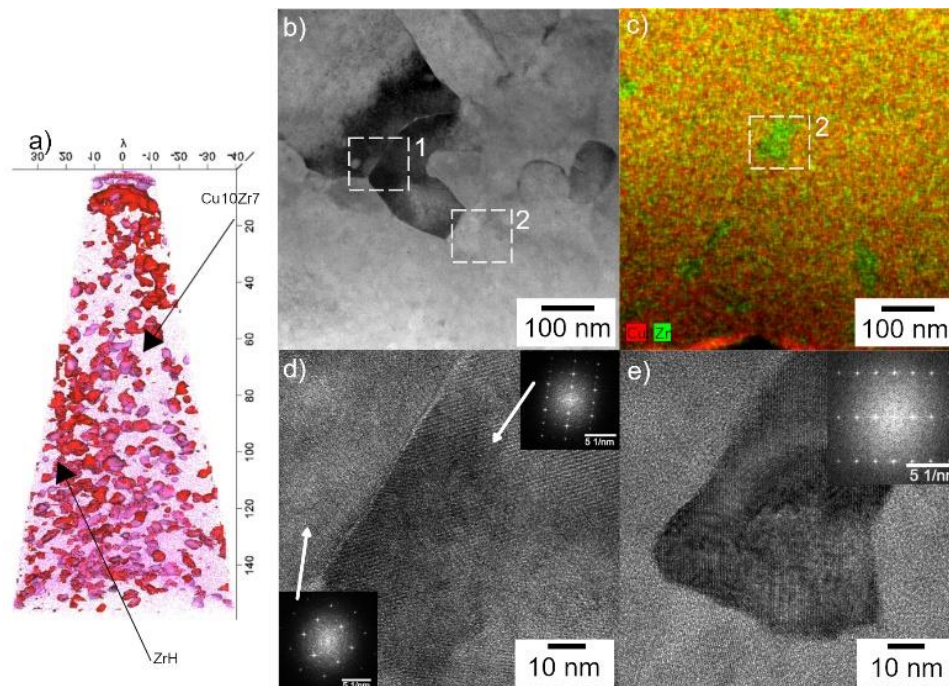


Figure 3.10: a) reconstructed APT of $\text{Cu}_{56}\text{Zr}_{44}$ b) TEM bright field of $\text{Cu}_{56}\text{Zr}_{44}$ c) EDS pattern of $\text{Cu}_{56}\text{Zr}_{44}$ d) HRTEM of $\text{Cu}_{56}\text{Zr}_{44}$ of the area enclosed in a box 1 in b) and an inset is an FFT pattern of the corresponding area. e) HRTEM of $\text{Cu}_{56}\text{Zr}_{44}$ of the area enclosed in a box 2 in b) and an inset is an FFT pattern of the corresponding area

Figure 3.11a shows reconstructed volume of $\text{Cu}_{50}\text{Zr}_{50}$ annealed at T_2 . Cu and Zr have atomic ratio of 50:50. The proximity histograms show ZrO (purple region) and ZrH (red region) clustered with CuZr matrix phase. From the 823 K annealing specimen as shown in figure 3.12, there are two more phases existed which are Zr-rich and Cu-rich region. Moreover, Sn was precipitated out of the solutions which could also be seen from EDX-TEM as shown in blue regions. Those 3 regions which are Sn-rich region, Cu-rich region and Zr-rich region, were Zr_5CuSn_3 , $\text{Cu}_{10}\text{Zr}_7$ and CuZr_2 respectively. From the EDX-TEM, it can be seen that Sn was precipitated out of Cu-rich region and formed a Sn-rich region as shown in figure 3.12. Precipitate of Sn is presence in the form of Stannide as Zr_5CuSn_3 [37]. With strong affinity of Sn and Zr, it was induced the Zr-rich region to formed around Sn-rich region as shown in figure 3.12c. The supper lattice-like structure was also observed in CuZr_2 crystal. Moreover, figure 3.12a shows good shows

good agreement between the APT reconstruction and measured feature sizes. The present of $\text{Cu}_{10}\text{Zr}_7$ and CuZr_2 are corresponding with previous studies [9, 10, 30, 33, 38-43]. The BF image in figure 3.12b confirms that there are a lot of black and grey crystalline particles with average size of 100 nm. From TEM observation, the Zr rich area formed similarly with $\text{Cu}_{64}\text{Zr}_{36}$. However, Sn crystal is much bigger at the boundary between those phases. Tim Cullinan et al. suggested that $\text{Cu}_{10}\text{Zr}_7$ phase grow from the solute balanced where it leads to shifting in the driving force which favoring the local formation of the CuZr_2 [42].

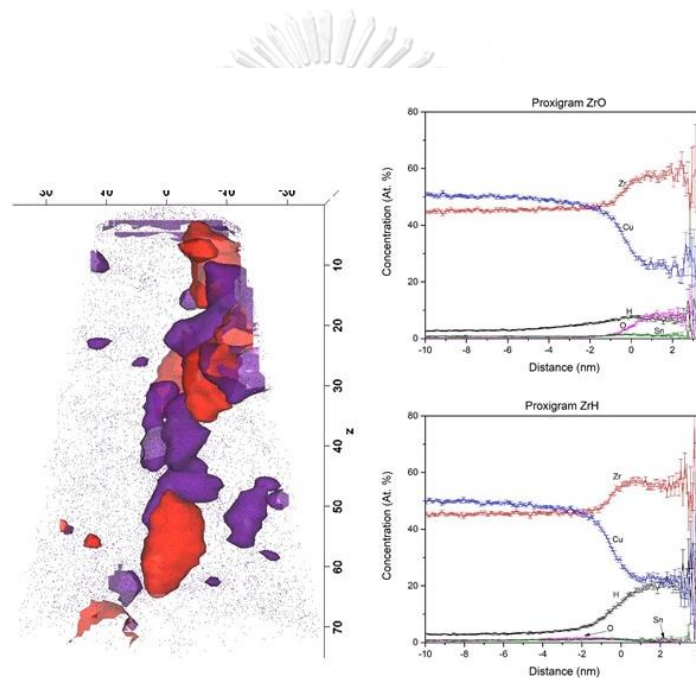


Figure 3.11: a) Reconstructed volume of $\text{Cu}_{50}\text{Zr}_{50}$ annealed at T_2
 b) Proximity histogram concentration profiles from selected volume of ZrO cluster
 c) Proximity histogram concentration profiles from selected volume of ZrH cluster

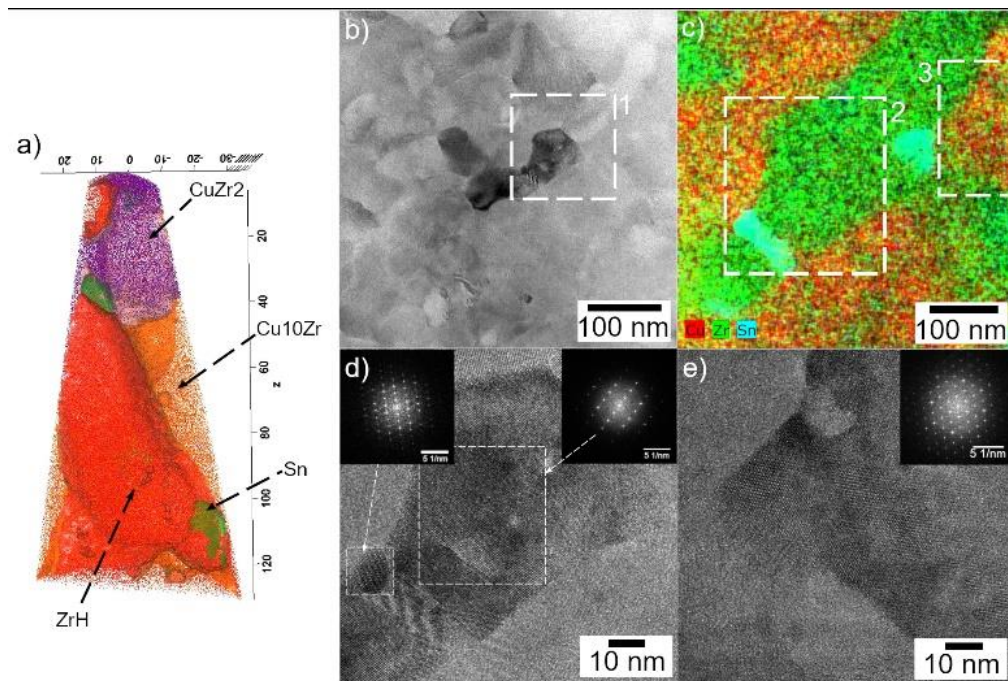


Figure 3.12: a) reconstructed APT of $\text{Cu}_{50}\text{Zr}_{50}$ b) TEM bright field of $\text{Cu}_{50}\text{Zr}_{50}$ c) EDS pattern of the area enclosed in a box 1 in b) d) HRTEM of $\text{Cu}_{50}\text{Zr}_{50}$ of the area enclosed in a box 2 in c) and an inset is an FFT pattern of the corresponding area. e) HRTEM of $\text{Cu}_{50}\text{Zr}_{50}$ of the area enclosed in a box 3 in c) and an inset is an FFT pattern of the corresponding area

In the constant heating rate with 10 K/min, the three phases ($\text{Cu}_{10}\text{Zr}_7$, CuZr_2 and CuZr) coexists after the temperature reach T_g while the CuZr phase start to decompose after the temperature had reached T_x [41]. As CuZr phase is metastable below 1002 K [10, 33]. Moreover, they also reported that the mechanism of crystallization in this $\text{Cu}_{50}\text{Zr}_{50}$ is the same for heating rates ranges from 10 to 60 K/min. The BF image confirms that there are a lot of black and grey crystalline spherical particles with average size of 100 nm. From TEM observation, the Zr rich area formed similarly with $\text{Cu}_{64}\text{Zr}_{36}$. However, Sn crystal is much bigger at the boundary between those phases. According to Braga et al., a $\text{Cu}_{50}\text{Zr}_{50}$ exists between $\text{Cu}_{10}\text{Zr}_7$ and CuZr phases. They are decomposed as the temperature decreased. First of all, the high temperature phases such as CuZr and Cu_2Zr are decomposed into Cu_8Zr_3 and $\text{Cu}_{10}\text{Zr}_7$ below 1,375 K and $\text{Cu}_{10}\text{Zr}_7$ and Cu_5Zr_8 below 1243 K. The Cu_8Zr_3 also decomposed into $\text{Cu}_{51}\text{Zr}_{14}$ and

$\text{Cu}_{10}\text{Zr}_7$ below 1,143 K, while Cu_5Zr_8 decomposed into $\text{Cu}_{10}\text{Zr}_7$ and CuZr_2 below 1,218 K [44]. On the other hand, CuZr , CuZr_2 and $\text{Cu}_{10}\text{Zr}_7$ were presented with the cooling rate of 40 K/min [30].

From all interested compositions, $\text{Cu}_{10}\text{Zr}_7$ phase seems to be the main crystallized phase which could act as a nanocrystal seed for crystallization [34]. Regardless of Sn, O and H contamination, the tolerance of recrystallization is dependent on the composition of the alloy. As $\text{Cu}_{50}\text{Zr}_{50}$ is the easiest to crystallize as the HRTEM image showed well-defined phase. This could be explained by the activation energy of crystallization where it increases with the copper content [45]. In addition, in term of packing density, $\text{Cu}_{50}\text{Zr}_{50}$ is less dense therefore it is easier for the atoms to diffuse around and rearrange themselves. The driving force for the phase separation could also be the difference in the affinity of Cu and Zr to Oxygen, Hydrogen and Tin. For example, Zr could preferentially forms oxide and hydride while repulsing Sn away. Although, with 10K/min cooling rate, the Zr-rich region seem to be CuZr rather than CuZr_2 [35, 36] This could denote that $\text{Cu}_{10}\text{Zr}_7$ is the main crystallized phase where secondary phase is determined by the cooling rate of devitrification.

3.1.3 Conclusion

In the current study, the crystallized sample showed uniform distribution of nanocrystallites. The characteristic of eutectic mode of crystallization imply the good glass forming ability of this alloy. The growth and coarsening regimes are observed, but not the nucleation and growth regimes.

Those small oxide clustered could acts as a nucleating site with a crystallite growing around it. As mentioned earlier that primary crystallized phase could be a meta-stable phase since the coordination of oxygen atoms could leave the sites around them unoccupied. Therefore, it leads in unstable phase or meta-stable phase where it could transform into the stable phase later according to kinetics or thermodynamics.

3.2 Kinetic Study of Binary Cu-Zr metallic glasses

Metallic glasses, in their amorphous state, can be evolved towards more stable crystalline phases by thermal annealing. Several multi-component metallic glass recipes with excellent glass-forming ability and high thermal stability have been developed in recent years due to their unique combinations of mechanical properties and ease of forming ability suitable for commercial applications. Bulk amorphous samples were produced via conventional solidification techniques at cooling rates as low as 1-100 K/s [47-50]. Vitreloids and related family of Zr-based and Zr-Cu-based alloys have attracted recent interests [51-56] due to their high resistance against crystallization as well as low critical cooling rates which opened up many new possibilities such as direct casting and thermoplastic forming.

Since the discoveries of Cu-Zr binary bulk metallic glasses, the Cu-Zr system has attracted research interests from fundamental perspectives [3, 57, 58]. In the Cu-Zr equilibrium phase diagram, the most probable crystallization products are CuZr_2 , $\text{Cu}_{10}\text{Zr}_7$, Cu_8Zr_3 and [30, 33, 59]. To investigate the thermal stability and crystallization behavior in the binary Cu-Zr metallic glasses, solid and liquid state phase transformations, as products of nucleation and growth, could reveal several important information regarding crystallization kinetics. The Johnson, Mehl and Avrami (JMA), a well-known transformation kinetics analytical description, could be applied to study phase transformation in metallic glasses [60-62]. The exponent or Avrami exponent, n , the overall effective activation energy, Q and the rate constant, K_0 can be determined according to nucleation and growth mechanism.

Differential scanning calorimetry (DSC) was utilized to determine characteristic temperature, thermal stability and to observe crystallization behavior in these materials by annealing in DSC chamber with controlled heating rate. The activation energy and Avrami exponent could be calculated by different models based on DSC data. Interestingly different research group reported different values for characteristic

temperatures as well as activation energy of crystallization as shown in table 3.3 for the same alloy compositions.

	T_g (K)	T_x (K)	DSC Heating rate (K/min)	Technique and details	Ref
$\text{Cu}_{50}\text{Zr}_{50}$	666	710	20	melt spinning	[63]
	677	724	10	splat quench	[46]
	667	701	10	Melt spinning	[64]
	-	735	10	melt spinning	[45]
	-	742	20	melt spinning	[45]
$\text{Cu}_{56}\text{Zr}_{44}$	682	724	20	melt spinning	[63]
	727	767	10	Splat quench	[36]
	688	725	10	Melt spinning	[42]
	-	756	10	Melt spinning	[45]
	-	768	20	Melt spinning	[45]
$\text{Cu}_{64}\text{Zr}_{36}$	737	776	20	Melt spinning	[63]
	-	791	10	Melt spinning	[45]
	-	798	20	Melt spinning	[45]

Table 3.3: Glass transition temperature, T_g and crystallization temperatures, T_c of amorphous $\text{Cu}_x\text{Zr}_{100-x}$ alloys of different processing history were reported in various values as obtained from DSC experiments

In the present work, different locations of three Cu-Zr melt spun ribbons of known compositions were investigated. Comparatively there were subtle changes in the shear strain rate values on the spun ribbon. The central region of the ribbon was compared to the outside to investigate the differences in characteristic temperatures. In

particular the $\text{Cu}_{64}\text{Zr}_{36}$ was found to be shear strain rate dependent as compared to $\text{Cu}_{56}\text{Zr}_{44}$ and $\text{Cu}_{50}\text{Zr}_{50}$ which were also studied in parallel. The analytic models were applied to investigate the crystallization kinetics of amorphous $\text{Cu}_{64}\text{Zr}_{36}$ alloy through the fits of JMA and Kissinger analytical models. Comparisons were made against experimental data obtained for both isothermal and isochronal DSC scans. Nucleation and growth modes during the crystallization and the separate activation energies for nucleation and growth were determined.

3.2.1 Methodology

Three alloys of nominal compositions $\text{Cu}_{50}\text{Zr}_{50}$, $\text{Cu}_{56}\text{Zr}_{44}$ and $\text{Cu}_{64}\text{Zr}_{36}$ were prepared by melt-spinning on copper roller at Eco-FM Company (Incheon, Korea). 75 mm wide by 75 μm thick ribbons were spun and rapidly solidified in argon atmosphere. The oxidation layers were removed prior to the experiments by mechanically wet grinding and washed in an ultrasonic cleaning bath. Characteristic temperatures were determined using Differential Scanning Calorimeter (DSC, NETZSCH5 STA 449F3) under argon atmosphere at flow rate of 40 ml min^{-1} . Along the width of a melt spun ribbon (x -direction), the liquid melt was ejected towards the center and as the liquid thinned and moved away from the center, the copper wheel surface exerted large amount of shear strain onto the sample. In particular, liquid moved in both x and y directions as shown in figure 3.13a experiencing more shear strain rate as the liquid moved away from the center.

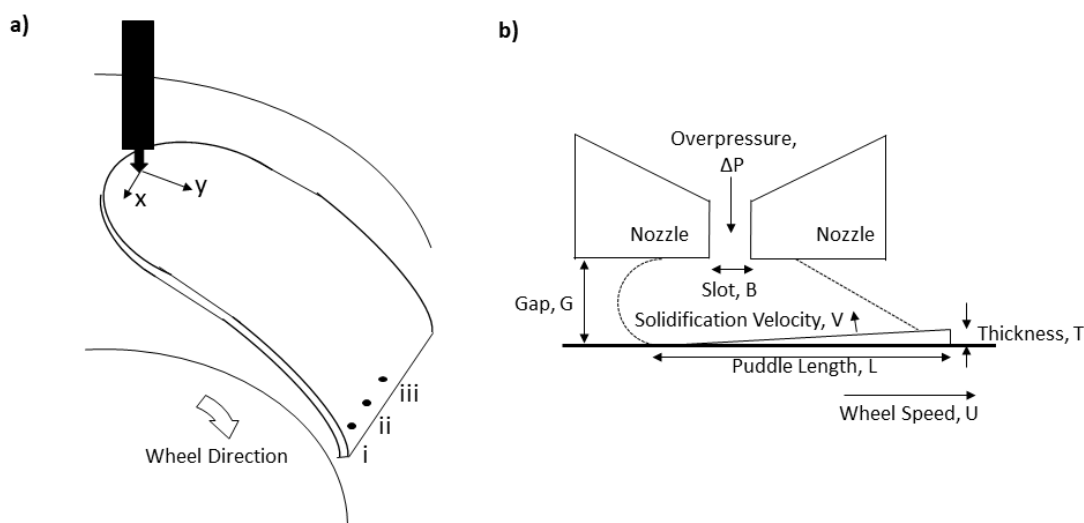


Figure 3.13: a) Schematic of melt spinning process with fluid flow in x and y directions with designated locations: (i) 2 mm away from the edge, (ii) midway between the edge and the center, and (iii) the center of the ribbon b) Side view schematic of spinning melt process at nozzle area (adapted from [65])

Specimens from melt spun ribbon that contained varying shear strain rates were obtained from different locations as shown in figure 3.13a. The specimens were taken from the following locations: (i) 2 mm away from the edge, (ii) midway between the edge and the center of the ribbon, and (iii) the center of the ribbon. Respectively the samples were labeled edge, quarter and center. Samples from three compositions were heated in a DSC at heating rates of 20 K/min. Only irregular response was found in the $\text{Cu}_{64}\text{Zr}_{36}$ melt spun ribbon in which shear strain rate may contribute to the shift in characteristic temperatures and enthalpy change profiles.

To further analyze the crystallization kinetic behavior of $\text{Cu}_{64}\text{Zr}_{36}$ in detail, samples were heat treated in the DSC under argon atmosphere at flow rate of 40 ml min^{-1} . Aluminum pans were used as sample holders. Baseline corrections during the experiments were conducted for all the DSC curves. Samples in the crystallization

kinetics study was characterized by DSC at heating rates of 10, 20, 30, 40 and 50 K/min. This set of experiments was regarded as isochronal kinetics study in the remaining of the paper. Isothermal kinetics study was also conducted in the same DSC using heating rate of 20 K/min to reach and hold at the following temperatures: 743, 748, 753, 758, 763, 768, 773, 778 and 783 K to observe the onset and completion of crystallization events.

Phase separation were studied under transmission electron microscopy (TEM) and laser-assisted local electrode atom probe (LEAP) investigation. High angle annular dark field (HAADF) Scanning transmission electron microscopy (STEM) observation was performed in TALOS F200X, FEI at an accelerating voltage of 200 kV. TEM specimens were prepared by Precision Ion Polishing System (PIPS, GATAN Model 691) with argon ion beam energy of 3 keV and the incident angle of 5° on liquid nitrogen stage. Chemical compositions were detected using LEAP (Cameca LEAP 4000X Si). The LEAP specimens were prepared by standard focused ion beam-based (FIB) lift out and annular milling protocol [66] with a radius of curvature at the tip of 100 nm using a FEI Helios Nanolab 600 dual-beam SEM/FIB. The final FIB clean-up procedure was carried out at 5, 3.5 and 1 kV to ensure the minimum Ga impurity. The operation parameters of the LEAP were set at temperature of 54 K, pulse rate of 250 kHz, pulse energy of 10 pJ and detection rate from 0.5-2%. The corresponding mass spectra was normalized to the counts of the $^{63}\text{Cu}^+$ peak. Basic tomographic reconstruction was performed using the Integrated Visualization & Analysis Software (IVAS 3.6.8) package (Cameca, USA).

3.2.2 DSC scans on different locations of melt spun ribbons

During melt spinning, the molten alloy was rapidly solidified on fast spinning copper roller. The melt experienced counteracting interactions from the roller forcing the fluid to translate, to rotate, to linearly strain, and to shear strain simultaneously. Towards the outer edge of the melt spun ribbon, the solidifying mass was subjected to higher

shear strain rate than the center of the ribbon as there is also a contribution from shear strain rate in the x direction (shown in figure 3.13a).

DSC heating scans of $\text{Cu}_{50}\text{Zr}_{50}$, $\text{Cu}_{56}\text{Zr}_{44}$ and $\text{Cu}_{64}\text{Zr}_{36}$ using constant heating rate of 20 K/min were shown in figure 3.14. Only $\text{Cu}_{64}\text{Zr}_{36}$ showed shear strain rate sensitivity in variations of DSC profiles as shown in figure 3.14c. As the shear strain rate was higher towards the edge, the width of the peak became broader. In addition, the inset of figure 3.14c revealed subtle differences in the onsets of glass transition suggesting possible relaxation in the short-range to medium-range order structure in $\text{Cu}_{64}\text{Zr}_{36}$. Onset of the glass transition temperature shifted to lower temperature as shear strain rate was increased. Tao et. al reported a similar trend in Zr-based amorphous alloys system of which T_g decreased with decreasing strain rate [51].

The melt spinning apparatus resembles that of rheometers with adapted geometries for measuring viscosity, shear modulus and other rheological quantities. Several publications reported on the rheological evidences of shear-assisted crystallization on simple and complex fluids such as polymer melts [67], colloidal glasses [64], bulk metallic glasses [68, 69], molecular liquids [70], etc.

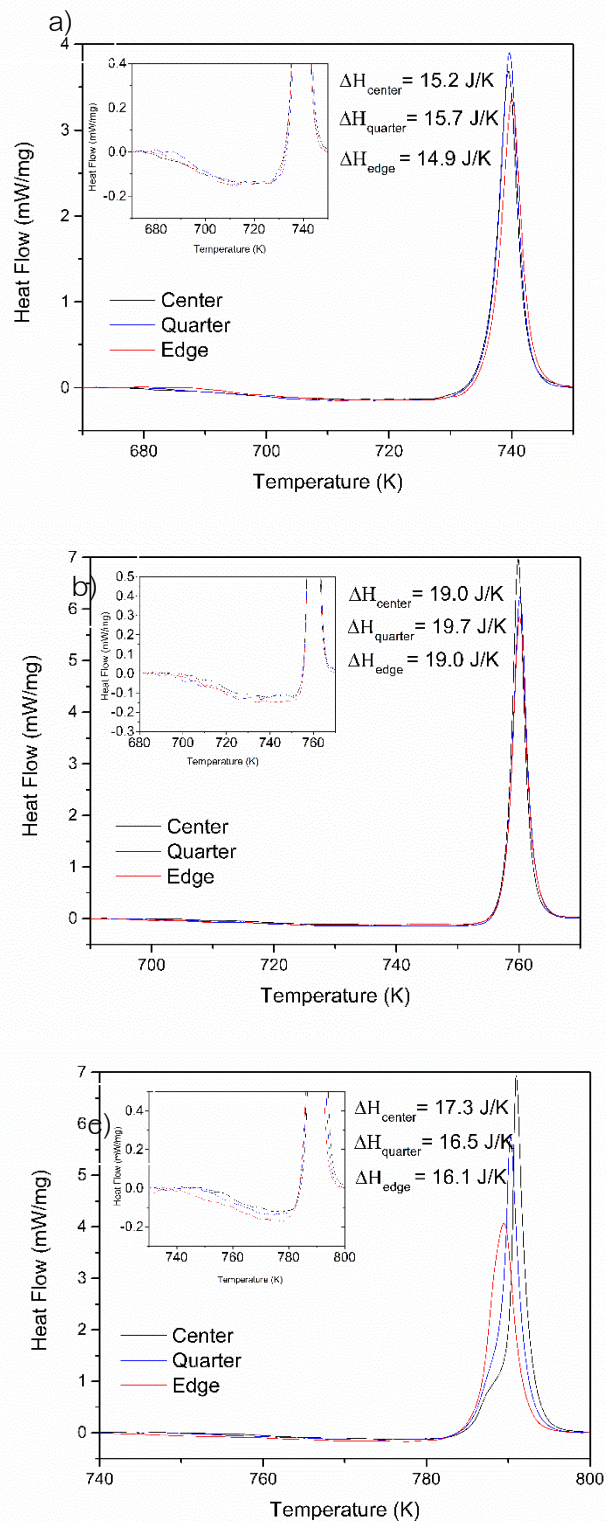


Figure 3.14: DSC heating curves from different locations of melt spun ribbons are displayed for the three Cu-Zr compositions: a) $\text{Cu}_{50}\text{Zr}_{50}$ b) $\text{Cu}_{56}\text{Zr}_{44}$ c) $\text{Cu}_{64}\text{Zr}_{36}$. The insets show the enlargement of region near T_g .

There have been several proposals to explain the complex problems of shear-induced crystallization. For example, shear is proposed to lower the energy barrier for nucleation and thereby expedite the growth of crystals. Ordering of inside constituents, e.g. micelles in micellar fluids or colloids in fluids, could result in crystallization through the effect of flow on the internal structure. Another proposal, applicable to simple fluids, puts emphasis on the phase separation driven crystallization. Readers are further referred to a physical review by Onuki on shear effects on physical fluids such as shear-induced demixing, nonlinear shear regimes, as well as mathematical treatments using computer simulations based on Ginzburg–Landau model [71].

As the fluid separates, crystallization kinetics may change abruptly in any highly sensitive fluids such as in bulk-glass forming liquids. The reported compositions for many bulk glass formers, such as the five components gold-based metallic glass [72], have already been fine-tuned for the highest glass forming abilities (GFA) with large critical casting thickness. However such gold bulk metallic glass exhibited strain rate induced crystallization in splat-quenched specimens of varying strain rates [68]. Way et al. [73] reported on shear rate and temperature dependence of viscosity in $Zr_{41.2}Ti_{13.8}Cu_{12.5}Ni_{10}Be_{22.5}$ alloy. Shear thinning as well as strong and fragile transition were found to be more sensitive in some bulk metallic glass systems as the liquids were subjected to Couette flow viscosity measurement. Glass forming compositions in binary Cu-Zr system is particularly narrow and is extremely sensitive to compositional change [63].

In particular, to investigate the anomaly in characteristic temperatures of $Cu_{64}Zr_{36}$ melt spun ribbons, this complex problem is further discussed with regards to (a) shear strain rate, and (b) crystallization kinetic studies.

3.2.3 Shear strain rate in melt spinning and planar flow casting (PFC)

To understand the extent of shear strain rate, various simulations and calculations of fluid flow for puddle formation in melt spinning technique as well as the velocity of fluid prior to leaving the puddle and begin to solidify were reviewed. The problem was known to be extremely complex to capture mathematically the shear strain rate values at different locations on the ribbon. The methodology required rigorous treatments of processing parameters and boundary conditions. Chen et al. [74] analyzed the fluid flow in 3-dimension using SOLA-VOF to show the difference in velocity profile along the cross-section surface (x-direction in figure 1a). RC Budhani et al. [75] also reported a velocity gradient along the cross-section based on mathematic analysis. Calculation by X.D. Hui et al. [76] predicted contour curve of the fluid velocity field in the melt puddle where it suggested the higher velocity in the middle of the wheel. This would induce the velocity of fluid flow before leaving the puddle to be higher than the surrounding. Z. Sun et al. calculated the heat transfer based on combined heat and momentum transfer model [77]. The model suggested decreased in thickness with increasing heat transfer coefficient. As the heat transfer of ribbon on the wheel is different along the x-axis, it would affect the local solidification rate. J.M. Kim et al. [78] employed Finite element methods to solve for dynamic of film casting, it showed that spinning film was slightly thinner at the edge. In summary, the shear strain rate difference was found to be the most prominent effect when compared to other parameters such as local solidification rate, ribbon thickness and heat transfer. The center region was exposed mainly to the fast spinning roller forcing the liquid melt to solidify instantaneously. As the liquid moved away from the center, the liquid melt experienced more shear and shear strain rate as now the contribution from both x and y shear directions.

3.2.4 Temperature dependent kinetic (Isochronal transformation)

The characteristic temperatures from DSC curves of $\text{Cu}_{64}\text{Zr}_{36}$ during continuous heating with different cooling rates were further experimented and shown in figure 3.15. Glass transition temperature (T_g), onset temperature of crystallization (T_x) and crystallization peak (T_c) were heating rates dependent in the range of investigation. As illustrated in figure 3.15, T_g , T_x and T_c increased with increasing heating rate. The enthalpy changes also increased with increasing heating rate.

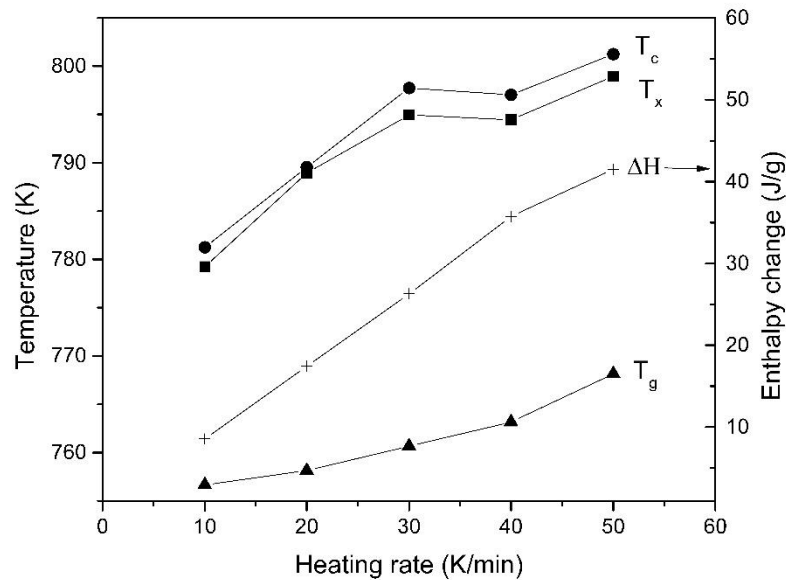


Figure 3.15: Characteristic temperatures: glass transition temperature (T_g), onset temperature of crystallization (T_x), crystallization peak (T_c) of $\text{Cu}_{64}\text{Zr}_{36}$ and enthalpy change of crystallization (ΔH_c) against various heating rate were recorded from DSC isochronal experiments. Lines are used for guide.

Since the T_g and T_c depend on heating rates, Kissinger equation can be employed to relate kinetics and activation energy. These characteristic temperatures were used in Kissinger equation [79]:

$$\ln \frac{R_h}{T^2} = -\frac{E}{RT} + \text{constant}$$

where R_h is heating rate, E is activation energy, R is gas constant and T is specific absolute temperature. Figure 3.16a shows relationship between $\ln(R_h/T^2)$ and $1/RT$, where slopes of the two straight lines shows the linear relationship between heating rates and the characteristics temperature. The calculated activation energies of crystallization (E_c) was 416.8 ± 29 kJ/mol. The error bars were calculated from the standard deviations of the linear fitting. Even though the T_g can be linearly approximated by Kissinger equation, the value retrieved from the equation may be more meaningful for first order transition. Moreover, the Kissinger equation was first developed in order to explain the reaction kinetics in term of heat absorption. The relaxation kinetics between T_g and T_c cannot be measured in term of reaction rate, and the activation energy of T_g cannot be calculated using the Kissinger equation. Ruitenberg [80] utilized the change of defects rate in the bulk materials for the Kissinger analysis. With additional assumptions, authors concluded that the adapted Kissinger equation was only valid at the slow heating rates.

Isochronal crystallization, crystallized volume fraction of bulk metallic glass (α) from metastable state to crystalline phase may be calculated from area under DSC curves according to following equation:

$$\alpha = \frac{\int_{T_0}^T \left(\frac{dH_c}{dT}\right) dT}{\int_{T_0}^{T_\infty} \left(\frac{dH_c}{dT}\right) dT} = \frac{A_0}{A_\infty}$$

where T_0 and T_∞ are the temperatures at which crystallization begins and ends in amorphous materials. A_0 and A_∞ are the area under the DSC curves, respectively.

The rate of enthalpy change, $d\Delta H/dt$, led to values for the cumulative transformation enthalpy change during the annealing or heating stage. As shown in figure 3.16b, the slope of crystallization fraction is decreased as cooling rate is increased, hence it can be implied that the faster the cooling rate, the slower the transformation.

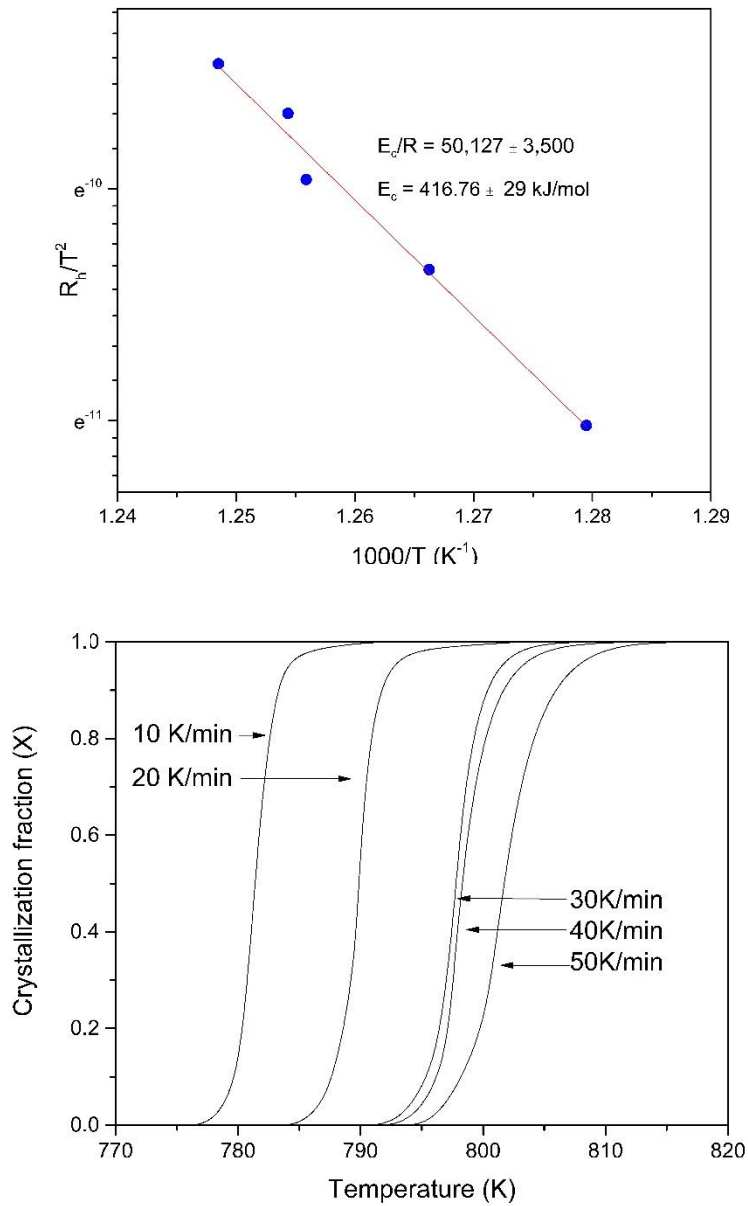


Figure 3.16: a) Calculation of activation energy for glass transition and crystallization of $\text{Cu}_{64}\text{Zr}_{36}$ using Kissinger Plot from T_g and T_c . b) Crystallized fraction curves as a function of temperature at different heating rates

3.2.5 Time dependent kinetic (Isothermal transformation)

The isothermal kinetics was characterized by annealing the samples at constant temperatures ranging from 743 - 788 K. The DSC traces were shown in figure 3.17a. All the DSC traces exhibited single exothermic peaks after a certain incubation period. With increasing annealing temperature, the apparent incubation time decreased as shown in figure 3.17b as there were nanocrystals or short-range order cluster of atoms in the amorphous matrix after certain period of annealing as was observed in Cu-based metallic glass BMGs [81]. Time before the crystallization transformation may be stated as time lag, τ_{tr} , which described the time needed to establish a steady-state nucleation rate. This incubation time would disappear if the specimen is pre-annealed at higher temperature as seen in the $Zr_{50}Al_{10}Ni_{40}$ amorphous system [82].

In the case of isothermal annealing, the activation energy for crystallization of an amorphous alloy is evaluated by the Arrhenius equation;

$$t(x) = t_0 \exp \left[\frac{E(x)}{RT} \right]$$

where t_0 is a constant for time, $E(x)$ is the activation energy for crystallization with the transformed volume fraction x and R and the gas constant. The plot of $\ln t(x)$ against $1/T$ at a given crystallization volume fraction (x) yielded a nearly straight line with a slope of $E(x)$ equal to 775.4 kJ/mol as shown in figure 3.18a. Crystallization fraction can be calculated in the same way as in the case of isochronal treatment and results are shown in figure 3.18b. Relationship between the crystallized volume fraction and annealing time during isothermal crystallization process of the metallic glass was demonstrated. With an increase in annealing temperature, the annealing time decreased with steeper slope of sigmoid curves. As crystallized volume fraction increased sharply, thus implying the rapid proceeding at the rest of crystallization process. The calculated activation energy from isothermal kinetics study was larger than the value calculated from Kissinger plot in isochronal kinetic study. The disparity was also observed in other metallic glass systems [83-85]. One possible hypothesis could be the fact that the crystallization temperature

during isochronal kinetics study was higher than the isothermal kinetic study, this could advance the crystallization from metastable state into crystalline phases. The activation energy in isochronal kinetic study is typically lower than that in isothermal kinetics study.

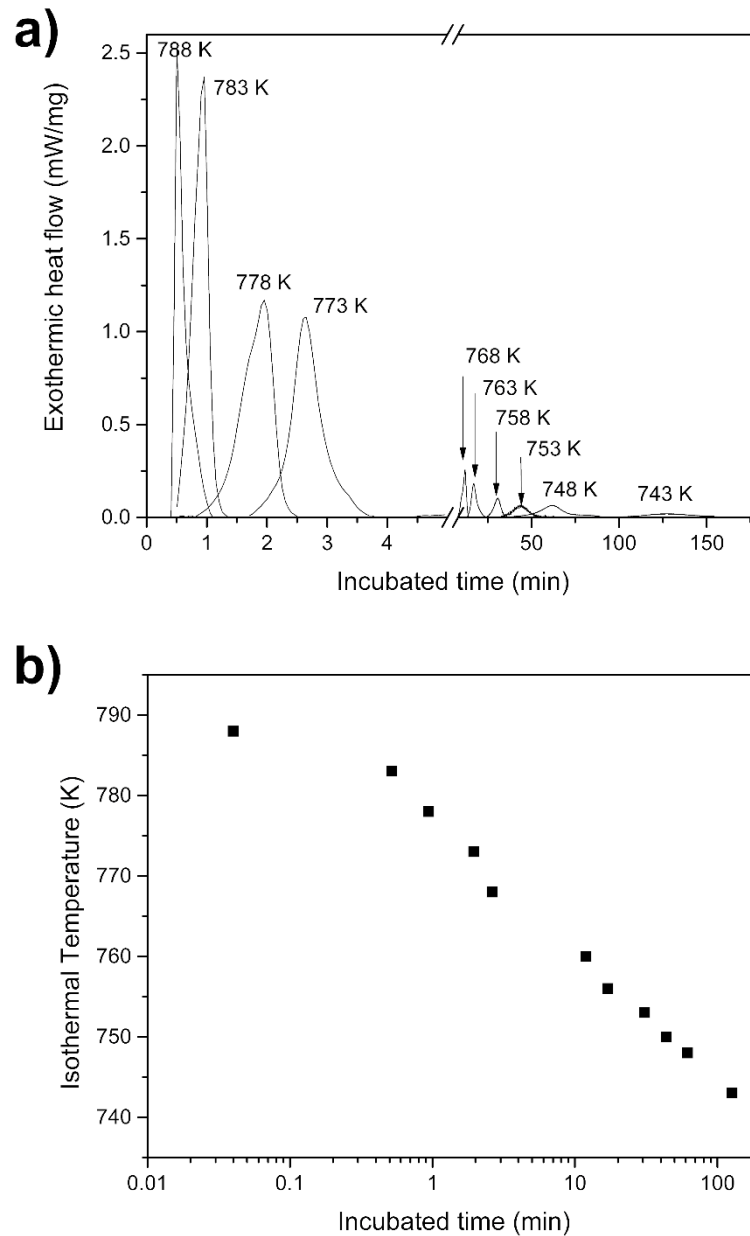


Figure 3.17: a) Crystallization peaks during Isothermal heat treatment in DSC of $\text{Cu}_{64}\text{Zr}_{36}$ at different annealing temperatures. b) Isothermal temperature against incubated time under isothermal transformation

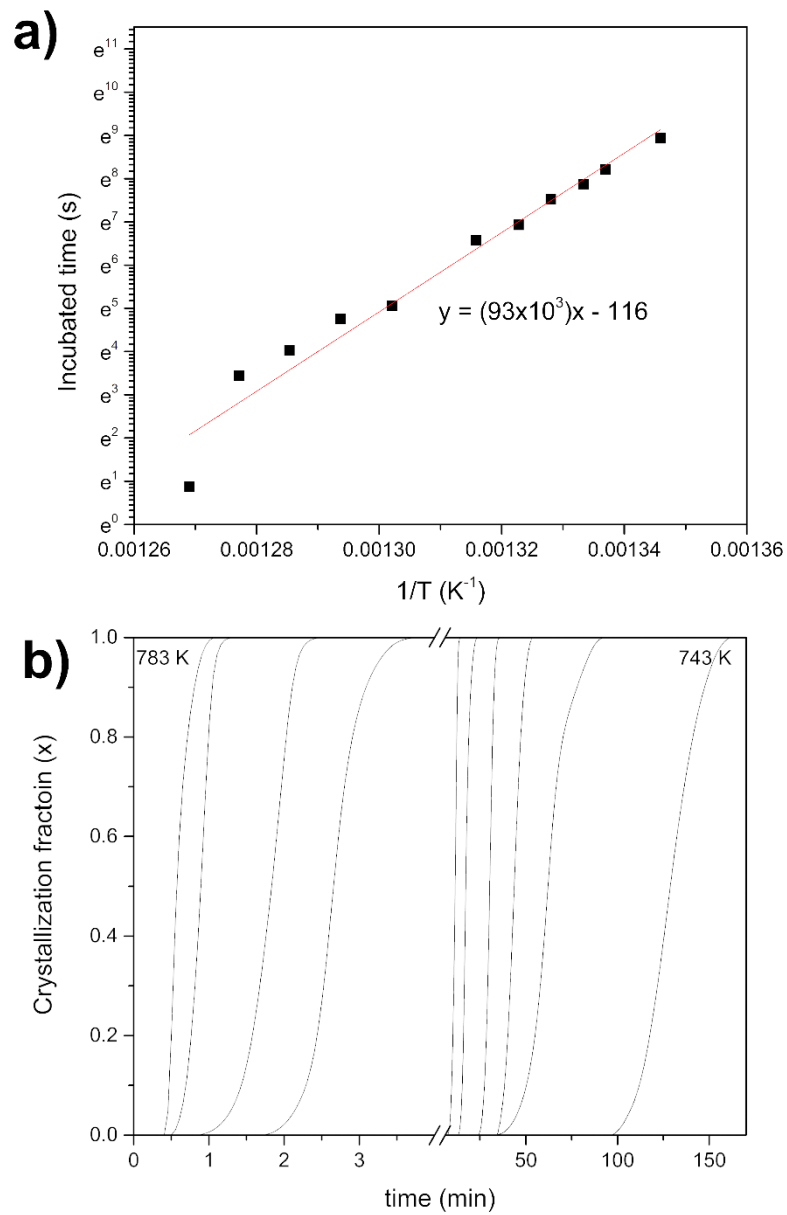


Figure 3.18: a) Calculation of activation energy for crystallization in isothermal annealing using Arrhenius equation. b) Crystallization fraction under different isothermal annealing temperature starting from the left at 783 K and decreasing at 5 K increment.

Johnson-Mehl-Avrami (JMA) analysis can be applied to the crystallization process under isothermal conditions to clarify the nucleation and growth mechanisms during crystallization. The avrami exponent (n) can be estimated from

$$x(t) = 1 - \exp(-|K(t - \tau)|^n),$$

where $x(t)$ is the crystalline volume fraction at different annealing time, t , and finally τ is the incubation time. By plotting of $\ln[-\ln(1-x(t))]$ against $\ln(t - \tau)$ at various temperatures between $0.2 < x(t) < 0.8$, the kinetic exponent, n can be determined as shown in figure 3.19. The slopes were approximately 3 which corresponded to the growth of small particles with an increasing nucleation rate. The kinetics of crystallization behaved similarly in the temperatures investigated. The incubation time decreased with increasing annealing temperatures. As the graph shifted to the right, in figure 3.19, the nuclei size became smaller as the annealing temperature decreased. The behavior is common to binary bulk glass forming systems of which devitrification is extremely sensitive to compositional change. In the case of $\text{Cu}_{64}\text{Zr}_{36}$ alloy composition, the following three line compounds were typically reported as crystallization products: $\text{Cu}_{51}\text{Zr}_{14}$, $\text{Cu}_{10}\text{Zr}_7$ and Cu_8Zr_3 [9, 38]. As crystallization of metallic glasses is believed to be a competition process among the phases, without direct observation technique it is unreliable to define primary crystallized phases. Cui et al. [86] suggest $\text{Cu}_{10}\text{Zr}_7$ to be the primary crystallized phase through X-ray diffraction investigation. In a related alloy system based on Zr-Cu-containing, $\text{Zr}_{41.2}\text{Ti}_{13.8}\text{Cu}_{12.5}\text{Ni}_{10}\text{Be}_{22.5}$, Mridha et al. [87] found evidence of primary nucleation of a metastable icosahedral phase followed by eutectic mode of crystallization in atomic probe microscopy. The icosahedral was richer in Ti, driving the matrix to be Ti-depleted and the supercooled liquid would crystallize into competing eutectic phases. This was not the case in our present study.

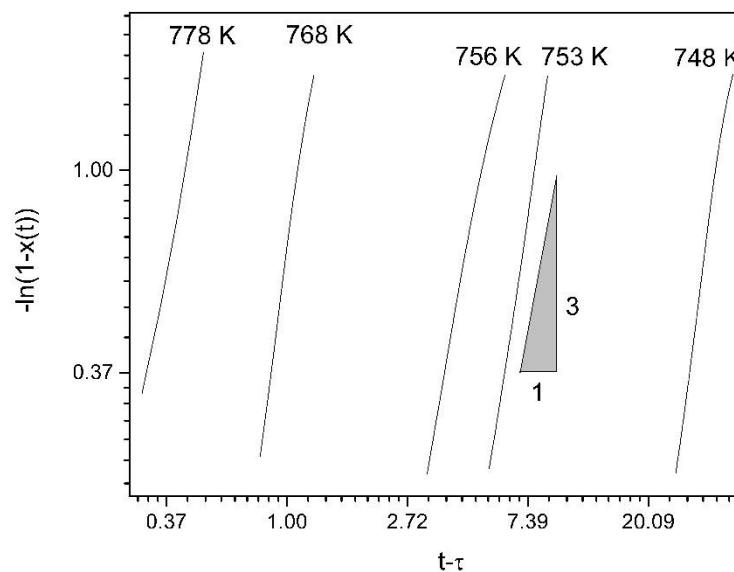


Figure 3.19: Johnson-Mehl-Avrami analysis at different annealing temperatures with crystallization fraction ranging from 0.2-0.8 under isothermal conditions.

Figure 3.20a and b show reconstructed tip of 770 K-annealed $\text{Cu}_{64}\text{Zr}_{36}$ with $30 \times 30 \times 30 \text{ nm}^3$ analyzed volume and the corresponding concentration profile in z-axes, respectively. Such annealing temperature was higher than T_g but lower than T_x . Uniform distribution for both Cu and Zr was observed. The concentration profile confirmed the atomic ratio of the sample which was closed to 64 at.% Cu and 36 at.% Zr. Figure 8c showed fully amorphous structure without evidence of clustering nor phase separation.

Phase separation in metallic glass was observed in various systems [69, 88-90]. As the anomaly in DSC curves suggested, the best glass former composition, $\text{Cu}_{64}\text{Zr}_{36}$ has the strongest shear strain rate dependency. The shift in T_g and change in DSC profile may originate from short range ordering that was beyond detection limits of HAADF-STEM and LEAP. This corresponded well with figure 3.20 where phase separation was not detected.

In addition, the DSC anomaly of $\text{Cu}_{64}\text{Zr}_{36}$ could suggest a competing crystallization event after 783 K. According to JMA analysis, only after 783 K, the MG

started to crystallize. This would drive the change in local chemical composition where it could accelerate nucleation process.

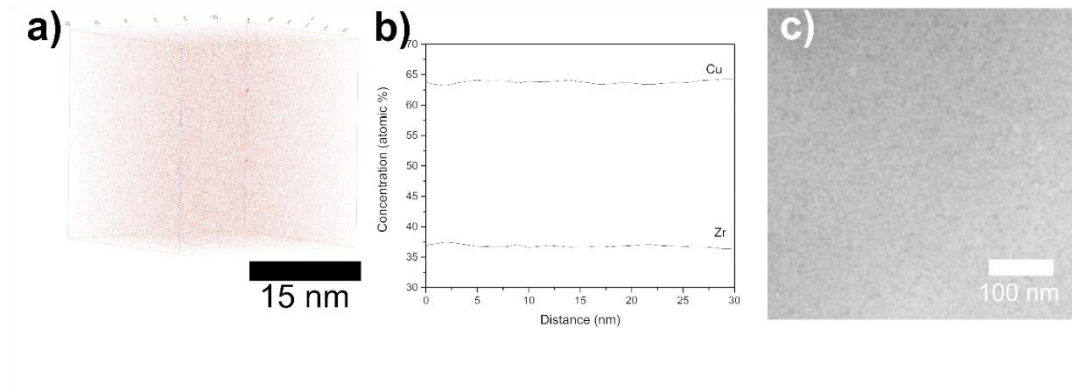


Figure 3.20: $\text{Cu}_{64}\text{Zr}_{36}$ annealed at 770 K a) Atom probe reconstruction b) Concentration profile c) HAADF-STEM image

3.2.6 Conclusions

Kinetics of crystallization in $\text{Cu}_{64}\text{Zr}_{36}$ metallic glass was studied by DSC in both isothermal and isochronal transformation modes. It was found that in isochronal crystallization, the average value of activation energy, determined using the Kissinger plot is 417 kJ/mol, while the activation energy in isothermal crystallization is 775 kJ/mol. The difference in the crystallization kinetics was thought to originate from the differences in the atomic mobility. The JMA analysis was applied in isothermal crystallization. Avrami exponent, n is close to 3 which indicate the growth of small particles with an increasing nucleation rate. High shear strain rate could induce crystallization in $\text{Cu}_{64}\text{Zr}_{36}$ alloy system. We found no evidence of phase separation as shown in the HAADF-STEM and LEAP analysis.

3.3 Observation of hydrogen artefacts during sample preparation and atomic probe tomography

Atom probe tomography (APT) has been used in a variety of experiments due to its accuracy in the ability to analyze chemical composition together with atomic arrangement. APT usage is now getting more and more popular despite the fact that sample preparation is tedious. This special technique has gained attentions due to its inherent capacity to detect light elements such as hydrogen and oxygen. However, the accuracy of the hydrogen detection by APT microscope was still questioned by the presence of residual hydrogen in the ultra-high vacuum chamber of APT microscope as well as hydrogen introduction during the sample preparations. The presence of hydrogen generates noise in the data, as the hydrogen atom may be adsorbed onto the tip, and subsequently migrate towards the specimen apex and get ionized.

To verify this, the material with high hydrogen affinity should be used in the experiment. The Cu-Zr binary amorphous alloy is introduced to the experiment to track the source of hydrogen contamination. The amorphous alloy was chosen due to its simple binary chemical composition and amorphous background suitable for identifying formation of new crystals during high resolution transmission electron microscope (HRTEM) investigation. It has been observed that Zr-based amorphous alloy has shown abundance of hydrogen diffusion and permeability with higher concentration of Zr yielded higher hydrogen permeability [91]. Hydrides are usually observed in Zr-based amorphous alloy due to its high hydrogen diffusivity and high hydrogen solubility [91, 92]. The undesired hydrogen that got introduced during the sample preparations could further complicate the study of hydrogen introduction and hydride formation in Zr alloys. As a result, focused ion beam (FIB) technique is recommended for preparing specimens for microscopic investigations such as Transmission Electron Microscope (TEM) and APT. However, FIB milling introduces structural defects and undesired artifacts because of beam-induced damage [93-95]. On the one hand, many studies have found that there is a high tendency for specimen preparation performed by FIB

milling at room temperature could lead to undesired hydrides, but on the other hand many research groups qualitatively show that FIB conducted on the cryogenic-FIB will prevent undesired hydrogen pick-up so hydride formation will not occur during sample preparation [96-98]. There have been limited quantitative investigations on the difference of hydrogen pick-up in the aforementioned techniques.

Hydrogen entrapment is energetically favorable at lattice defect in the crystal. They could be along the grain boundaries, dislocation cores, nanovoids or point-defects. Hydrogen can present in metals in the form of solution, trapped at crystal defects or in the form of hydrides. If sufficient Hydrogen is present or if the solubility limit of H in Zr is low, then Hydrogen could precipitate and form Zirconium hydrides. Typically the hydrides would form at room temperature since the solubility of hydrogen in zirconium is below 10 wt ppm at room temperature [99]. Hydrogen in Zr metal can appear in many forms of hydride (such as ζ , γ , δ , and ϵ) and in solid solution [100]. The phase diagram of Zr-H system shows at least four ZrH_x phases at temperatures below 550 °C where hexagonal (HCP) ζ - ZrH_x with $x=0.25-0.5$, a face-centered tetragonal (FCT) γ - ZrH_x with $x=1$, a face-centered cubic (FCC) δ - ZrH_x with $x=1.5-1.65$ and another FCT ϵ - ZrH_x with $x=1.75-2$ [100, 101].

This study is aimed at using FIB to prepare sample for TEM and APT. The focused of the study is to observe the hydrogen content in APT data as well as compare it with TEM investigation and to understand hydride formation by providing a direct comparison between cryo-stage FIB and conventional FIB.

3.3.1 Results and Discussion

Both samples were heat treated at temperature between T_g and T_x in order to transform the materials from relaxed glass into metastable equilibrium by closely observing the enthalpy change.

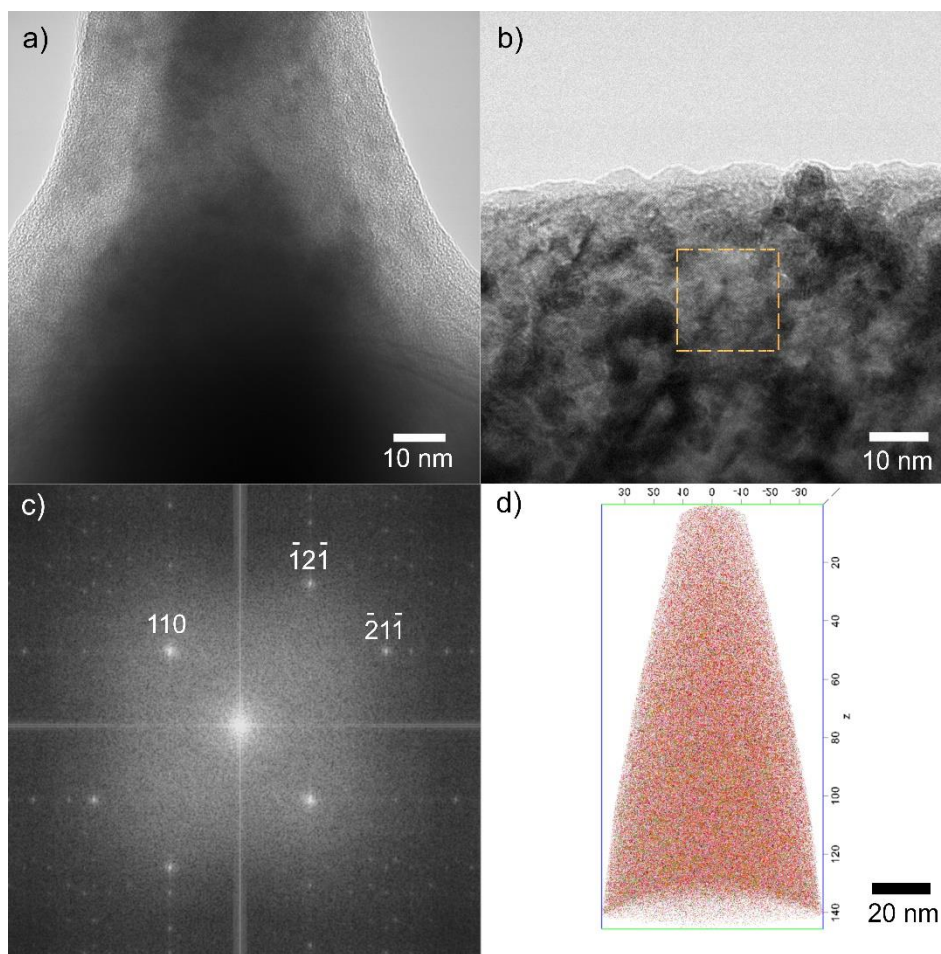


Figure 3.21: a) HRTEM image of $\text{Cu}_{64}\text{Zr}_{36}$ heat treated at 768 K prepared by FIB before running a LEAP experiment. b) TEM micrograph $\text{Cu}_{64}\text{Zr}_{36}$ annealed at 768 K prepared by FIB after running a LEAP experiment. c) FFT pattern obtained from the box shown in figure 1b. d) Reconstruction APT of $\text{Cu}_{64}\text{Zr}_{36}$ heat-treated at 768 K

Figure 3.21 illustrates the comparison of $\text{Cu}_{64}\text{Zr}_{36}$ sample before and after running a LEAP experiment. Figure 3.21a illustrates the HRTEM micrograph of the sample before the experiment where an amorphous structure with short range order was indicated. There was no nanocrystals observed. The dissimilar contrast observed in the nanotip was caused by the difference in thicknesses of the tip. On the other hand, figure 3.21b illustrates the HRTEM micrograph of the sample after the experiments. It shows evidence of crystallization in the sample. The dark contrast zones observed in figure

3.21b could be caused by inhomogeneous thinning or by composition contrast. The observed dark contrast zones are more likely to be caused by inhomogeneous thickness after the specimen was investigated in APT chamber. This is due to the reason that the roles in the HRTEM micrograph, figure 3.21b, is consistent between dark contrast zones and lighter contrast zones. From the FFT image analysis, the heat treated $\text{Cu}_{64}\text{Zr}_{36}$ revealed small crystalline particles which were indexed as ZrH_2 and shown in figure 3.21c. The $\delta\text{-ZrH}_2$ was confirmed by $[0\bar{1}\bar{3}]$ zone axis identification. The $\delta\text{-ZrH}_2$ is tetragonal with lattice parameters of 0.465 nm (a) and 0.517 nm (c) [102]. $\delta\text{-ZrH}_2$ is also found to be a cause of phase separation in Cu-Zr binary alloys [45]. However, the $\delta\text{-ZrH}_2$ was not observed in the LEAP data. The hydride in the LEAP data was identified as $\gamma\text{-ZrH}$ which was a metastable phase. Figure 3.21d shows full reconstructed APT tip of approximately 20 million ions where it was superimposed of all the major elements. The tip shows uniform distribution of elements without any evidence of crystallization or nano-clusters. This indicates that the hydrogen was diffused into the sample before the LEAP experiment. However, the energy from laser during LEAP could induce the formation of $\delta\text{-ZrH}_2$. As G.Sha et. al has discussed the formation of $\delta\text{-ZrH}_2$ through decomposition and partitioning of the alloy [103]. In addition, it was also discovered that $\gamma\text{-ZrH}$ can be transformed to stable $\delta\text{-ZrH}_2$ with appropriate time and temperature [101].

The source of hydrogen could be from the APT chamber itself. The flux of hydrogen (F) to a nanotip specimen was calculated based on the classic gas kinetic factor times and enhancement factor due to the polarizability of H_2 , as expressed elsewhere [29]. Values apply in the equations were as followed: $\alpha_{\text{H}} = 8.76 \text{ C}^2\text{m}^2/\text{J}$ [29], $E = 28 \text{ V/nm}$ for Zr [104], the partial pressure of H_2 assumes two orders of magnitude less than the total pressure which was 6.53×10^{-11} Torr in the UHV chamber, hence, $p_{\text{H}_2} = 6.53 \times 10^{-13}$ Torr, $T = 54 \text{ K}$ and $\eta = 1$ as it was assumed monolayer. These values give $F = 2.21 \times 10^{13} \text{ molecules/m}^2/\text{s}$. Consequently, the time for monolayer coverage is roughly 2 hours where the LEAP experiments were ran for 1 hour with 1.5% detection rate. The

calculation demonstrates that part of hydrogen source could be from the residual gas in LEAP analysis chamber.

The local enrichment of hydrogen is necessary for the precipitation of hydrides in Cu-Zr alloy. However, the diffusivity of the metal atoms is very small at room temperature. The other possible sources of hydrogen are water or acid solution used during mechanical grinding. The hydrogen content in the bulk materials should be lower than those measured by APT. Hydrogen was likely introduced during the preparation of specimens. Rengen Ding et al. [105] noticed greater number of hydrides in the specimens etched with acid solution than in dry mechanical grinding specimens. Rengen Ding et al. [105] further reported that the hydrogen concentration in their titanium specimen was increased after cleaning with acid and acetone. Additionally, hydrogen in FIB chamber could be generated from platinum deposition where it was employed as a protective coating. The Pt organometallic gas precursor used in the Helios 650 FIB system is trimethyl (methylcyclopentadienyl) platinum (IV) [106]. The reaction of the gas precursor can be expressed as [106]: $MeCpPt^{IV}Me_3(Precursor) + e^- \rightarrow PtC_8(Adsorbed PtC_x film) + H_2(gas) + CH_4(gas)$. Therefore, it can be assumed that another source of hydrogen during FIB preparation could be the hydrogen gases generated by ion beam irradiation of the gas precursors used for Pt-deposition.

$Cu_{56}Zr_{44}$	Cryo-stage FIB	Conventional FIB
Y-ZrH	4.99	6.83
Diffuse H	3.89	7.15

Table 3.4: The hydrogen contents of $Cu_{56}Zr_{44}$ nanotips prepared by cryogenic stage FIB and conventional FIB (all numbers are expressed in atomic weight)

Moreover, FIB is a technique that sputtered particles out, it would result in the formation of defects, phase transformation or even the formation of a new phases. These clusters or dislocations could cause the atoms to rearrange or even provide nucleation sites for the hydride precipitation. The most important criteria in FIB is the temperature given that the specimen temperature could be critical. In the next part, $\text{Cu}_{56}\text{Zr}_{44}$ metallic glass was used to study the effect of temperature during LEAP nanotip preparation. The sample from Cryo-stage FIB were compare with sample from conventional FIB. The parameters and protocol were identical in both FIBs. The reconstructed data from LEAP showed that there are two types of hydrogen in the nanotips, namely diffused hydrogen and Zr-Hydride. The diffused hydrogen refers to as free hydrogen that was detected from the 1-Da peak in mass-to-charge spectrum. It is possible that the adsorbed hydrogen was field evaporated in molecular form such as $\gamma\text{-ZrH}$. As shown in table 3.4, both diffused Hydrogen and $\gamma\text{-ZrH}$ were lower in the tip prepared by cryogenic stage FIB. Many researchers have investigated the hydrogen diffusion induced by FIB [97, 107]. Other studies were also observed the smaller quantity of Hydride and lower depth of hydrogen penetration [108].

It is clear that Zr is prone to form hydrides. $\delta\text{-ZrH}_2$ is considered as most stable at room temperature. While the metastable $\gamma\text{-ZrH}$ could form under conditions of fast cooling rates with hydrogen diffusion alone [109]. This phenomenon could occur by hydrogen atoms aggregation at interstitial sites in the zirconium lattice where it could promote the nucleation of dislocations or misfits required for the transformation.

Hydrogen trapping by zirconium metal alloy was commonly observed in Zr-containing amorphous [103]. When Hydrogen molecules arrive at a surface of the specimen, they dissociate into hydrogen atoms. Hydrogen may come from decomposed residual hydrocarbons and moisture as a by-product of gallium ion beam [106]. Owing to the high affinity of Zr for Hydrogen and rapid diffusion of hydrogen, uptake of atomic hydrogen into the matrix was expedited. They dissolve and diffuse in Cu-Zr alloy in the form of interstitial solid solution. Since Zr has higher affinity with hydrogen as compared to Cu, diffused hydrogen preferentially concentrates around Zr atoms. When the

temperature was increased to 823 K, Cu and Zr atoms diffused and coarsened. Cu-rich region and Zr-rich region were formed, and some hydrogen atoms were impelled out. With this locally concentrated hydrogen, ZrH started to form cluster and precipitate into γ -ZrH due to its thermodynamic preference for precipitation [110]. Carpenter et. al [109] proposed that the precipitation of γ -ZrH can occur in Zr by means of hydrogen diffusion together with shear transformation caused by the glide of Shockley partial dislocations on alternate basal planes. However, in this study, the physical transformation could be caused by atomic arrangement such as during the devitrification process of metallic glass. Furthermore, the laser pulse energies used in LEAP experiment as well as the partial pressure of H_2 in the vacuum system had influences on the behavior and concentration of H and γ -ZrH. The greater laser pulse energy, the higher temperature of the specimen tip was observed, and subsequently in turn led to more hydrogen atomic mobilities. The hydride forms were also observed in LEAP with laser mode experiment [111]. As there was no hydride observed in TEM, it could be deduced that the hydride was induced in the APT chamber. Moreover, from previous study, the hydride were formed more in the FIB-prepared sample [112, 113]. This could imply that significant amount of H were introduced during the annular milling procedure.

3.3.2 Conclusions

High hydrogen-affinity alloy such as Zr-alloy or Ti-alloy are prone to hydrogen pick-up during sample preparation. This could lead to ambiguous microstructural characterization as well as chemical composition analysis.

Our investigation showed systematic quantitative evidences of three main possible sources of hydrogen. First, hydrogen could be introduced during wet mechanical grinding, where water, polishing solution and etchant could be sources of hydrogen. Second, the precursor of Pt used in FIB technique could also be another possible source. Lastly, the hydrogen could be introduced from the analysis chamber itself during the LEAP experiment. To the best of our knowledge, it could be a

combination of hydrogen sources together with laser energy during LEAP experiment, that lead to formation of hydrides. While the hydrogen content could be reduced by using cryogenic stage instead of conventional FIB. This is another evidence that hydride formation in amorphous is sensitive to energy used.

In order to reduce hydrogen uptake during sample preparation, using water-free and acid-free methods for mechanical and chemical polishing as well as using cryo-stage FIB to limit the hydrogen diffusion during preparation.



Chapter 4

Creep deformation investigation on tin-based alloys

4.1 Physical property of lapping plate

4.1.1 Microstructure of Sn-Bi alloy

Microstructure of lapping plate was studied under optical microscope. Different between forged and non-forged Sn-1 wt.% Bi alloy was studied. Sections of lapping plate were EDM wire-cut out of the 17" plate in a rectangular shape with thickness of 3 mm. Different directions of plate on inner diameter (ID), middle diameter (MD) and outer diameter (OD) was observed. Each direction is called A, B and C according to figure 4.1. These sample were then ground with 400, 600, 800, 1200, 2000 grid number of SiC paper then followed by polishing with alumina powder. Afterward, they were etched with 2%HCl in Ethyl alcohol. Photographs were then taken under optical microscope. Grain size of the forged and non-forged Sn-1 wt.% Bi was measured from the photographs using the E112 intercept method from ASM metals handbook. The intercept was drawn three times on each photograph to normalize the error of human eyes. Three photographs were taken from each direction (A, B and C).

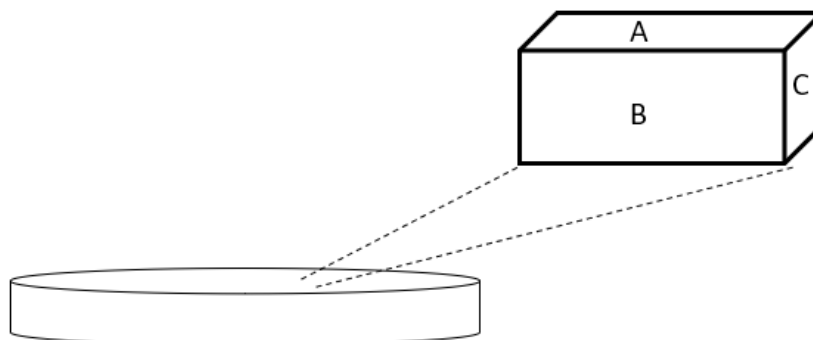


Figure 4.1: Dimensional presentation of sample with directions: A as surface facet, B as longitudinal facet and C as cross-sectional facet

Figure 4.2 shows the average grain size measurement in different direction and different location on the plate. It can be seen that grain size of non-forged Sn-1 wt.% Bi is larger than forged Sn-1 wt.% Bi. Average grain size of forged Sn-1 wt.% Bi is 100 μm while average grain size of non-forged Sn-1 wt.% Bi is 500 μm . Therefore, they will be named as small grain size (SG) sample and large grain size (LG) sample. However, SG Sn-1 wt.% Bi seem to have smaller standard variation which could be imply that it is more homogenized than LG Sn-1 wt.% Bi. Inner diameter (ID) has largest grain size in both forged and non-forged plate while middle diameter (MD) has smallest grain size. While A, B and C does not show any distinguished different in grain size.

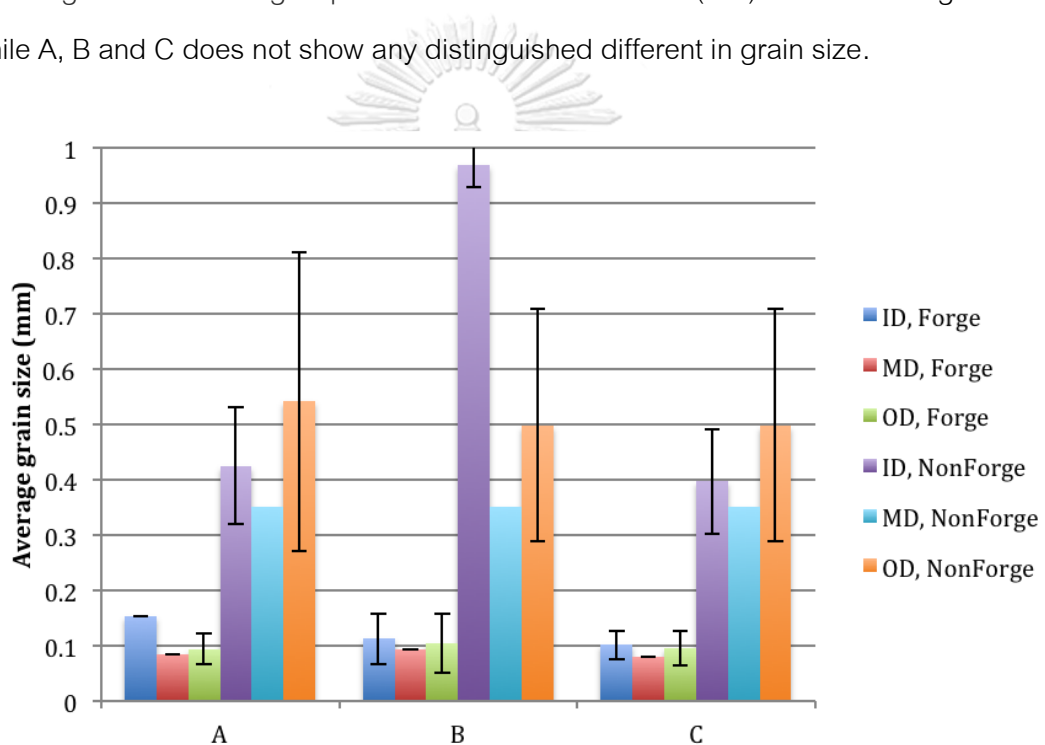


Figure 4.2: Average grain size in different direction and different area on the plate

Some of the photographs from optical microscope are shown in figure 4.3 and 4.4. They are clearly illustrated that LG Sn-1 wt.% Bi has larger grain size than SG Sn-1 wt.% Bi. Figure 4.3 shows photographs of LG Sn-1 wt.% Bi. They displayed some interesting features such as stripes inside the grain, different contrast inside the same grain and grain growth. These features could lead to explanation of recovery and recrystallization stage.

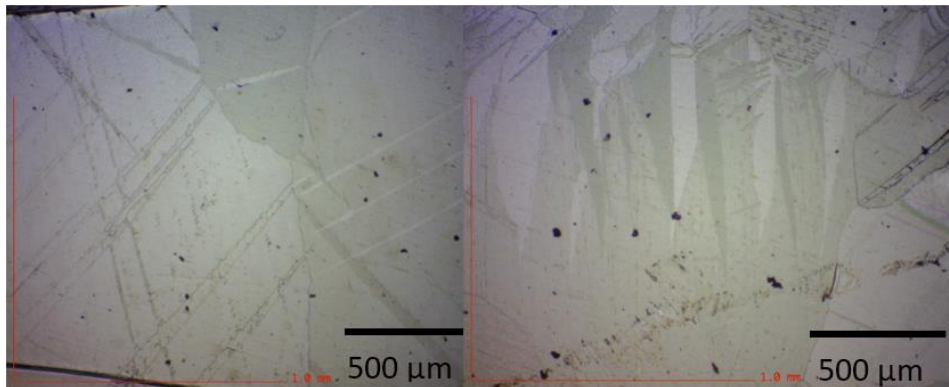


Figure 4.3: LG Sn-1 wt.% Bi plate under optical microscope

Figure 4.4 shows photographs of SG Sn-1%Bi. They displayed similar interesting features to LG Sn-1 wt.% Bi plate as shown in red circle. As mention above that these could lead to understanding the recovery and recrystallization process, further investigation is needed. Bismuth (Bi) could play an important role in these features as well as recovery and recrystallization process.

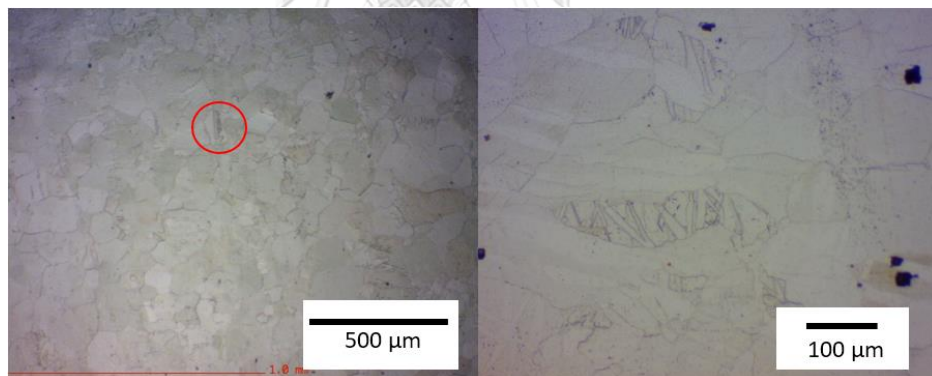


Figure 4.4: SG Sn-1 wt.% Bi plate under optical microscope

Field emission scanning electron microscope (FE-SEM) and energy dispersive X-ray spectroscopy (EDS) were used to investigate composition of those small interested features. Figure 4.5 shows SEM image of SG Sn-1 wt.% Bi plate in back scatter electron mode (BSE). It illustrates similar feature to LG Sn-1 wt.% Bi plate however, this is a much smaller scale. Mapping area scan of SG Sn-1 wt.% Bi plate is shown in figure 4.6. This mapping area scanned for Sn and Bi which are shown in yellow

and blue dots, respectively. These mapping areas show that Bi is evenly spread all over the alloy.

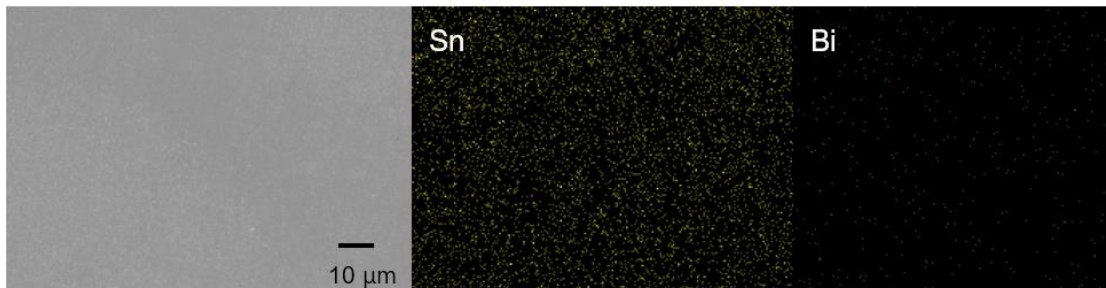


Figure 4.5: EDS mapping area scan of SG Sn-1 wt.% Bi

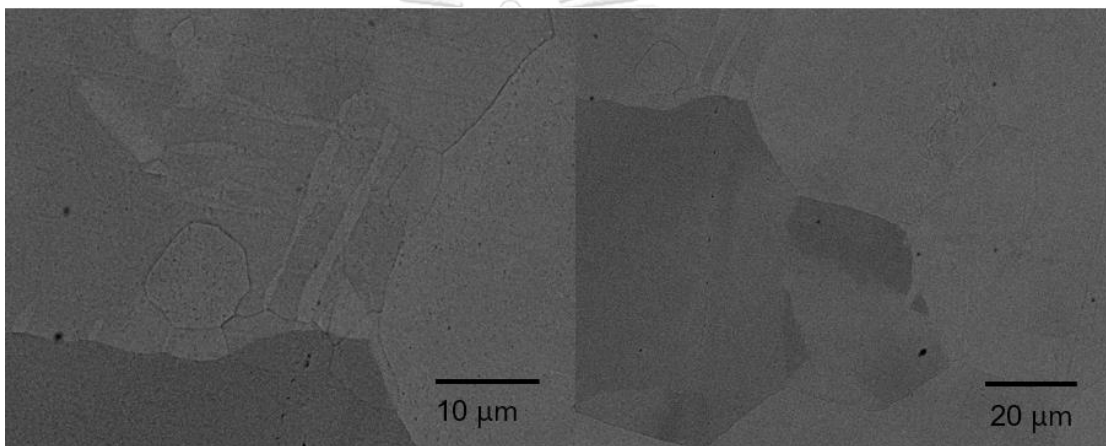


Figure 4.6: Image of SG Sn-1 wt.% Bi plate under FE-SEM in BSE mode

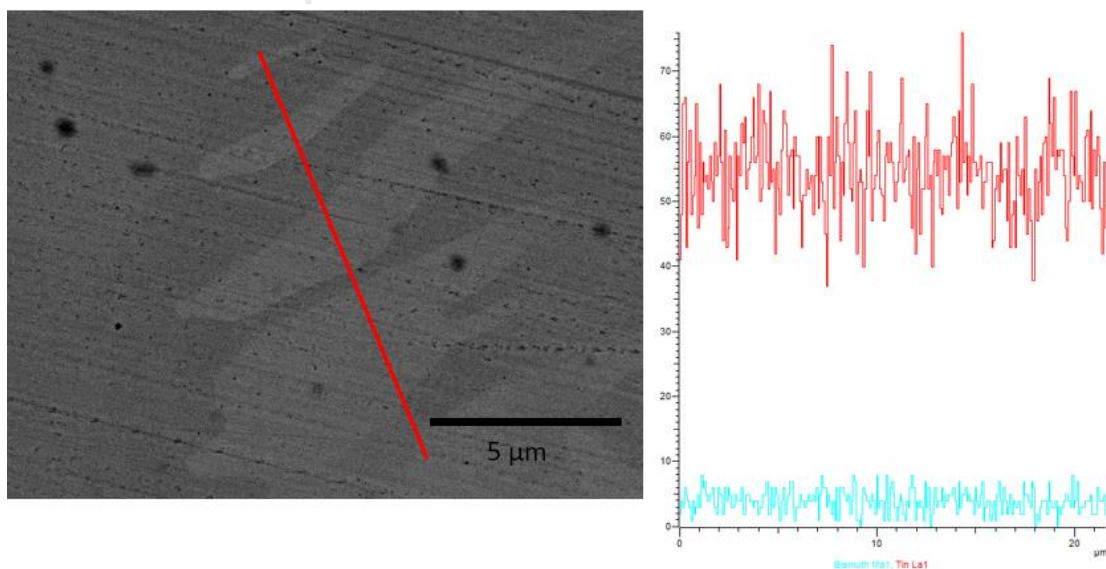


Figure 4.7: EDS line scan of SG Sn-1%Bi

Furthermore, as shown in figure 4.7 that there is a stripe feature in the grain. Line scan across these features was conducted to obtain location of Bi, shown in figure 4.7a, red line. In figure 4.7b, the chemical composition along the red line was shown. It can be concluded that Bi content is not the cause for this stripe feature.

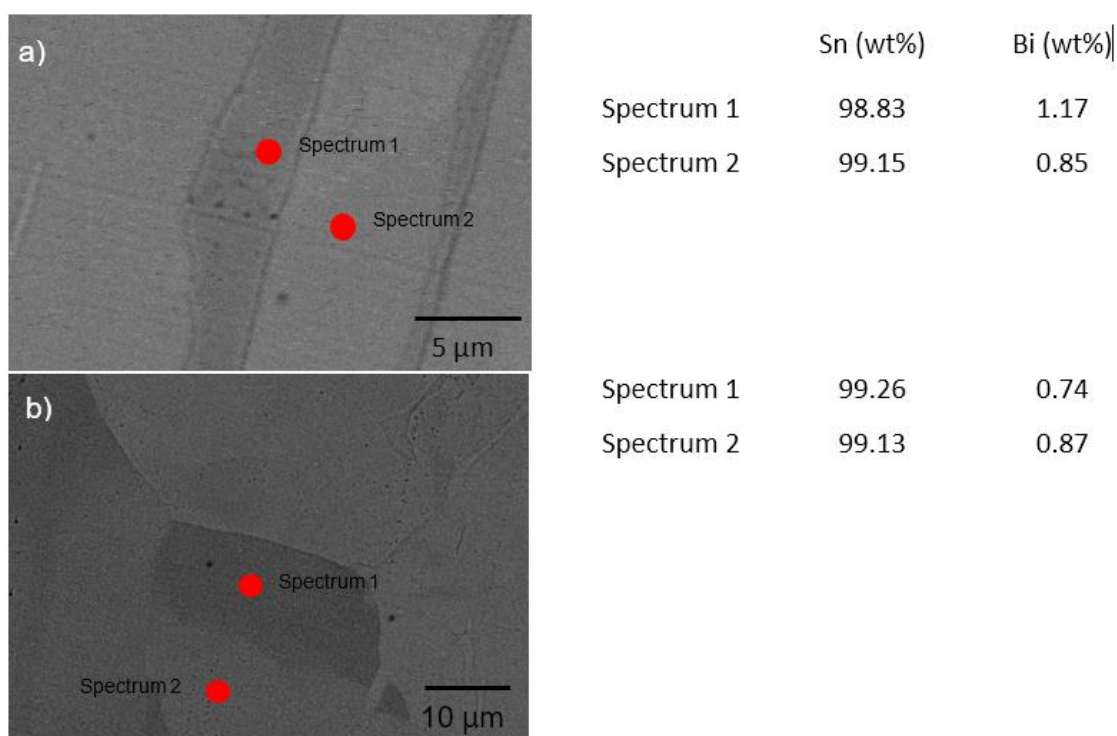


Figure 4.8: EDS point scan of SG Sn-1 wt.% Bi

EDS point scan was conducted to verify different in chemical composition in different area of the grain, shown in figure 4.8. Figure 4.8a shows point scan on stripe feature as it has two different contrast. In darker area, spectrum 1 shows Bi content as 1.17 wt.%. In lighter area has lower Bi content, 0.85%. Hence, there's a small different between stripe feature and background area. From figure 4.6, the contrast is gradually reduced along the grain. As EDS line scan could not give much information about variation of Bi content, EDS point scan was conducted instead and shown in figure 4.8b. Two points were selected as the dark area and the light area of the grain, which are spectrum 1 and spectrum 2 respectively. Bi content in spectrum 1 area is 0.74 wt.% while Bi content in spectrum 2 area is 0.87 wt.%. Even though there's a different in Bi

content between these 2 spots, the difference is too small to conclude that there's a gradient in composition along the grain.

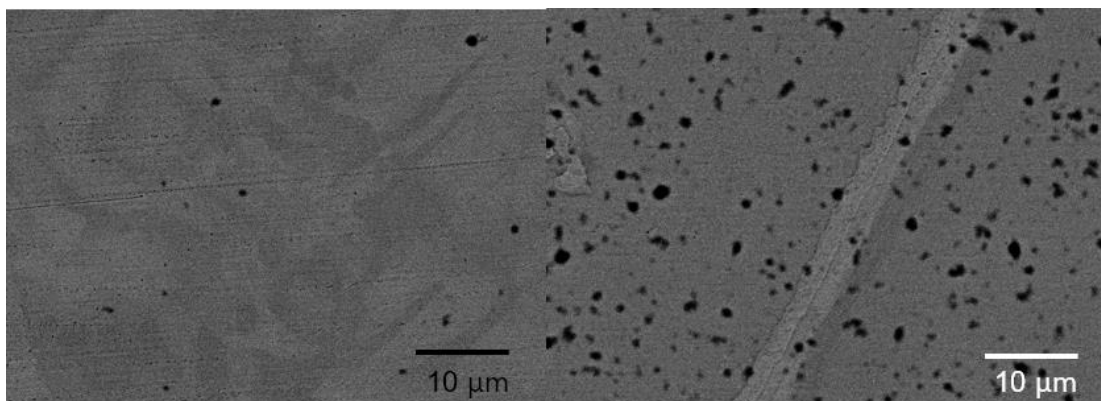
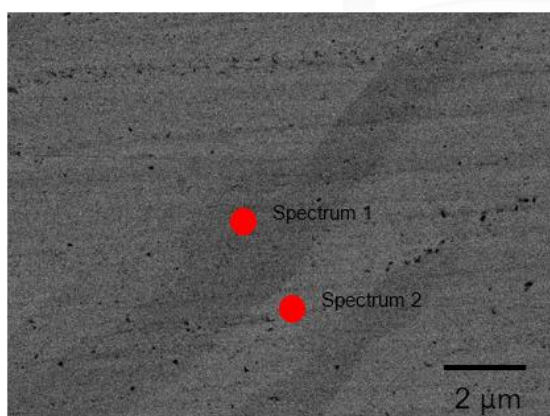


Figure 4.9: Image of LG Sn-1 wt.% Bi plate under FE-SEM in BSE mode

Likewise, LG Sn-1 wt.% Bi plate was also observed under FE-SEM and EDS study in order to locate Bi in the alloy. Since grain size of LG Sn-1 wt.% Bi plate is large compare to SG Sn-1 wt.% Bi, whole grain cannot be observed under the SEM. In the same way, stripe feature and other feature are larger than the SEM beam, therefore, only partial part of the grain can be observed at a time. Figure 4.9 shows image of LG Sn-1 wt.% Bi plate in BSE mode.



	Sn (wt%)	Bi (wt%)
Spectrum 1	98.75	1.25
Spectrum 2	99.48	0.52

Figure 4.10: EDS point scan of LG Sn-1 wt.% Bi

Figure 4.10 shows EDS point scan of LG Sn-1 wt.% Bi plate. There were two points scans namely spectrum 1 which is on stripe feature and spectrum 2 which is in

the background grain. Similar to SG Sn-1 wt.% Bi, Bi content in the stripe area (darker zone) is greater than lighter zone which is 1.25 wt.% and 0.52 wt.%, respectively.

From figure 4.8 and 4.10, it can be concluded that there's a different composition in stripe feature as Bi is more concentrated inside the darker stripe band. Usually, precipitated Bi is accumulated around grain boundary. However, from the line scan across grain boundary, there's no variation of Bi along the line as there is only 1% Bi. Nevertheless, it cannot be concluded that there's no precipitation around grain boundary.

4.1.2 Anisotropic property of lapping plate

Preferable direction of plate was studied using XRD in both SG Sn-1 wt.% Bi and LG Sn-1 wt.% Bi plate. As shown in figure 4.11a, A, B and C side show peak in different height for SG Sn-1 wt.% Bi and LG Sn-1 wt.% Bi sample. These peaks are then compared with the referenced powdered Sn, which has random orientations. Sn in (101) direction is the major direction of these sample. SG Sn-1 wt.% Bi plate show more homogenization than LG Sn-1 wt.% Bi plate as peak of A, B and C are similar except for the peak of Sn (112). When compare A side of SG Sn-1 wt.% Bi and LG Sn-1 wt.% Bi sample, figure 4.11 illustrates that nearly all the peaks are the same except that direction (112) is greater in non-forged plate. Comparison between different side of LG Sn-1 wt.% Bi plate shows that there is a different amount in (112) and (400) direction of Sn. It is commonly known that tin is anisotropic, which is coincide with this XRD result. Moreover, this XRD patterns also shows trace of crystallization during casting of the plate as shown here that (200) plane was relatively low compare with the powdered Sn pattern.

The XRD pattern in figure 4.11a can be used to determine crystal system and size of crystal structure. It is believed that this plate is tin-white with tetragonal structure. The dimension of the tetragonal in x and y direction are 5.819 Angstroms and 3.17 Angstroms in z direction.

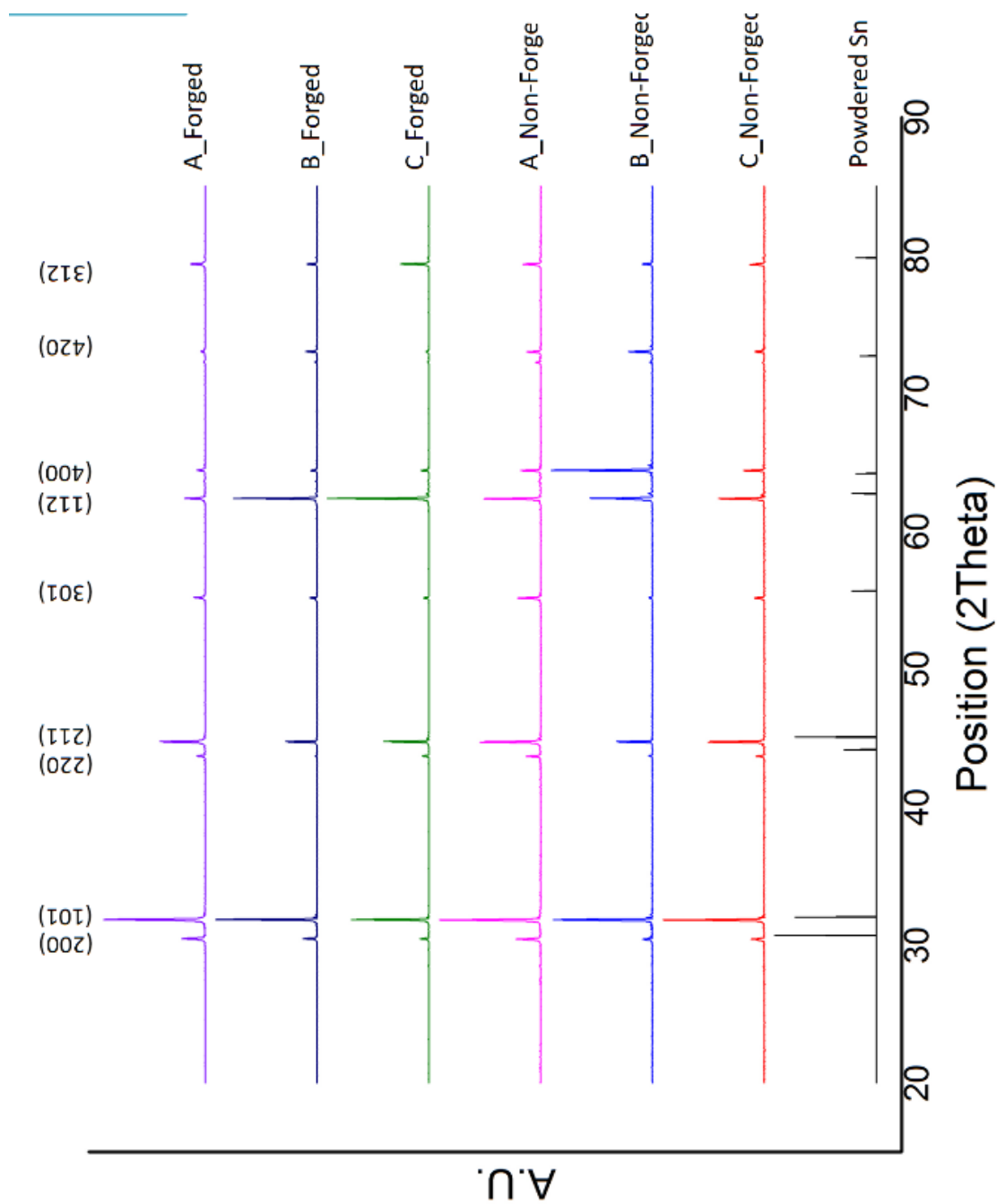


Figure 4.11: XRD plot in arbitrary unit (A.U.)

4.2 Mechanical property of lapping plate

4.2.1 Micro-Vicker Hardness measurement

The hardness values were determined by Microvickers hardness testing machine with diamond indenter. The Microvicker hardness test is divided into 2 parts. The first part is the effect of varying hold time on hardness of Sn-1wt%Bi. Hardness measurements were performed at hold time ranging from 10 seconds to 60 seconds and at constant applied load of 50 kgf. For second part, hardness measurements were performed at a load of 1, 2, 3, 5, 10, 50 and 100 kgf and at constant hold time of 20 seconds. Well-defined eight hardness measurements were done for each condition. Hardness values were then average, and the errors were calculated by standard deviation.

The specimens were wire-cut electrical discharge machining (EDM) from surface of the Sn-1wt%Bi lapping plate. The surface damage was removed mechanically by grinding down to 2000 grit sand paper and mechanically polished using 0.3 μm alumina suspension to achieve mirror-like surface.

4.2.1.1 Effect of varying hold time

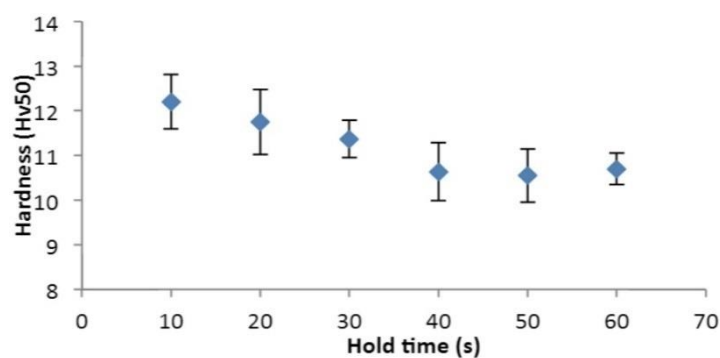


Figure 4.12: Hardness value of Sn alloy with varying holding period (s)

The hardness values vary around 10.6 to 12.2 Hv_{50} as shown in figure 4.12. It was found that as the hardness decreased with increasing hold time. This is due to

creep behavior of Sn alloy. When constant load is applied to the sample and hold for long period, the depth will be increased. This leads to an increase in diagonal length of impression (d^2) which reduce the hardness value.

4.2.1.2 Effect of varying applied load

Figure 4.13 shows the variation of Hardness, H_v as a function of applied test loads ranging from 1 to 100 kgf. Hardness decreased with increasing applied load and reached saturation at about 8 kgf. This phenomenon is called indentation size effect (ISE). The main reason is associated with error in measuring the diagonal length from optical microscope at small loads because the sizes of indented marks are very small. ISE might also result from strain-hardening or residual stress created during sample preparation (grinding and polishing) or occurrence of thin oxide films (the properties of thin oxide film are different to properties of bulk). Eventually, the hardness values become stable and precise at load above 5 kgf because using higher load created larger impression so indentation diagonal is easy to measure (less error) and indenter penetrated deeply into the sample (Measure hardness of the bulk instead of thin oxide film). Hence, the hardness found was more precise and accurate at high load. The applied load was used up to only 100 kgf because the load higher than 100 kgf cause too large indents area and won't be able to measure the d^2 from optical microscope.

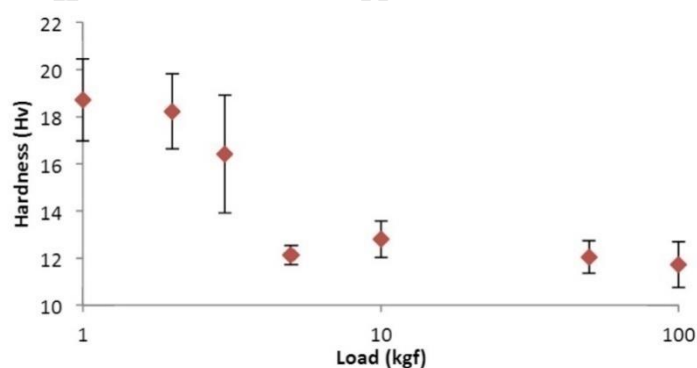


Figure 4.13: Hardness value of Sn alloy with varying load (kgf)

4.2.1.3 Effect of different composition of Sn

There were three compositions which are Sn-1 wt% Bi, Sn-58.69 wt% Bi and Sn-2.5 wt% Sb. Nomenclature used is following WD method namely, Sn-1wt%Bi is 725 plate, Sn-58.69 wt% Bi is 510 plate and Sn-2.5 wt% Sb is MMX plate. Samples were prepared by grinding process with 400, 600, 800, 1200, 2000 grid number of SiC paper then followed by polishing with alumina powder. During indentation, it can be divided into three steps namely loading step, holding step and unloading step. In this experiment, speed during loading step and unloading step was kept constant.

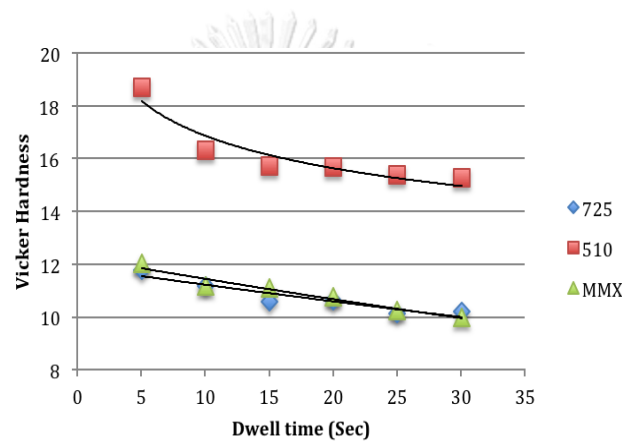


Figure 4.14: Varying hold time in Micro Vicker Hardness test at 100 kgf

Samples were subjected to different holding time (dwell time) and loading force. Each condition was repeated 5 times with at least four times of the indentation size separation. While the holding time was varied from 5 to 30 seconds, loading force was kept constant at 100 kgf. Result shown in figure 4.15. It can be seen that Sn-58.69 wt.% Bi plate has greatest hardness among three types of samples. While the Sn-1 wt.% Bi and Sn-2.5 wt.% Sb plate had shown similar Vicker hardness value of 11. All three plates are sensitive to holding time as hardness decreases as holding time increases.

Figure 4.15 shows the result from varying loading force in Micro Vicker Hardness test. While the loading force was varied from 5 to 200 kgf, holding time was kept constant at 15 seconds. Sn-58.69 wt% Bi plate has greatest hardness and its hardness increases with increasing loading force. On the other hand, Sn-2.5 wt% Sb plate

decreases with increasing loading force. While Sn-1 wt% Bi plate does not show any sensitivity on loading force.

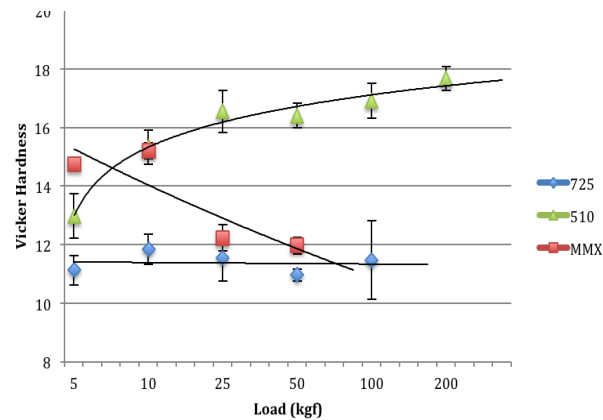


Figure 4.15: Varying loading force in Micro Vicker Hardness test

In both experiment, Sn-58.69 wt% Bi plate has greatest hardness which is approximately 16 -18 in Vicker hardness scale. This is due to its microstructure. Composition of Sn-58.69 wt% Bi plate is 47.45 wt% Sn and 52.55 wt% Bi. This is a eutectic composition of this alloy. Therefore, this tree-like pattern in the microstructure will provide strength and prevent dislocation movement in the grain. The reason that hardness decreases with increasing holding time and loading force is because this alloy has fast recovery process. It has recovery itself faster than it has become hardening. Recovery reduces this dislocation density, it normally results in a reduction in material strength and a simultaneous increase in ductility.

4.2.2 Nanoindentation

In this experiment, Sn-1wt%Bi plate was used to study in order to understand its mechanical behavior especially its dynamic effects. Nanoindentation was used to obtain data for this study. The constant load (CL) and constant strain rate (CSR) are popularly mode used to study in nanoindentation test. These two modes have their own usefulness and can be distinguished as followed; CL is able to scrutinize the mechanism during indentation whereas CSR is able to examine the steady-state creep incurring.

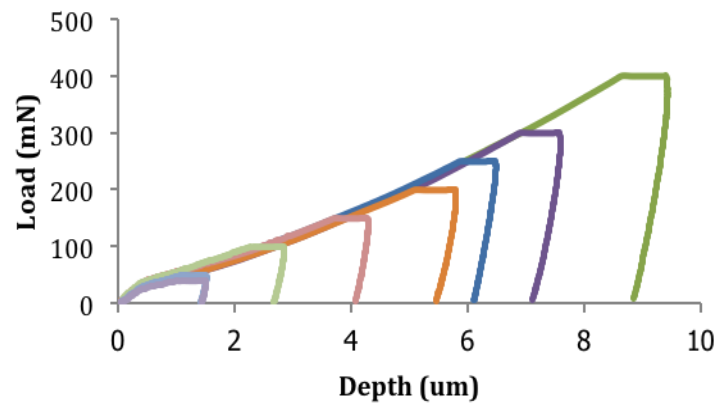


Figure 4.16: Load and displacement curve at different maximum load ranging from 10 to 400mN. Hold time and loading rate were set as 20s and 4.5 mN/s respectively

For in-depth study of recovery and hardening effect, Nanoindentation was used. The experiments were performed on Nano-Mechanical Instrument (UMIS II, CRISO, Australia) with Berkovich indenter at Chulalongkorn University, Faculty of Dentistry. Sample was prepared similar to Micro Vicker hardness. The effect of varying maximum load on hardness and elastic modulus of Sn-1wt%Bi plate were examined. The holding time used were 20 seconds and the loading rate used was 4.5 mN/s. The maximum loads were varied from 10mN to 400mN as shown in figure 4.16. About five indentations were performed for each conditions and IBIS Nanoindentation system were used for calculating hardness and elastic modulus which is based on Oliver and Pharr's model. Hardness, elastic modulus, load against depth plot and load against time plot can be extracted from the testing machine. Five indentations were performed for each condition. Hardness and elastic modulus were averaged among those indentations.

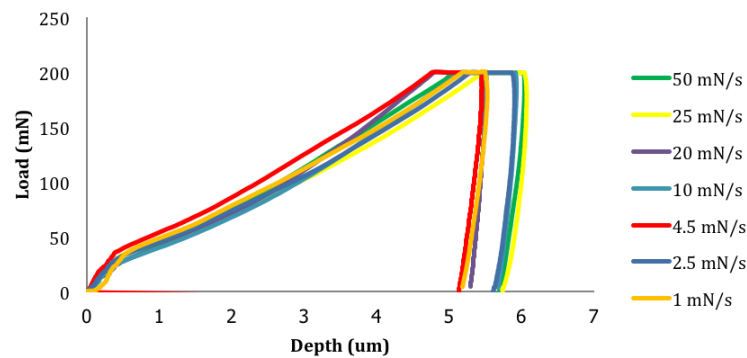


Figure 4.17: Load-displacement curve at different loading rate ranging from 1 to 50mN/s. Hold time and loading rate were set as 20s and 4.5 mN/s respectively

Hardness and elastic modulus can be calculated from the plot of load against displacement as shown in figure 4.16. The slope of loading section in all the test are approximately equal, so this suggest that the loading rate similar for all the test. Moreover, the slope is very steep at depth below 0.5 μm and then the slope decreases after passing 0.5 (This occur for all test). Possible reason might due to occurrence of thin oxide layer, residual stress at the surface of the sample from sample preparation which indenter required more load to penetrate sample. Hence, the slope is steeper. Another possible reason might due to limitation of the machine. Moreover, the effect of varying loading rate on hardness and elastic modulus of Sn-1wt%Bi plate were performed. Holding time and maximum load were set to 20s and 200mN respectively. The loading rates were 1, 2.5, 4.5, 10, 25 and 50 mN/s. Result is shown in figure 4.17.

As mentioned earlier that hardness and elastic modulus was calculated from the unloading section of load against displacement curve. They are plotted in figure 4.18 and 4.19 which illustrate that hardness and elastic modulus decrease with increasing applied load. This is due to the indentation size effect (ISE). Eventually, the elastic modulus and hardness become stable after 200 mN and have value of 0.22 GPa and 33.56 GPa, respectively. This is in good agreement with other experiment [11]. Moreover, maximum applied load variation experiment shows large error at small-applied loads. This is due to the large variation in the contact depth from load and displacement plot. It was also found that loading rate had no effect on hardness. The

hardness values were constantly around 0.25 GPa. The maximum load was set at 200 mN. However, the elastic modulus increases with increase loading rates and become stable at loading rate of more than 10mN/s.

Figure 4.19 showed that the calculated reduced elastic modulus remained constant at load larger than 100 mN. There was a small reduced in elastic modulus at a smaller strain rate for strain rate varying experiment which could due to the indenter tip roundness and the surface oxidation of the specimens. This situation is consistent with results reported in the literature [114]. However, in the load varying experiment, the elastic modulus increased as the applied load decreased. Ordinarily, the variation of elastic modulus obtained as a function of the indentation load shows that the elastic modulus increases with increasing indentation depth then reaches a saturation value at certain indentation depth. The transition in such curve and plateau of constant elastic modulus is corresponding to the intrinsic reduced elastic modulus of the materials.

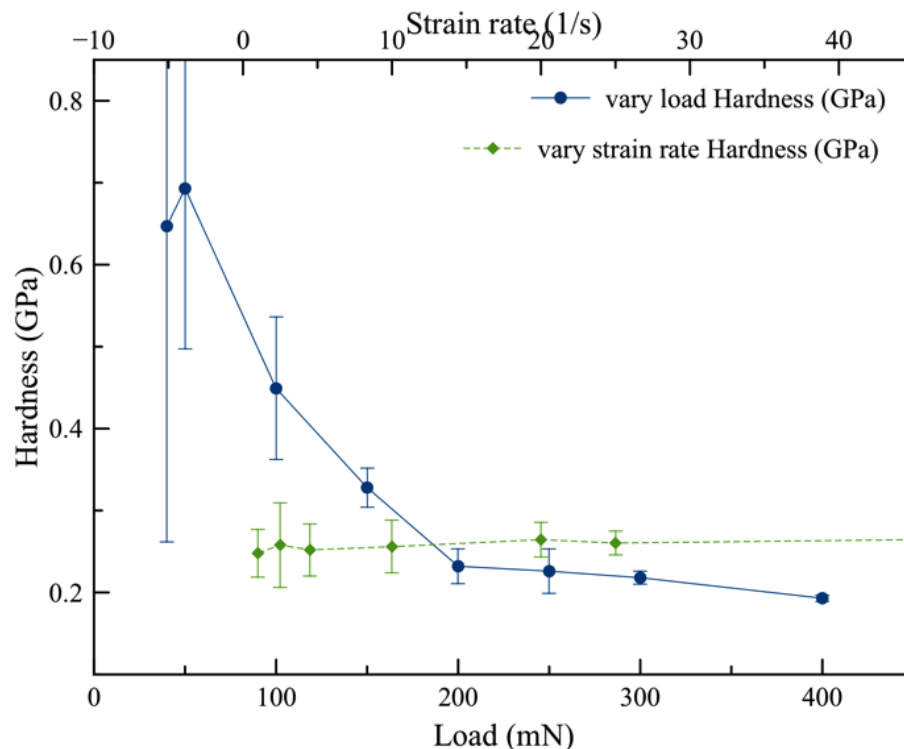


Figure 4.18: Calculated hardness from varying loading rate and strain rate

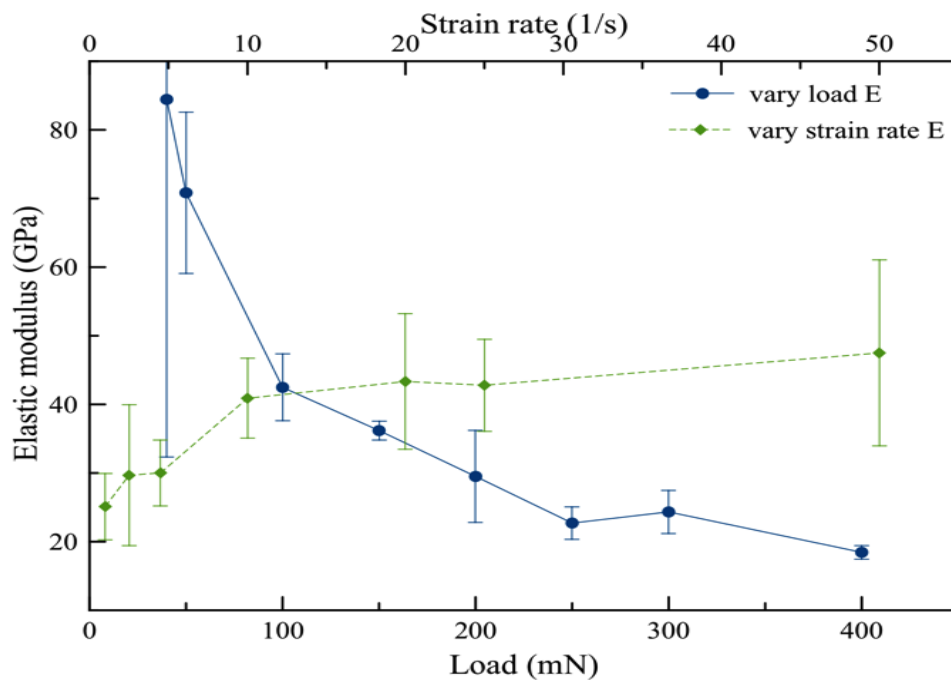


Figure 4.19: Calculated elastic modulus from varying loading rate and strain rate

To further investigate the anisotropy effect of mechanical property according to their direction of casting, nanoindentation was exploited. Hardness and Elastic modulus were explored. Besides direction of casting, various regions on the lapping plate were also considered namely inner diameter (ID), middle diameter (MD), and outer diameter (OD). Elastic modulus and hardness of SG and LG Sn-1 wt% Bi were compared. According to Chudoba and Richter [115], a hold period should be long enough during Nanoindentation test in order to prevent creep effect in hardness and elastic modulus calculations. In this test, the applied loading rate is 4.5 mN/s with 60 seconds of holding period at peak loads while varying peak loads from 10 to 400 mN. Each test was repeated three times with at least four times the size of indented apart to increase reliability of experimental results. In hardness and reduced elastic modulus calculation, Berkovich indenter tip was assumed perfect shape. Therefore, area function for the indenter is $A = 24.5h_c^2$ where h_c is the displacement when there is no elastic deformation that was calculated using equation 2.8.

It can be seen from figure 4.20 that the average hardness values of both SG Sn-1 wt.% Bi and LG Sn-1 wt.% Bi decreased with increasing maximum indentation applied load. They were later reached plateau state after 100 mN with calculated average hardness of 0.2 GPa regardless of pre-forging, direction of casting and region on the plate. This behavior is well-known as indentation size effect (ISE). The specimens show indentation size effect at applied load lower than 100 mN. Moreover, the error bar is larger at applied load lower than 100 mN which could imply that there is less consistent in data. From figure 4.20, it could be presumed that grain size does not affect the hardness. It is possible that the size of indenter is far too small compare to grain size, hence average hardness is similar between specimens with grain size of 0.1 and 0.5 mm. Grain boundary sliding and grain refinement are not the major strengthening mechanism in this case.

Data were closely evaluated and compared between SG Sn-1 wt.% Bi and LG Sn-1 wt.% Bi plate. From figure 4.21, there is no distinct variation between directions of casting the lapping plate even though microstructure of non-forged plate showed that there is a difference in shape of grain between cross-section facet (C) and longitudinal facet (B).

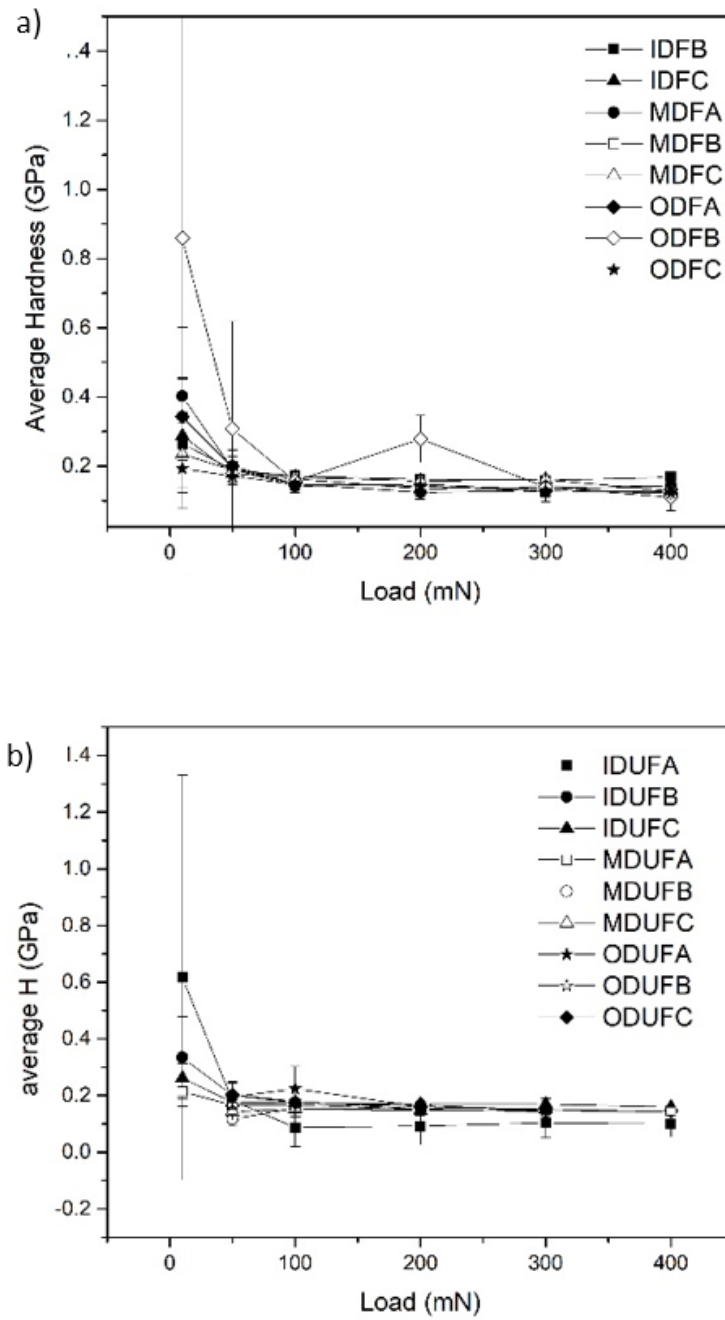


Figure 4.20: Average hardness of a) SG Sn-1wt%Bi plate and b) LG Sn-1wt%Bi plate of different casting direction and region on the lapping plate

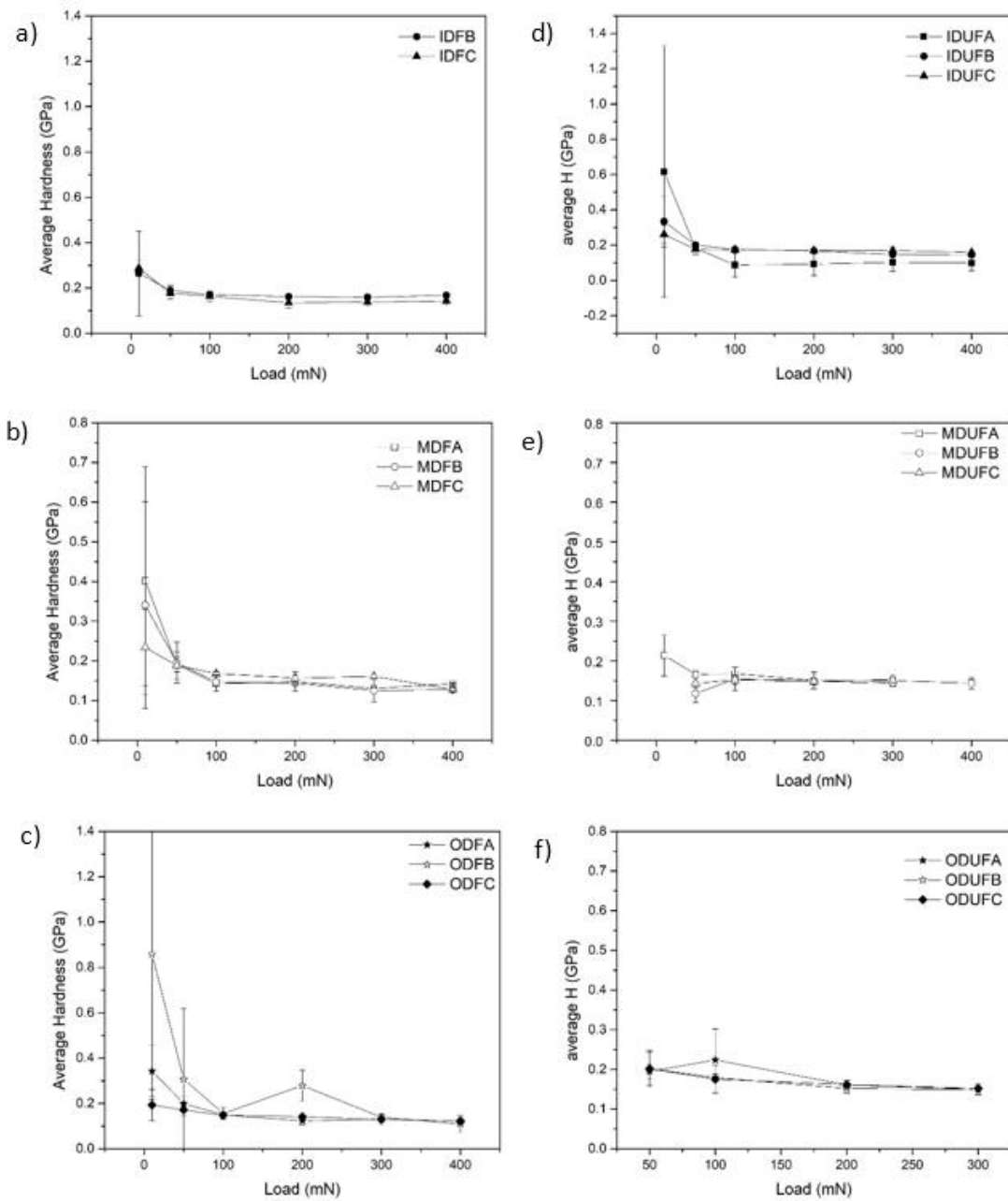


Figure 4.21: Average hardness of Sn-1 wt% Bi between small grain size sample (left-handed column) and large grain size sample (right-handed column) at inner diameter a) and d), middle diameter b) and e), and outer diameter c) and f)

Figure 4.22 showed that averaged reduced elastic modulus is approximately 40 GPa for both SG Sn-1 wt% Bi and LG Sn-1 wt% Bi plate. In spite of this, averaged reduced elastic modulus of SG Sn-1 wt% Bi plate along longitudinal facet (B) and cross-section facet (C) is lower than the other region and casting direction to 10 GPa. There is also an evidence of indentation size effect at applied load lower than 100 mN, similar to average hardness.

Figure 4.23a), b) and c) display that average reduced elastic modulus is the lowest at inner diameter and the widest spread out of data at outer diameter in SG Sn-1 wt% Bi plate. On the other hand, the LG Sn-1 wt% Bi plate has broad average reduced elastic modulus in all regions as shown in figure 4.23d), e) and f).

In conclusion, as the average hardness does not show significant variations concerning grain size, direction of casting and regions on lapping plate, this could suggest that grain refinement is not the main strengthening mechanisms. However, it should be apprehended that the size of the indenter is much finer than the grain size of the lapping plate. Similarly, the reduced elastic modulus does not show considerable difference in the data at different as a result of grain size, direction of casting and regions on lapping plate. The reduced elastic modulus data of SG Sn-1 wt% Bi plate is more consistent between different casting directions which could lead to better uniformity of diamond impregnation on the forged lapping plate. Nonetheless, it is worth noting that reduced elastic modulus data is profoundly depending on initial slope of unloading section. It was found that the errors in indentation size measurements due to elastic recovery and indenter tip blunting are not the only source of ISE observed in the study [116].

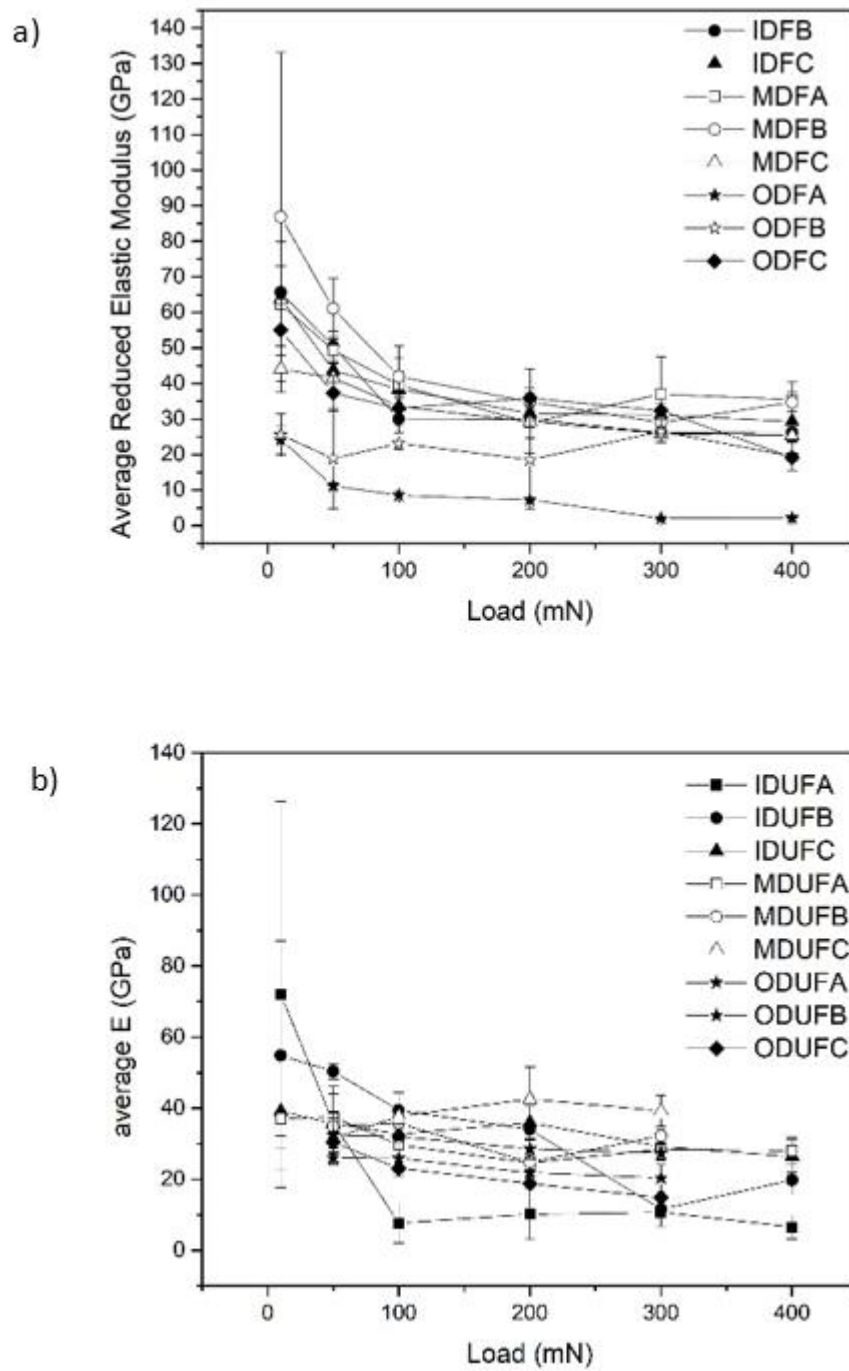


Figure 4.22: Average reduced young modulus of a) SG Sn-1wt%Bi plate and b) LG Sn-1wt%Bi plate of different casting direction and regions on the lapping plate

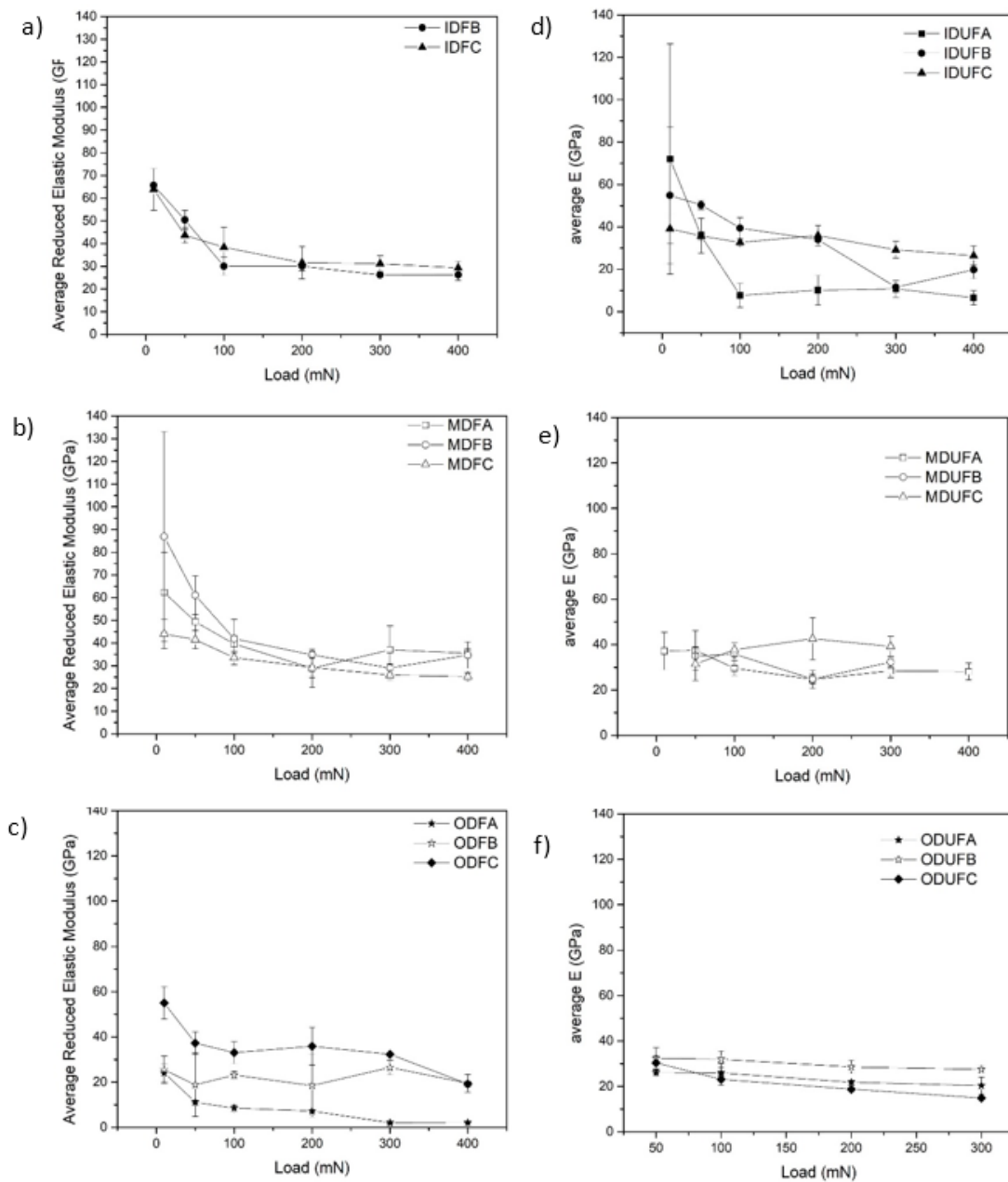


Figure 4.23: Average reduced elastic modulus of Sn-1 wt% Bi between small grain size sample (left-handed column) and large grain size sample (right-handed column) (right-handed column) at inner diameter a) and d), middle diameter b) and e), and outer diameter c) and f)

4.2.2.1 Indentation size effect (ISE)

The indentation size effect is a phenomenon where the hardness is larger at a smaller applied load. As shown earlier, the ISE was observed in the Sn-1%Bi alloy. This similar behavior was also observed in pure Sn [114] for different crystal direction of single crystal. There are many phenomenon that could cause ISE which are work hardening during indentation, magnitude of the loads to initiate plastic deformation, indentation elastic recovery, strain gradient associated with dislocations, tip rounding, temperature, and grain boundaries [117-119]. However, the main reason behind them is the reduction of the size of dislocation assemblies around indents. The ISE has been examined extensively on different kind of materials. At small loads, the indenter may penetrate only the region nearest to the surface. Therefore, the measured hardness and elastic modulus is of its oxide layer instead of the bulk material.

The most widely use empirical equation for describing the ISE is the Meyer's law. Meyer's law is an empirical equation between the size of hardness from indentation test and the load required to leave the indentation. It's described in the form of power law as:

$$P_{max} = Ch_c^n,$$

Where C and n are constants derived from curve fitting of the experiment data. P_{max} is peak indentation load. h_c is contact depth during indentation. Exponent n is Meyer index where it could be used to explain the effect of the deformation on the hardness of the material. The exponent usually lies between 2 and 2.5 where the first one is found for fully strain hardened materials and the latter is for fully annealed materials. The ISE is observed if n is less than 2.

In order to avoid the possible superposition of the ISE, a careful analysis of the surface preparation, surface cleanliness and testing conditions in each material is needed.

4.3 Conventional Creep

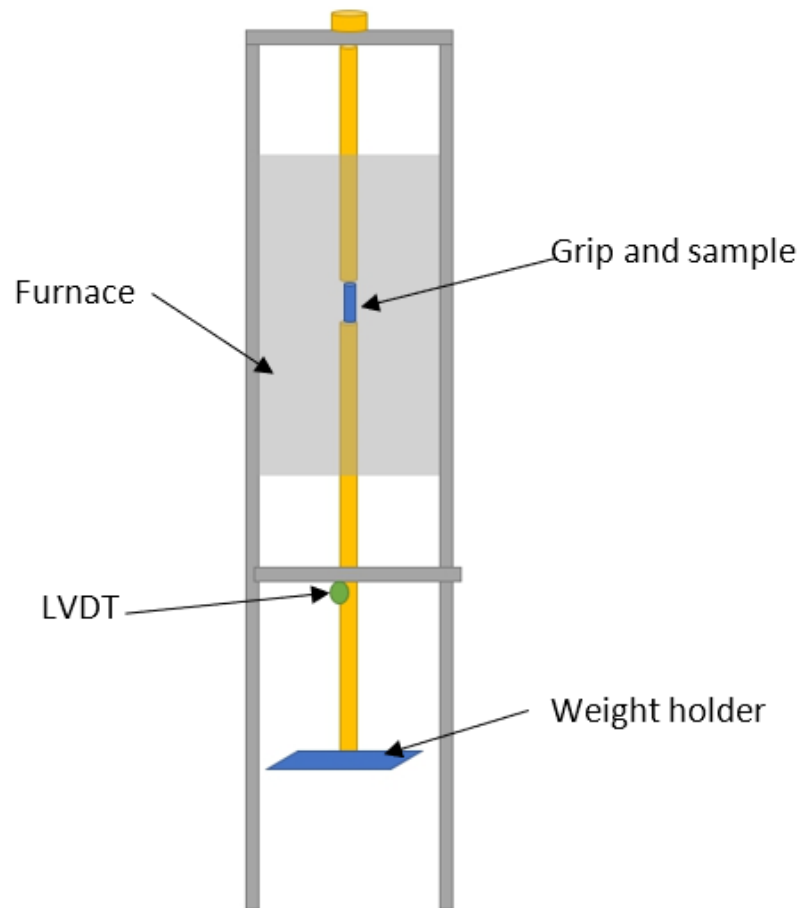


Figure 4.24: Creep frame

Creep is defined in material science as the tendency of a material to deform permanently under the influence of mechanical stresses lower than its yield strength. As creep is more severe in materials that are subjected to heat for long periods under given stress, comparable to the lapping process, tin alloy is used as a lapping plate which was subjected to stress from lapping and heat from cycling movement of lapping. This could help explain diamond behavior during lapping process. Creep frame is shown in figure 4.24. The conventional way of controlling the applied load is by applying direct weights. The strain was measured by linear variable differential transformer (LVDT) which were located below the furnace to ensure no effect from heat of the furnace. Thermocouple were tied with the sample at the gauge length.

4.3.1 Isothermal Creep

There are two types of the specimen to be test under creep frame. They are SG Sn-1%Bi and LG Sn-1%Bi. Sample were machined to the size according to ASTM E8, creep standard test as shown in table 4.1. Figure 4.25 shows machined specimens. Constant load creep tests were performed in air at three different temperatures which are 298, 353 and 393 K under stresses varying from 1 to 30 MPa. Temperature was measured using K-type thermocouple attached onto a specimen to ensure the exact temperature on the specimen. Some of the data points were collected as the applied stress was increased in steps after the secondary creep regime was reached or stepwise on a single specimen. The loading process was repeated until the specimen is fractured. After the samples had entered the secondary stage of creep, the creep rate was determined. The result is shown as deformation and time where the slope of this plot will be further investigated for creep mechanism.

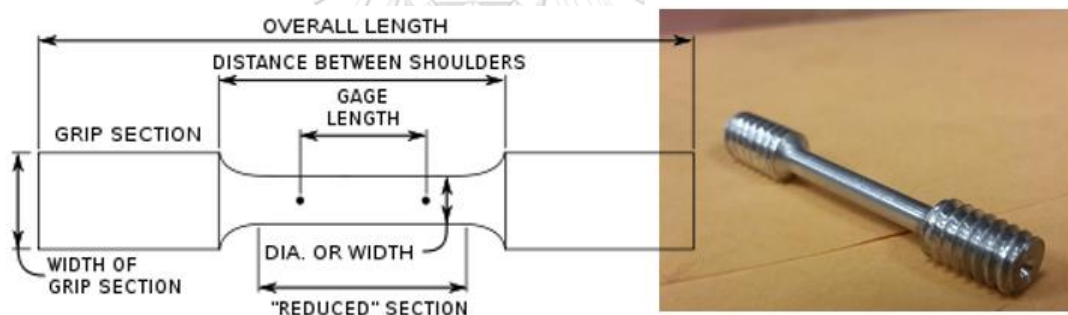


Figure 4.25: Creep specimen following ASTM E8 Standard

	DIMENSION (MM)
DIAMETER OF REDUCED SECTION	3
GAGE LENGTH	15
DISTANCE BETWEEN SHOULDER	18
THREADED END	0.25" - 20

Table 4.1: Dimension of creep specimen following ASTM E8 standard

SG Sn-1%Bi was chosen as a subject to study for its creep property and mechanism at 298, 353 and 393 K by heating the sample in the creep frame to the certain temperature under applied stress until the strain of specimen reaches the steady state. Slope of the strain and stress plot was shown in figure 4.26. It is obviously shown that there's a transition of creep mechanism for all the temperature. The transition of creep mechanism of this specimen is around 7-10 MPa. The observation of two regime namely high stress and low stress regime with transition range between 8-10 MPa was detected by other research [120, 121]. The transition shift to a lower stress as temperature increased. At higher applied stress, creep exponent is around 8 where creep exponent of lower applied stress is around 1 which could be concluded that at higher applied stress, the system is under power-law creep while at lower applied stress, the system is under diffusional creep.

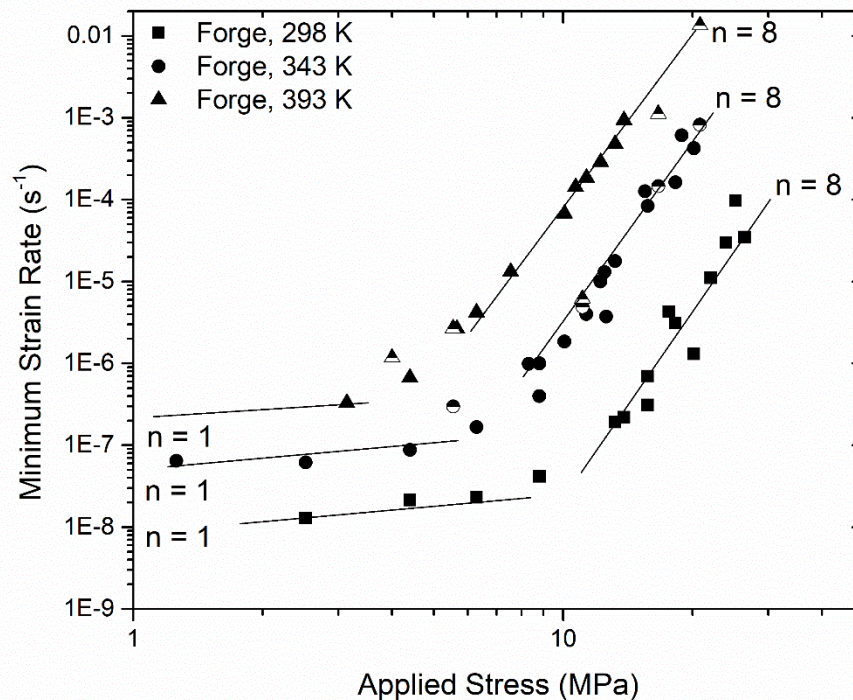


Figure 4.26: Creep behavior of forging Sn-1%Bi at 298, 343 and 393 K

The applied stresses were increased in a stepwise method on a single specimen as mentioned earlier. In order to confirm that the strain rate measured from this method is at its minimum, a single applied stress was employed until the specimen is fractured and shown as half-filled data point in figure 4.26. Minimum strain rate was estimated from differentiation of strain rate and time plot and shown indistinguishable of slope or stress exponent. This verified that strain rates acquired from stepwise-applied-stress experiment were in steady-state creep. This implied that the minimum strain rate and stress exponent between stepwise-applied-stress experiment and single-applied-stress experiment is comparable.

4.3.2 Thermal Cycling Creep

Internal stress was studied by forcing the specimen to expand and contract under applied heat. Specimen was cooling under ambient air. There were two rate of heating and cooling cycle which are 30 mins/cycle and 15 mins/cycle. Figure 4.27 shown the result of thermal cycling which is similar to the isothermal experiments as shown in figure 4.26. Transition range during thermal cycling is approximately at 7- 10 MPa. Mechanism of creep during thermal cycling is in the same as the isothermal experiment where higher applied stress has creep exponent of around 8 where creep exponent of lower applied stress is around 1 which could be concluded that at higher applied stress, the system is under power-law creep while at lower applied stress, the system is under diffusional creep. The rate of thermal cycling doesn't affect the mechanism and transition range of this specimen.

Figure 4.28 shows the superimposed thermal cycling experiment and isothermal experiment. It appeared that both experiments have similar creep mechanisms as well as transition range. It was illustrated that strain rate and stress curve of isothermal experiment is in the middle between isothermal 298 K and isothermal 353 K creep curve. However, the stress exponent of the higher stress region of thermal cycling is slightly higher which could imply that the creep resistance is lower. Therefore, it can be

concluded that at the thermal heating and cooling rate of cycling or cycling rate in this experiment does not have an internal stress effect due to the contraction and expanding of the metal.

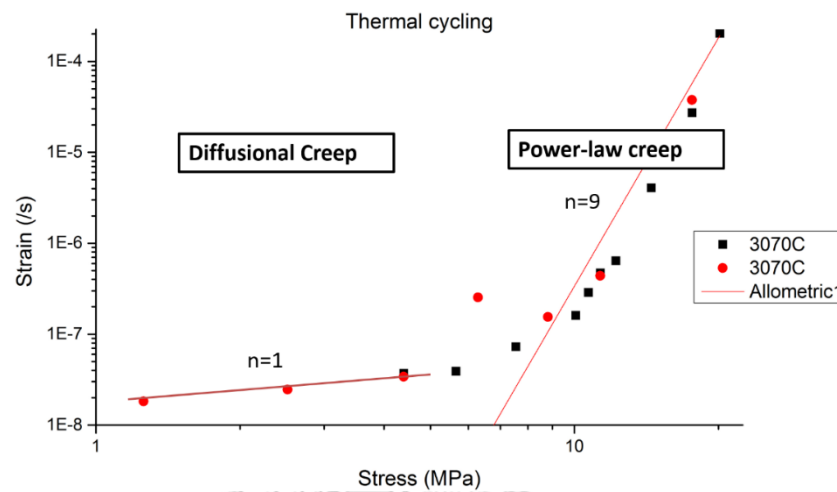


Figure 4.27: Creep behavior of thermal cycling between 298 and 353 K of forging Sn-1 wt% Bi

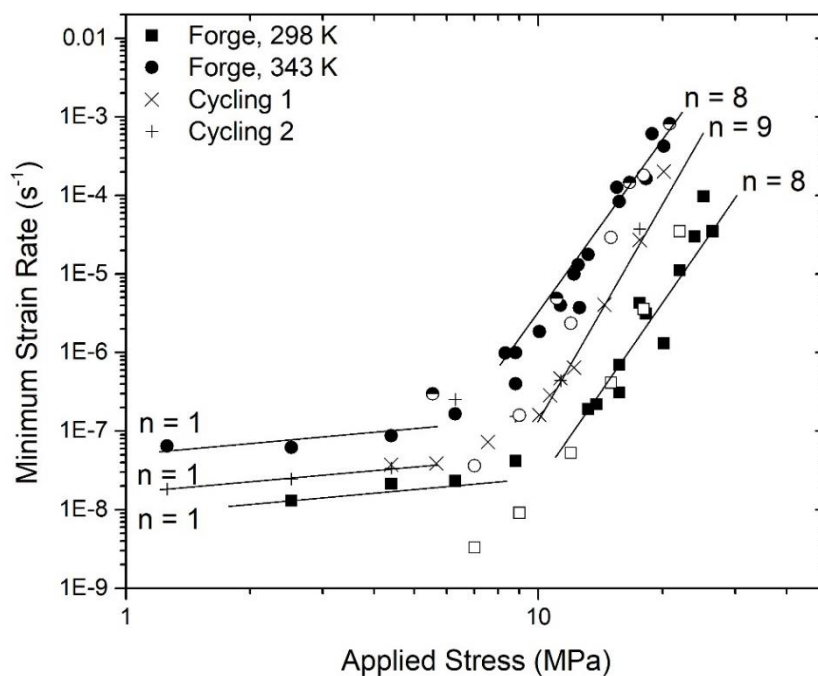


Figure 4.28: Superimposed of creep data from isothermal experiment and thermal cycling experiment

The logarithm of the creep rate was then plotted against the reciprocal of the absolute temperature in figure 4.29. The slope of this plot thus yielded the activation energy divided by the gas constant. Activation energy at higher stress ($n=8$) is roughly estimated as 9,000 cal/mol (37.4 kJ/mol) while the activation energy at lower stress ($n=1$) is roughly estimated as 4,000 cal/mol (16.82 kJ/mol). This is coincided with the study back in 1958 [122]. However, the material used in the study was 99.99% zone-refined tin. This indicates that 1 wt% Bi does not have significant effect on the activation energy of creep.

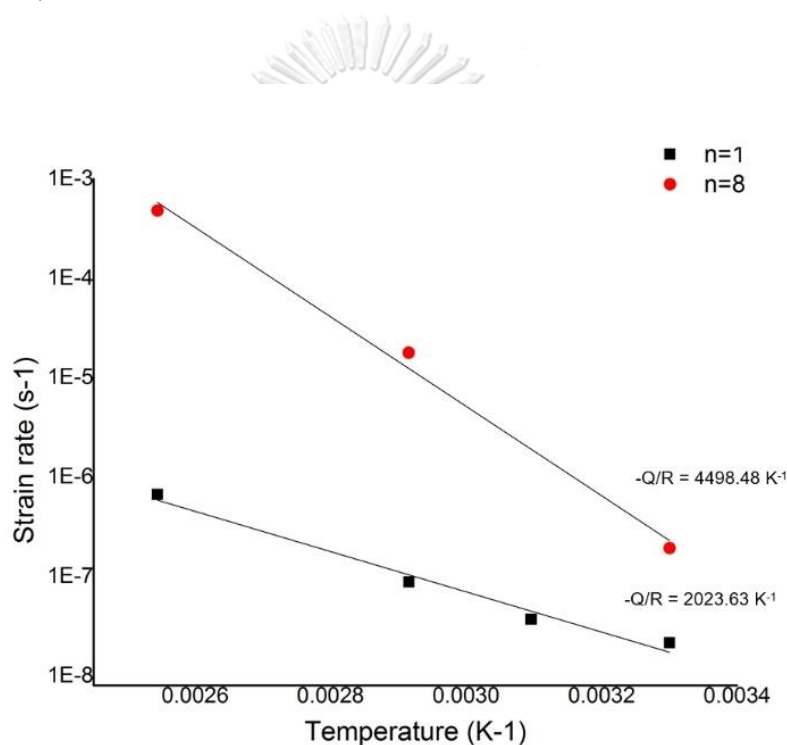


Figure 4.29: Creep rate and reciprocal of the absolute temperature with activation energy from low stress and high stress region

Lastly, minimum strain rate of SG Sn-1%Bi specimen and LG Sn-1%Bi specimen were compared on the same range of applied stress in figure 4.30. Slope of minimum strain rate against applied stress plot for both 353 and 393 K in high stress region show that grain size does not affect creep behavior. The transition region does not change by grain size of the specimen. This is contradicting to general understanding. Usually,

creep rate is decreased by increasing grain size [123-125]. The calculated activation energy shows in figure 4.31. In high stress region ($n=8$), there is no different between SG Sn-1%Bi specimen and LG Sn-1%Bi specimen. The calculated activation energy is approximately 37.4 kJ/mol. On the other hand, the calculated activation energy in low stress region ($n=1$) shows deviation. The smaller grain size has lower activation energy by half, compares to the activation energy of larger grain size. This suggests that the LG Sn-1%Bi specimen has lower creep resistance since the relative strain rate of the two curves. While the stress exponents are not affected by grain size changes in the range of examined. This is coincide with other research [28].

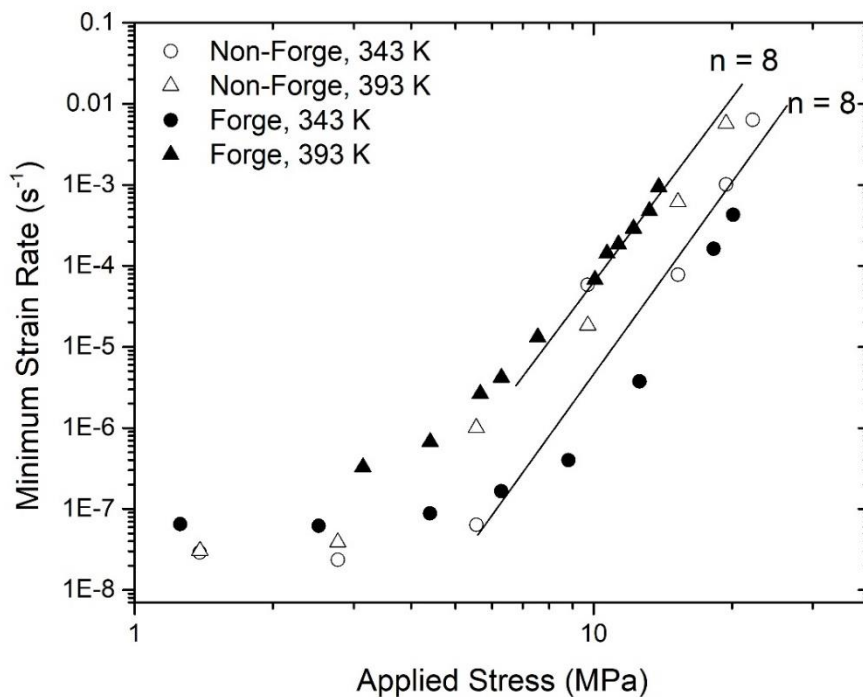


Figure 4.30: Minimum strain rate against applied stress of LG Sn-1%Bi specimen at 343 and 393 K

The calculated activation energy can be used to identify the mechanisms involved during creep deformation. It can be concluded that the mechanism corresponding to the creep behavior of high stress region is cross slipping dislocation or dislocation pipe diffusion [121] while the mechanism for the creep behavior of at low stress region is glide dislocations [126].

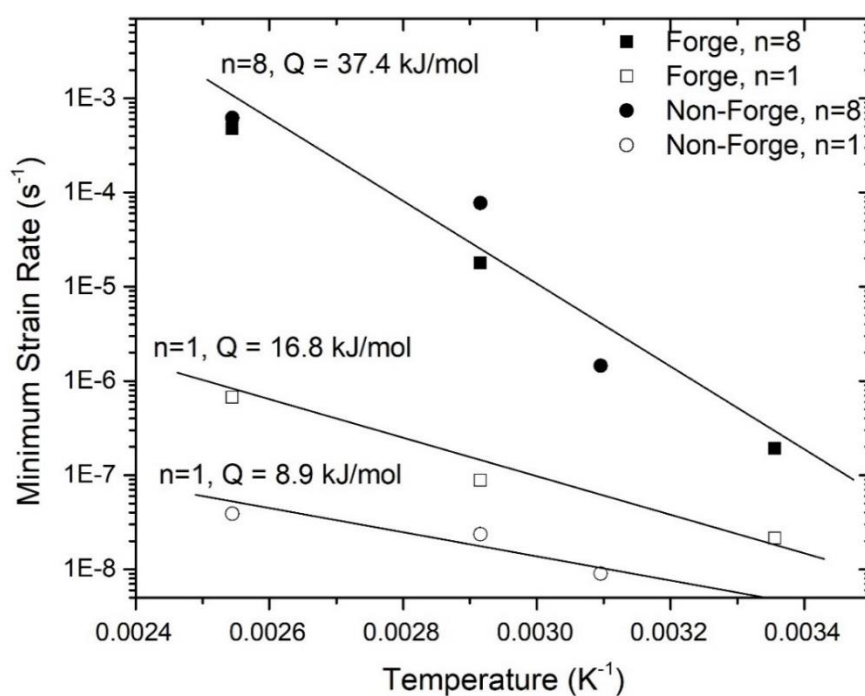


Figure 4.31: Plot of minimum strain rate with a function of temperature

4.4 Nanoindentation creep

4.4.1 Methodology

There are two sizes of grain diameter namely, 100 and 500 μm . Surface of both samples were mechanically grinded and polished with SiC 400, 1000 and 2000 grit followed by 1 μm and 50 nm alumina suspension. 2% HCl in Methanol was used as etchant.

The depth sensing creep experiments were performed on Nanoindentation Hysitron TI950 model. Three different maximum loads, constant loading and unloading rates, hold 300 s with 60 s for thermal drift corrections. In all nanoindentation tests a total of five indents are averaged to determine the mean hardness and elastic modulus values for statistical purposes. All nanoindentation tests have been performed with the standard three-sided pyramidal Berkovich probe.

In a nanoindentation creep experiment, the initial loading is pushed the indenter tip into the surface until specified maximum load is reached, then the load is held constant for 300 seconds. Finally, the indenter tip is retracted from the material. The loading and unloading rates are 200 $\mu\text{N/s}$. The creep tests were performed at several temperatures namely, 298, 353 and 393 K. Five repetitive tests were performed at each temperature to ensure repeatability of the data. Data with strain burst were excluded.

4.4.2 Results and Discussion

The hardness and Elastic modulus were determined from the load displacement curves based on Oliver-Pharr method [127]. Values of hardness and elastic modulus shows sign of indentation size effect below 1000 μN and 500 μN , respectively as shown in figure 4.32. SG Sn-1%Bi sample seems to be harder than the LG Sn-1%Bi. This could be the result of grain size effect. Elastic modulus does not affect by the apply loads. However, the range of standard deviation is quite large. This is the result from the bowing of unloading section where it could be reduced by increase a holding section. In order to avoid indentation size effect on creep, 1000 μN maximum load was chosen to hold for 360 s.

During the dwell period at maximum applied load, the indenter continues to penetrate into the specimen with time. Dwell period was shown in figure 4.33 where time and displacement were adjusted to zeroes for easier of calculations. Figure 4.33 shows changes in indentation depth with time. This is similar to creep curve retrieves from conventional uniaxial creep test. At the beginning of the curves were corresponded to the transient creep, then creep rates were decreasing to a steady state value. The slope

of the curve increases with temperature. The creep rate and displacement increase with temperature as expected.

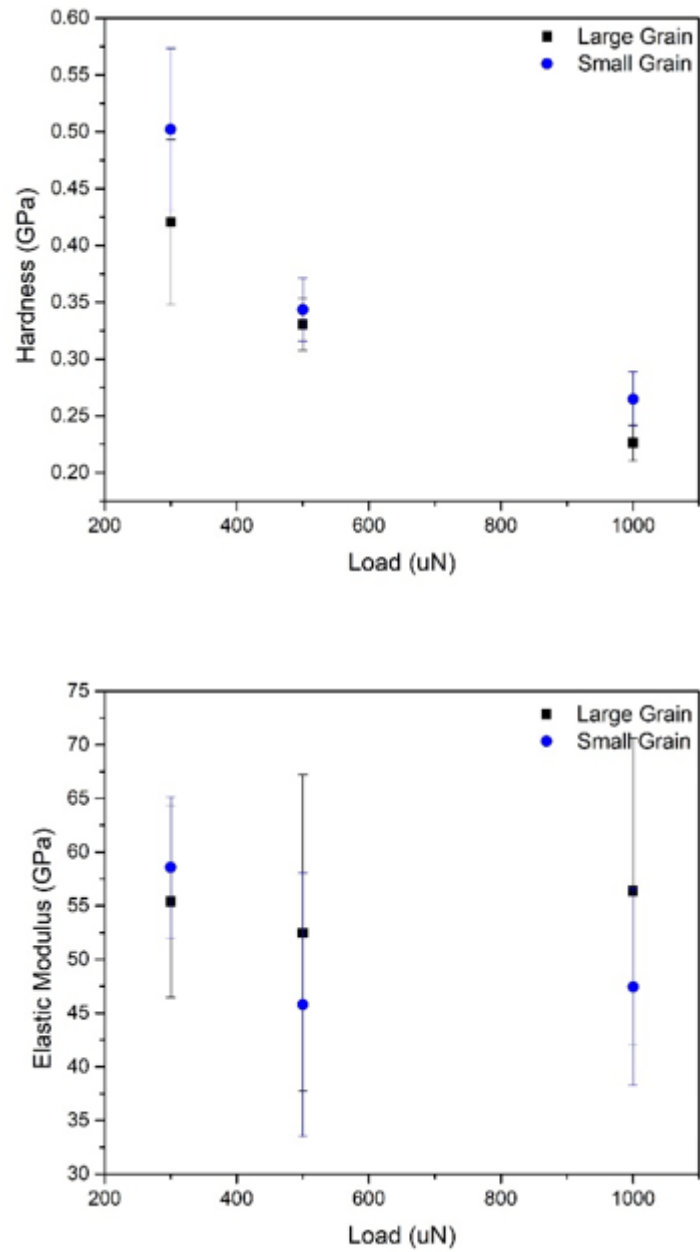


Figure 4.32: Calculated hardness and elastic modulus at different maximum load

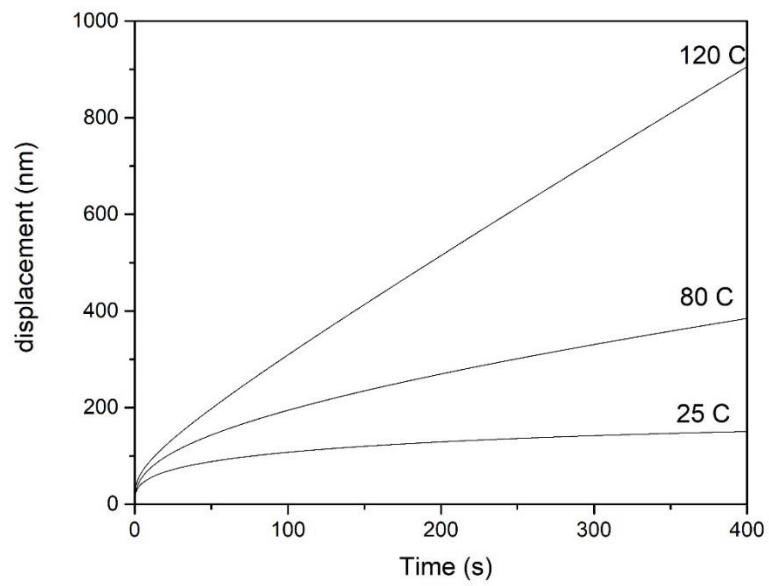


Figure 4.33: Adjusted displacement against time during dwell period

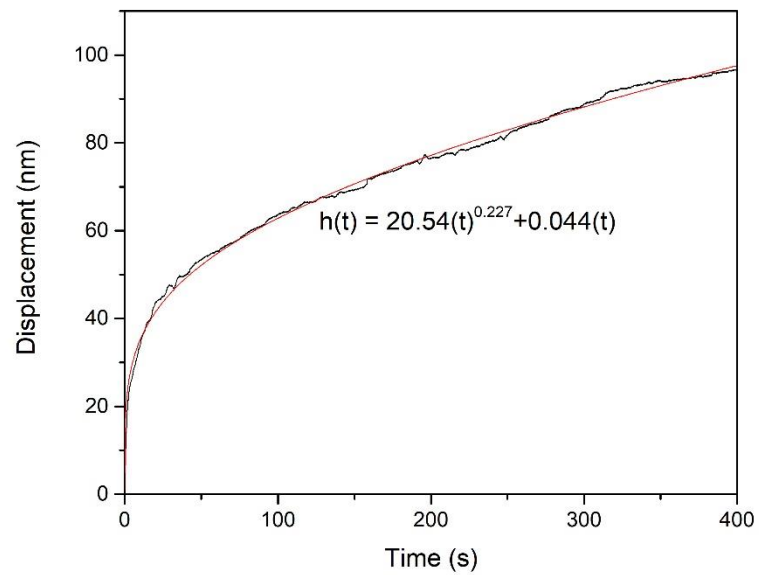


Figure 4.34: Fitted function of $h(t) = h_i + a(t-t_i)^b + kt$ with dwell time

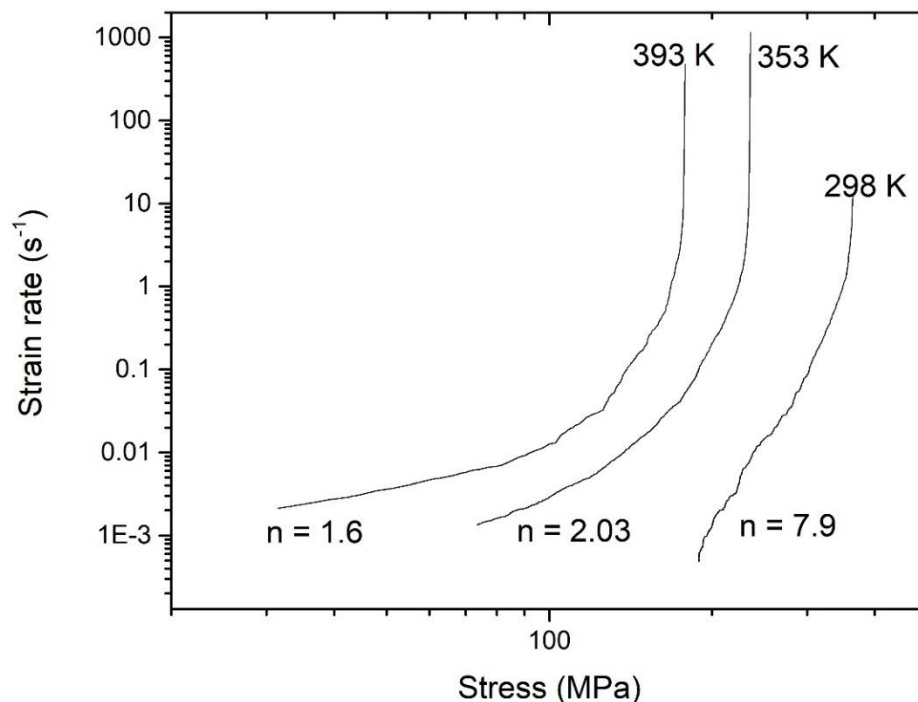


Figure 4.35: Strain rate as a function of stress at various temperature

The empirical equation, $h(t) = h_i + a(t-t_i)^b + kt$, is used to calculate the displacement rate by fitted to the displacement versus time curve at each constant indentation load. The fitting function is found to fit the creep curves at all indentation loads accurately as can be seen from the examples shown in figure 4.34.

Figure 4.35 shows strain rate as a function of stress at 298, 353 and 393 K. the stress exponents at various temperatures can be measured from the slope of this plot. it can be seen that the slope increased with decreasing temperature. This is also coincided with other research [128-130]. Hence, the stress exponent decreased as temperature decreased. It is evident from figure 4.35, that the nanoindentation creep at room temperature (298 K) follows a power-law with a stress exponent, n , of 6 which is comparable to conventional creep test and also typical for soft material such as Tin [130]. It is commonly found that stress exponent is between 6 -10 [13, 28, 126, 129]. The creep exponent greater than 5 is usually associated with dislocations movement,

including dislocation climb and dislocation glide. Dislocation motion is the dominant creep mechanism. Moreover, the nanoindentation creep at higher temperature (353 and 393 K) also follows a power-law but with a different stress exponent. The stress exponent at higher temperature is about 1. The stress exponent of 1 implies that grain boundary sliding becomes dominant creep mechanism. This suggest a change in mechanism of creep at different temperature. In all interested temperature, it shows power law break down where the observed stress level and strain rate does not follow the power law. This break down usually suggest a change in creep mechanism from diffusion-controlled flow to glide-controlled flow [121].

Marques et al suggest that at $T > 100$ C, the mechanism corresponding for this deformation is grain boundary diffusion with dislocation creep at $T < 100$ C. They also suggest a transition temperature of $0.65T_m$ for Sn-rich alloys [130].

Temperature (C)	Stress exponent (n)		Hardness (GPa)		Reduced Elastic Modulus (Gpa)		Elastic Modulus (Gpa)	
	Average	SD	Average	SD	Average	SD	Average	SD
25	7.91	1.00	0.27	0.023	60.17	2.54	55.73	2.49
80	2.03	0.51	0.088	0.029	32.83	5.03	29.68	4.66
120	1.63	0.61	0.090	0.049	27.09	2.64	24.36	2.44

Table 4.2: Stress exponent, hardness and elastic modulus of Sn-1 wt% Bi at different temperature

It is assumed that steady-state creep has been accomplished during creep holding where stress-exponent can be defined in the conventional power-law creep.

$$\dot{\epsilon} = A\sigma^n$$

The activation energy of creep can be calculated from the slope of strain rate plotted versus $1/T$ of the same applied stress similar to conventional creep. Figure 4.36 shows the arrhenius plot at a constant stress of 40 MPa. The activation energy calculated from the slope is 52.38 kJ/mol. Masami et. al [129] also got similar value for the activation enregy at temperature below 418 K, the value was 49 kJ/mol. The activation energy suggests the pipe diffusion phenomena. Eventhough the activation energy for grian boundary diffusion is also 40 kJ/mol [131], the grain size of the sample is much larger than the indentation which ensure that the experiments were done in the bulk material with no interfere of the grian boundary. Therefore, the mechanims of indentation creep of Sn-1%Bi is pipe diffusion.

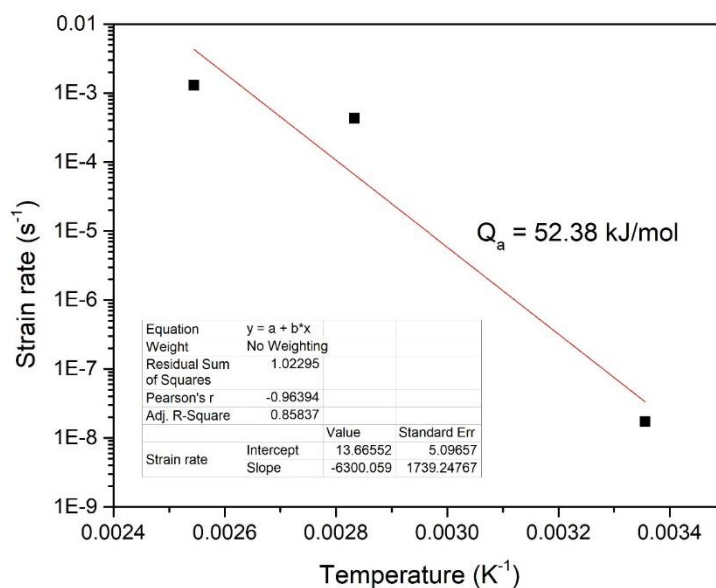


Figure 4.36: Log strtain rate against reciprocal temperature of Sn-1%Bi at 40 MPa

Creep mechanisms of Sn-1 wt.% Bi is suggested to be dislocation climb through core diffusion. Bi solute hinders the dislocation movement within Sn bulk lattice. In Sn-Bi alloy, it is typically to have higher creep resistance than pure metals as lower creep rates are found in the alloy at the same stress conditions. With activation energy close to 60 kJ/mol, dislocation pipe diffusion were also proposed for a high stress region [121].

The development of depth-sensing technique allows the creep studies on the small volumes of materials. This permits the hardness and elastic modulus of concise features. However, the question remains whether the stress exponents obtained from nanoindentation creep is verified and deformed in the same manner as conventional uniaxial tensile creep from bulk specimens. Figure 4.37 demonstrated that the nanoindentation creep can yield identical information about dislocations dynamics in a similar manner of conventional creep. However, low stress region in nanoindentation creep at 393 K show different stress exponent compare to the conventional test. This could be the result of surface deformation of Sn-alloy as well as Sn oxide layer.

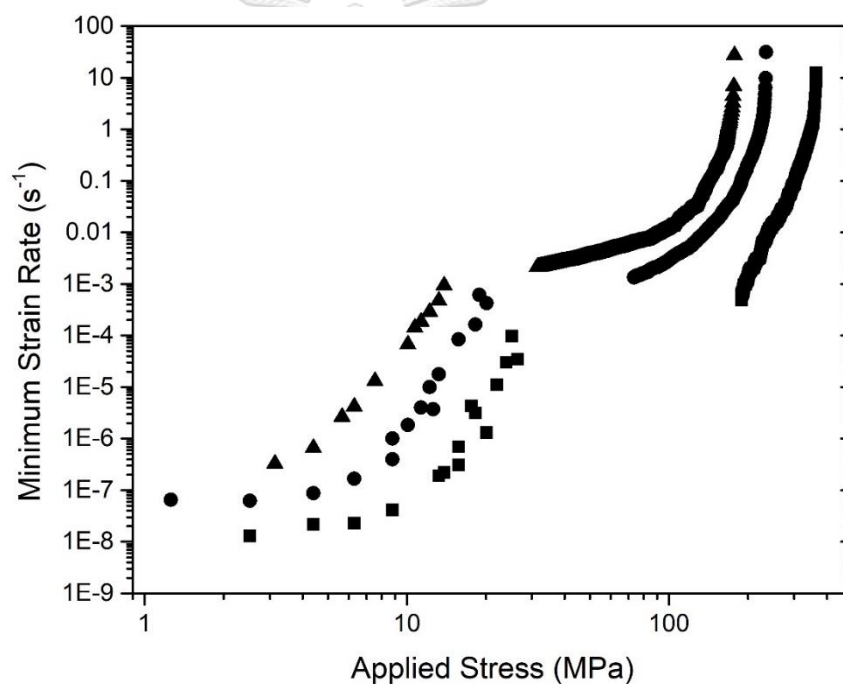


Figure 4.37: Superimposed of conventional creep and nanoindentation creep

Chapter 5

Applications of atomic diffusion in lapping process

Over the last decade, many machining techniques have been improved in order to fulfill the great demands for miniature components with greater surface quality, tighter tolerances and high precision accuracies. Many machining techniques are based on grinding or abrasive process [132]. Generally, machining techniques can be divided into free abrasive machining and fixed abrasive machining. Free abrasive machining utilizes abrasive particles for removal of material and surface finishing. The abrasive particles do not intentionally get embedded onto the lapping plate [132, 133], they are rather floated in the slurry which is placed between a lapping plate and a workpiece. They usually cause a combination of two-body and three-body wear types. The latter type is essential to secure a fine abrasive particle at a high density to enable material removal with smooth surface [134]. Despite this, there are two main mechanisms in material removal namely, mechanical mechanism and chemical mechanism [135]. Mechanical mechanism is involving erosion and abrasion for plastic deformation and fracture while chemical mechanism is a result from chemical reaction of products and dissolution of material.



Figure 5.1: System of lapping process

Lapping process is one technique of a precision machining. It is usually used in the manufacturing of components with greatest quality in terms of surface quality, precision accuracies and surface integrity. Numbers of precision manufacturing application use lapping process as a cutting-edge technology to achieve their high-

quality targets. It is understood to be a process used as an intention to remove materials and diminish the dimensions as well as reducing the surface roughness.

In lapping process, material could be mainly removed by the cutting action of the abrasive particles that are embedded onto the lapping plate. Lapping process usually comprises of three main parts: lapping plate, sample and abrasive particles as shown in figure 8. Mechanics of lapping process are carried out when the parts are put in contact with one another. Lapping plate and sample holder are usually rotated therefore there are various types of motions and friction during lapping process depending on relative velocity and rotation of lapping plate and sample holder.

It is well known that the abrasive particles, using in the lapping process, are said to be in distribution. Hence, they are uneven in size and shape. Since they are used in large amount, so the cutting action occurs continuously over the surface that they are becoming in contact with. It is common that if the abrasive particles are larger and harder, the finish will be smoother. The depth of the marks and scratch grooves could be used to define the surface roughness.

Prior to lapping process, the lapping plate needs preparation in order to create optimum cutting tool. Surface of the lapping plate requires flatness in order to be ready for abrasive particles for lapping. It usually prepares through shaving process, which is the process that is used to modify the surface of the lapping plate intended to create suitable area for abrasive particles. This step is performed by removing a layer of unwanted material with sharp edges tool in order to create flat areas.

After suitable surface of lapping plate is achieved, abrasive particles are pressed into the material lapping plate forming abrasive surface. There are few key parameters in charging process that can determine quantity of abrasive particles. For example, time, plate speed, oscillation speed, charging pressure, and slurry dropping cycle.

5.1 Evolution of abrasive particles on lapping plate during charging process

Diamond evolution during charging was observed through 17-inch experimental lapping plate which consists of 98.87 wt.% Sn and 1.13 wt.% Bi as shown in figure 5.2. It contains 1 cm diameter of holes at different area on the plate where it can be taken out without interfering with the process. Diamond density of every 10 minutes of charging were quantified from SEM images in order to study how much diamond on lapping plate has changed over charging process.

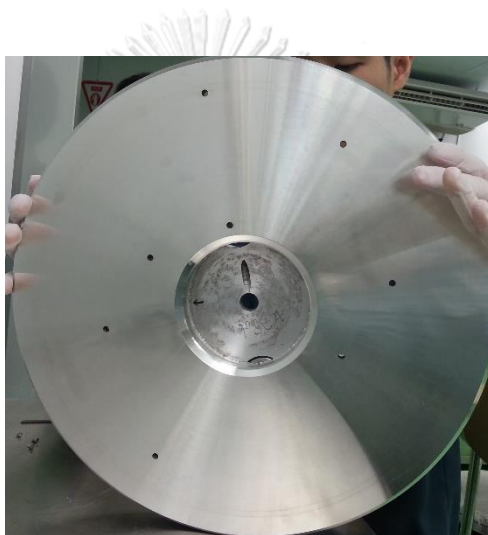


Figure 5.2: A 17-inch diameter experimental lapping plate

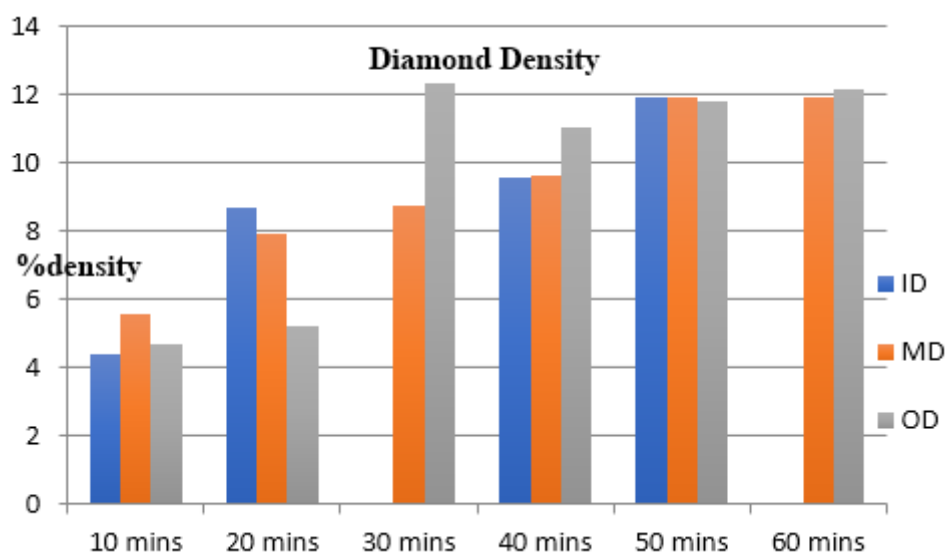


Figure 5.3: Evolution of diamond on lapping plate during charging process

As shown here in figure 5.3, diamond density was increasing over charging time. During first 30 minutes, diamond density was increasing from 0% to 9%. After 30 minutes of charging, it was shown that diamond density has reached maximum at approximately 12%.

5.2 Evolution of lapping plate during lapping process

Surface and topography of the lapping plate was studied throughout the charging and lapping process in order to observe the area available for abrasive embedment. Surface roughness were measured using surface profilometer (Taylor Hobson at Western Digital Co.ltd).

As shown in figure 5.4a), lapping plate after facing was shown here with average separation groove length of 106 μm . Groove depth of 7.4 μm was also measured and shown in figure 5.4b. After facing, lapping plate was shaved in order to provide land area for diamond to be charged later. Groove pitch from all inner diameter (ID), middle diameter (MD) and outer diameter (OD) were approximately 100 μm which are considered to be unchanged from facing process. Figure 5.5 and 5.6 also shows shape of the groove after shaving process. Groove depth was decreased from roughly 7 μm to 6 μm which could be imply that peak of the groove was removed by 1 μm in height and produced land width of 15.5, 18.06 and 22.90 μm from ID, MD and OD respectively.

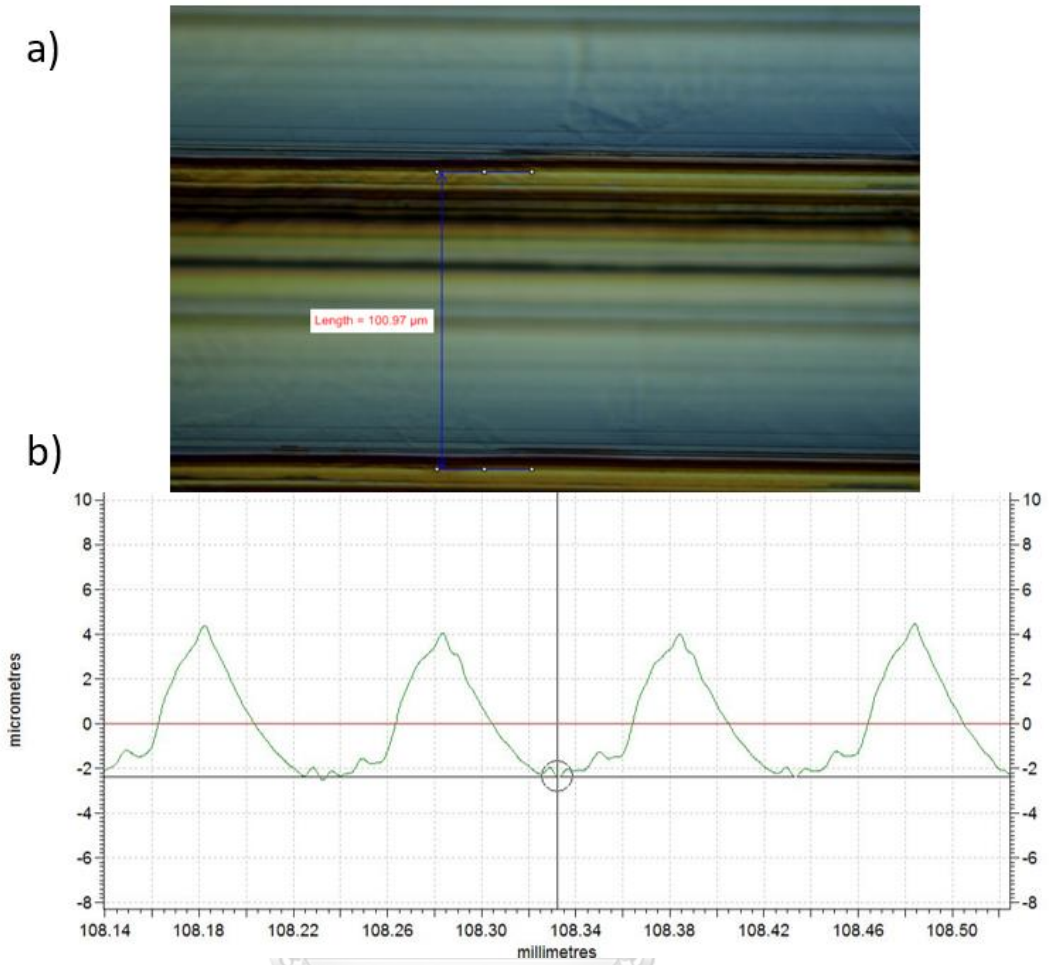


Figure 5.4: Sn-1%Bi plate after facing, taken from optical microscope at 50X magnification b) topography of Sn-1%Bi plate after facing

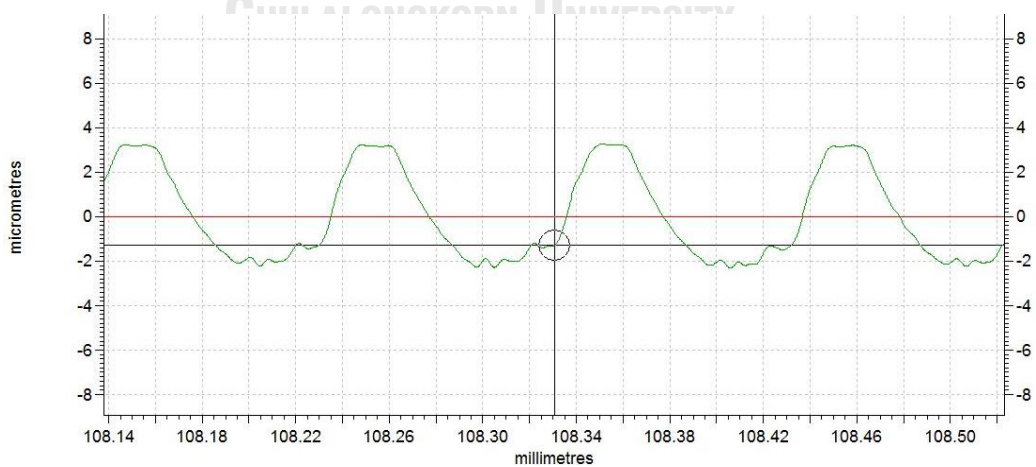


Figure 5.5: Groove shaped of Sn-1%Bi plate after shaving from Profilometer

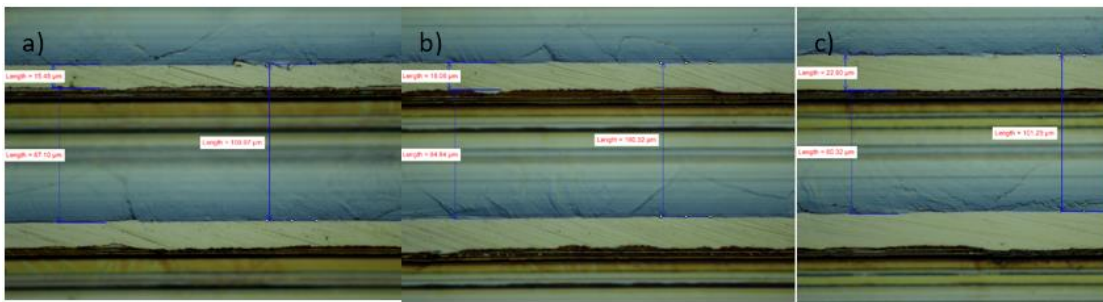


Figure 5.6: Sn-1%Bi plate after shaving taken from optical microscope with 50X magnification a) taken from inner diameter (ID) of lapping plate b) taken from middle diameter (MD) of lapping plate c) taken from outer diameter (OD) of lapping plate

Later, lapping plate was charged with 70 nm diamonds for 60 minutes, similar to normal groove plate preparation. Groove pitch of ID, MD and OD were measured and the values were approximately 100 μm , which are considered to be unchanged from shaving process. However, land width and groove width were changed from shaving process. Land width of ID, MD and OD are 19.2, 23.7, 29.17 μm respectively. While groove width of ID, MD and OD are 80.8, 77.6, 70.5 μm respectively. Land width of ID, MD and OD were increased by approximately 4 -7 μm due to loads applied during charging. Groove depth was decreased from roughly 6 μm to 5 μm , which was also due to loads applied during charging process.

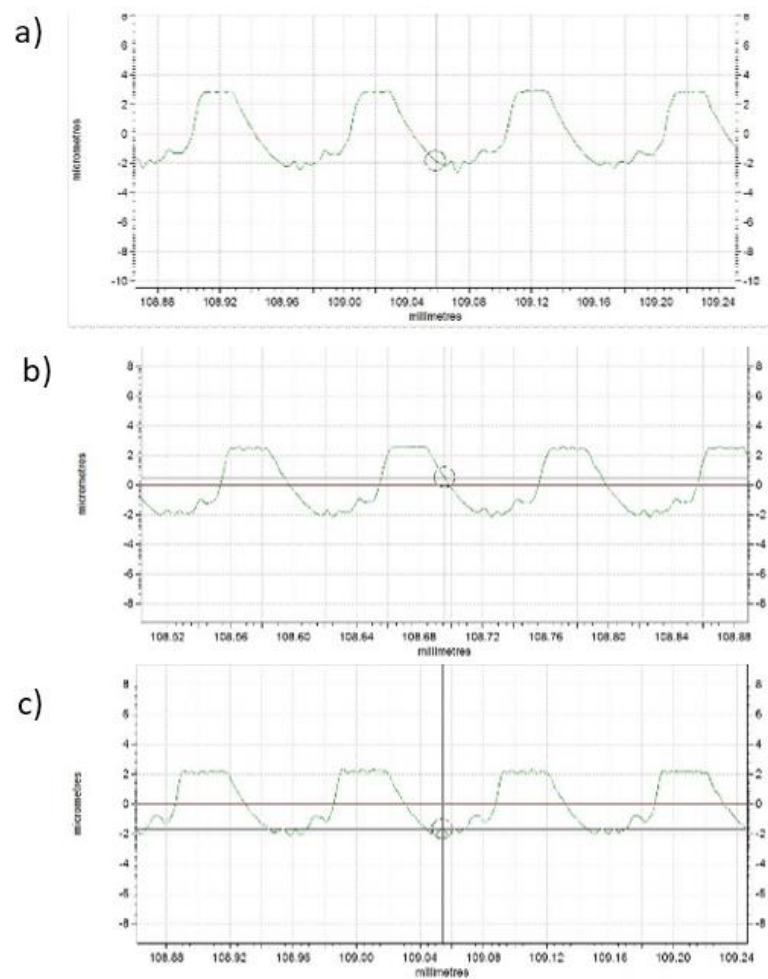


Figure 5.7: Groove shaped of Sn-1%Bi plate after charging from Profilometer a) taken from inner diameter (ID) of lapping plate b) taken from middle diameter (MD) of lapping plate c) taken from outer diameter (OD) of lapping plate

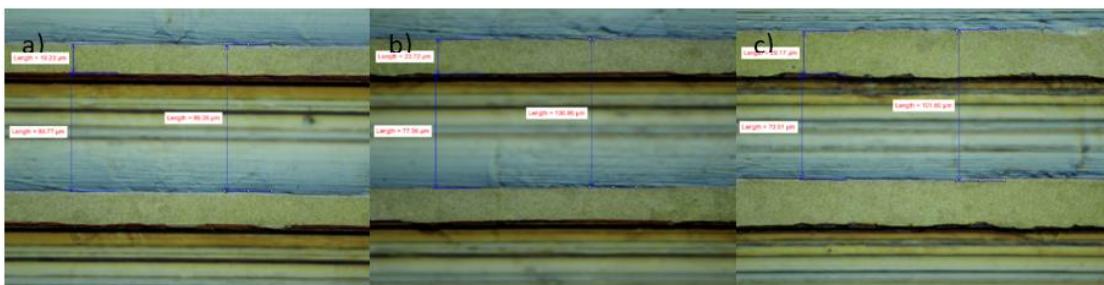


Figure 5.8: Sn-1%Bi plate after charging taken from optical microscope with 50X magnification a) taken from inner diameter (ID) of lapping plate b) taken from middle diameter (MD) of lapping

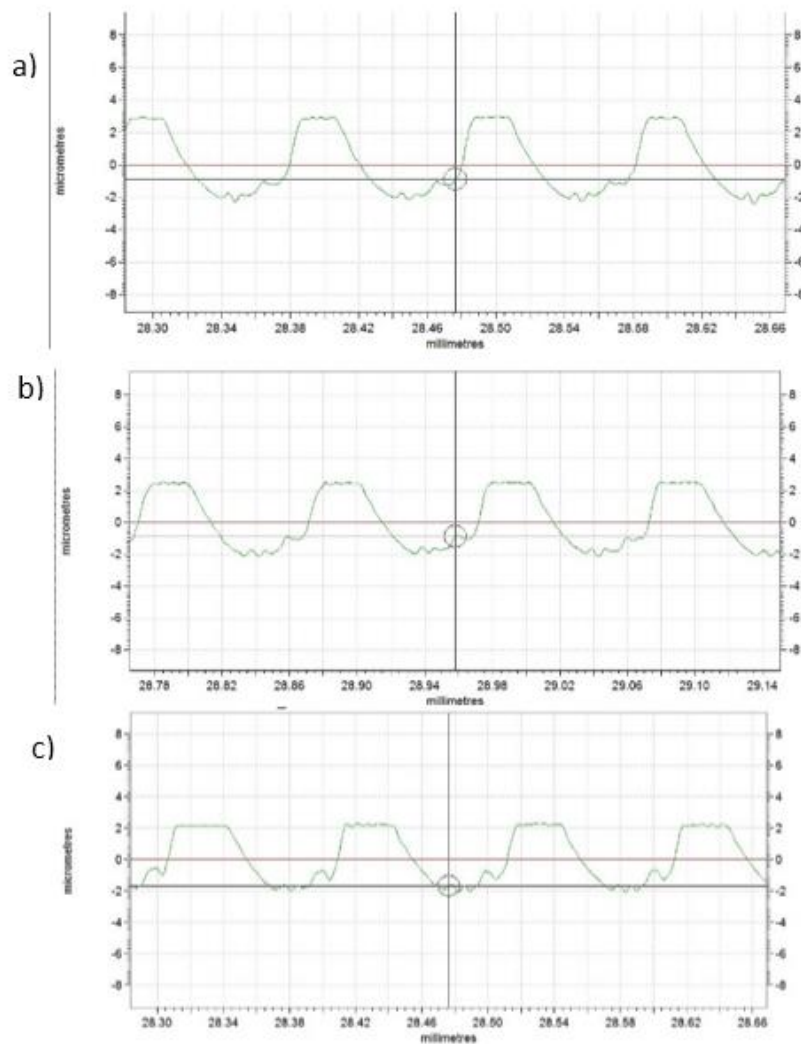


Figure 5.9: Groove shaped of Sn-1%Bi plate after 1 HR lapping from Profilometer a) taken from inner diameter (ID) of lapping plate b) taken from middle diameter (MD) of lapping plate c) taken from outer diameter (OD) of lapping plate

Afterward, lapping plate were running dummy run with sliders bars and were lapped for 60 minutes. Groove pitch of ID, MD and OD remained unchanged. However, land width and groove width were changed from charging process. Land width of ID, MD and OD are 20.2, 24.36, 31.0 μm respectively. While groove width of ID, MD and OD are 81.41, 76.6, 70.83 μm respectively. Land width of ID, MD and OD were increased by approximately 1-2 μm due to loads apply during charging. Decreasing of groove depth was not shown as expected, however it might due to short time of applied

load. Dimensions of groove on lapping plate during each step were measured and shown in figure 5.9 and 5.10. Moreover, land width is the largest in OD and getting smaller to MD and OD respectively. These diverse land widths between ID, MD and OD were due to the fact that lapping has round shape. Therefore, by using same condition from each step, OD area will have greatest diamond cutting head travelling distance.

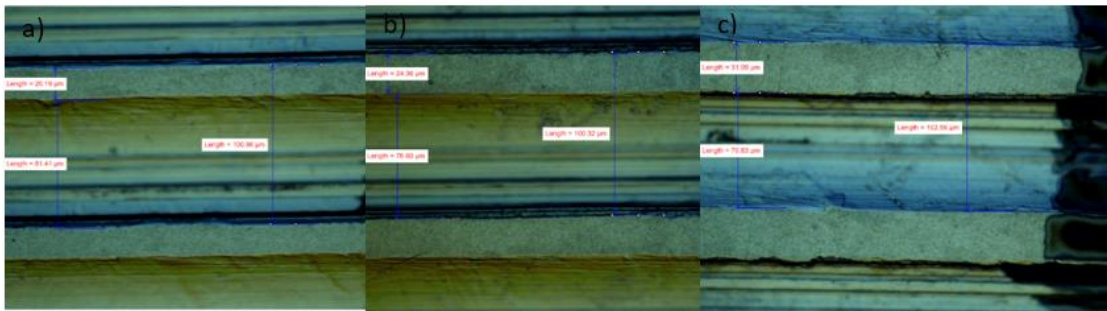


Figure 5.10: Sn-1%Bi lapping plate after 10 bars lapping taken from optical microscope with 50X magnification a) taken from inner diameter (ID) of lapping plate b) taken from middle diameter (MD) of lapping plate c) taken from outer diameter (OD) of lapping plate

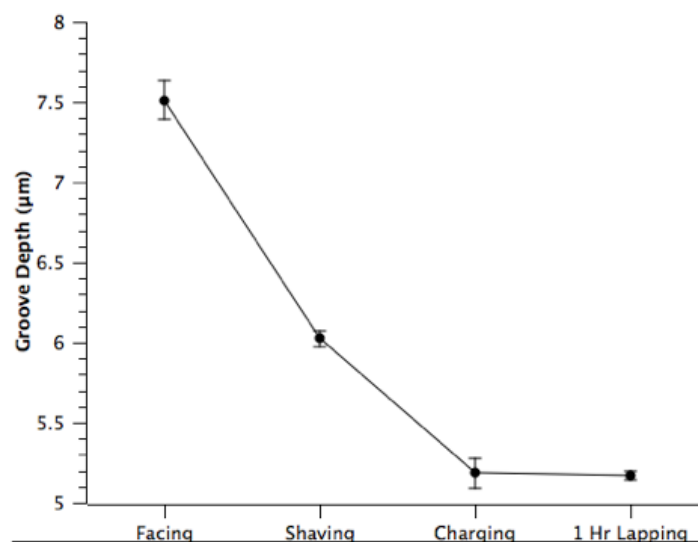


Figure 5.11: Groove depth of lapping plate after facing, shaving, charging and 1-hour lapping

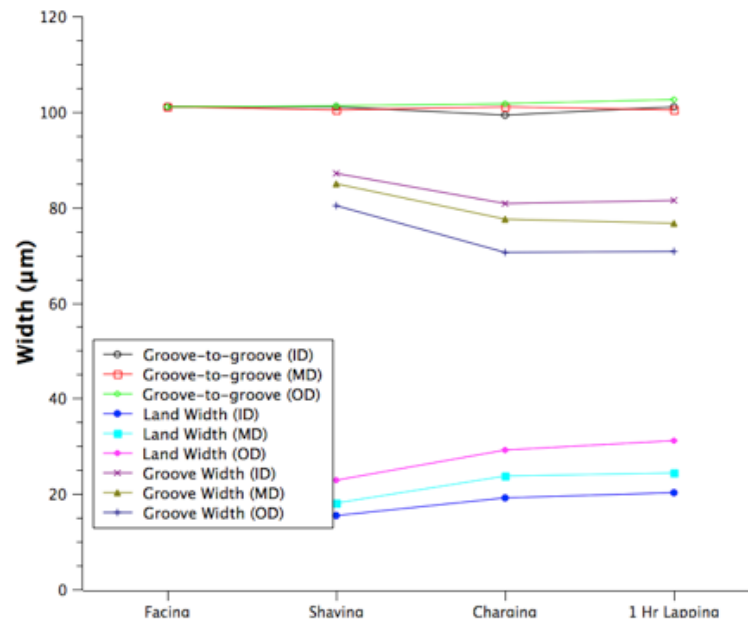


Figure 5.12: Dimension of groove plate from ID, MD and OD

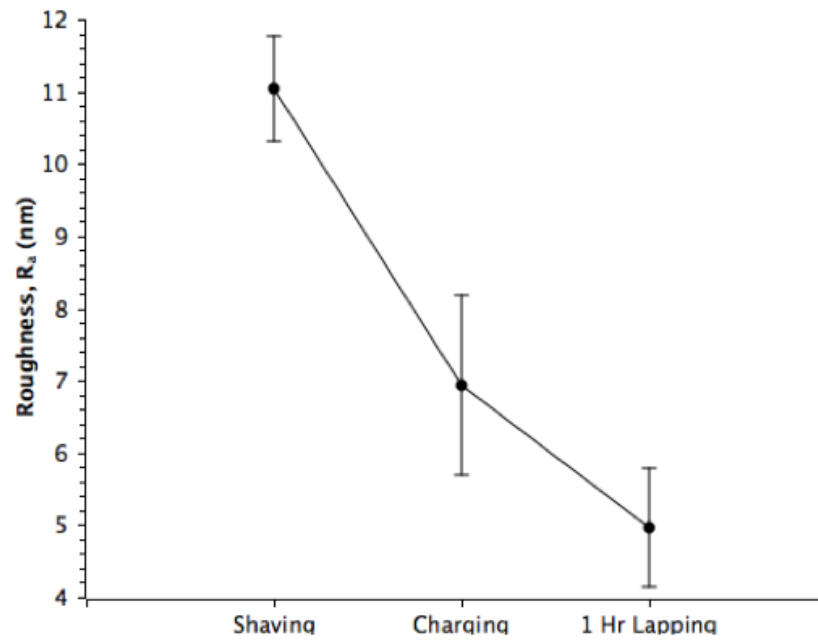


Figure 5.13: Roughness, Ra, of lapping plate

		Dimension (μm)									
	Groove Depth		Land width	Groove width	Peak to peak	Land width	Groove width	Peak to peak	Land width	Groove width	Peak to peak
	ID	MD	OD	ID	MD	OD	ID	MD	OD	ID	MD
1. Facing		7.42									
2. Shaving		6.06		15.48	87.10	100.97	18.06	84.84	100.32	22.90	80.32
3. charging	8.52	5.12	5.25	19.23	80.77	99.36	23.72	77.56	100.96	29.17	70.51
4. 1HR lapping	5.84	5.15	5.19	20.19	81.41	100.96	24.36	76.6	100.32	31.09	70.83
Peak to peak = 100.97											

Table 5.1: Measurement data of groove dimension

In addition, roughness of land area was also measured by using AFM scan. As shown in figure 5.13, the roughness of land area was decreasing from shaving with 11.2 nm R_a to 6.9 nm R_a after charging, later it was decreasing to 4.9 nm R_a after 1-hour lapping process. This decline may cause by the load applied from the machine. This was also found in other research group [136]. Furthermore, the reason behind greater reduction of R_a after charging than lapping is that main purpose of weight or applied loads during charging is to create flatter area for diamond embedment. As in the beginning period of charging, there were small number of diamonds got embedded onto lapping plate. However, as lapping plate got flattening, more diamonds were embedded.

Subsequently, Diamond density after each step was determined and quantified by using ImageJ program from 10,000X magnification of SEM. Figure 5.14a, b and c shows SEM images of lapping plate after shaving, charging and 1 hour of lapping. It can be qualitatively seen that diamond density on the lapping plate were reduced in number in table 5.2. Average diamond density from ID, MD and OD were shown in figure 5.15. From this data, it demonstrated that, both after charging and lapping, diamond density is greatest around MD and lowest around OD. This is because charging ring is presented and gave pressure more often around MD area comparing to ID and OD. Yet, ID area contained greater number of diamonds than OD due to the geometry shape of lapping plate. The inner diameter has smaller distance hence charging ring is presented more often than outer diameter area. It was also illustrated that diamond density from MD was decreasing from 15% diamond density after charging to 12% diamond density after 1-hour lapping.

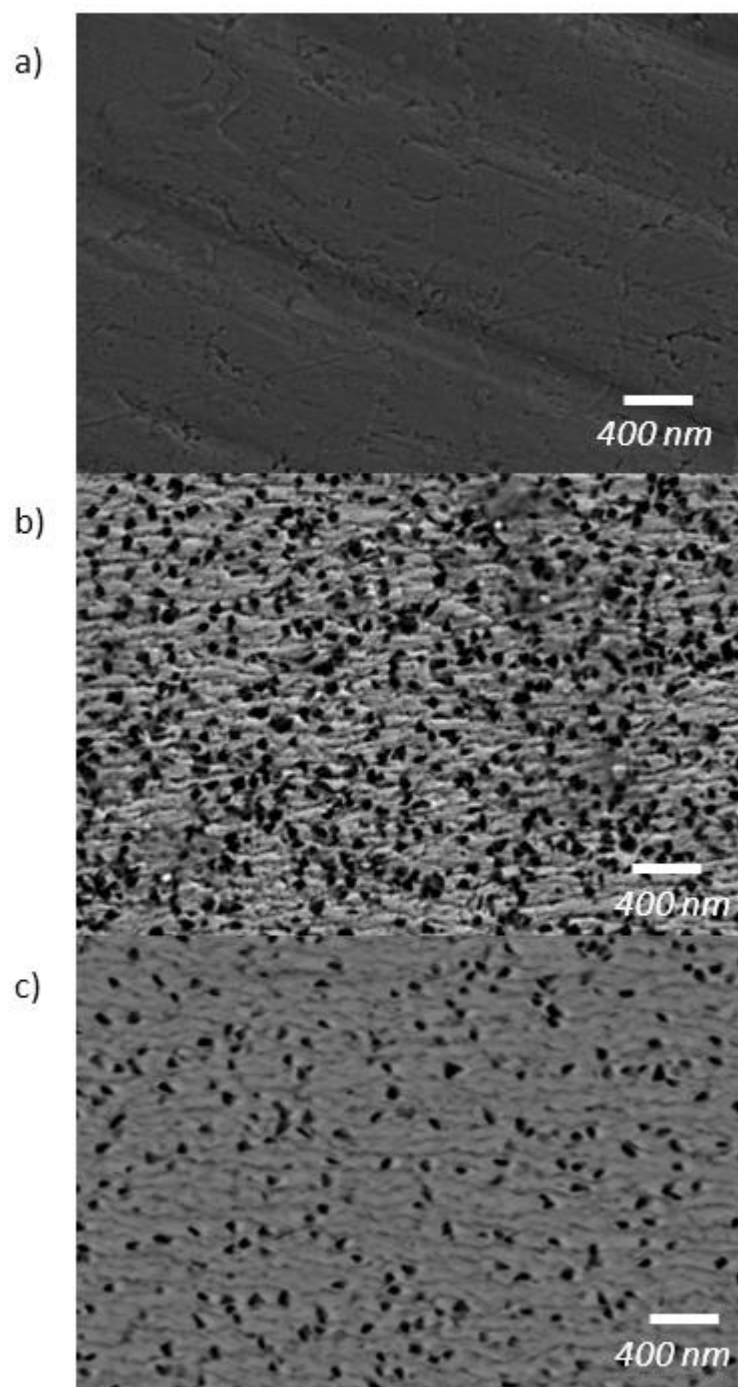


Figure 5.14: SEM image of lapping plate (MD) a) shaving b) charging c) 1-hour lapping

	Area fraction (%)		
	ID	MD	OD
1. Charging	15.10		
2. 1 HR lapping	8.70	12.48	6.36
3. 20 HR lapping	3.78	0.78	1.22

Table 5.2: Area fraction and average diamond size of ID, MD and OD from various processes

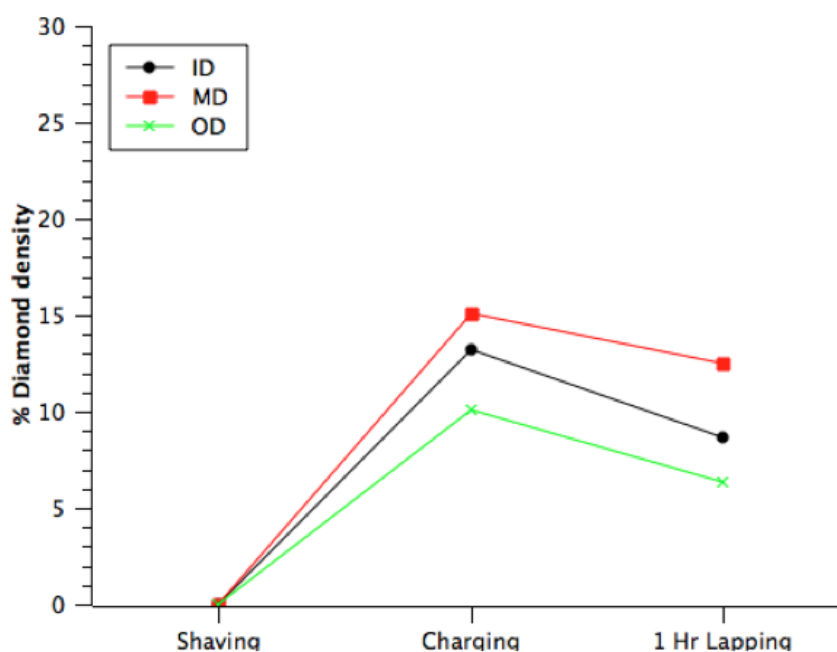


Figure 5.15: Diamond density on lapping plate

Furthermore, diamond protrusions were measured using AFM scan as shown in figure 5.16 and 5.17. AFM scan showed that diamonds protrusions were approximately 10-20 nm after charging process and 20 minutes lapping. Even though diamond protrusions were not changed after each process, embedment or impregnation of diamond assumption cannot be eliminated from the view since AFM measured only small area of diamond and data is not significantly different to conclude. Therefore, more data of these processes needed as well as more process in order to provide more accurate data to conclude.

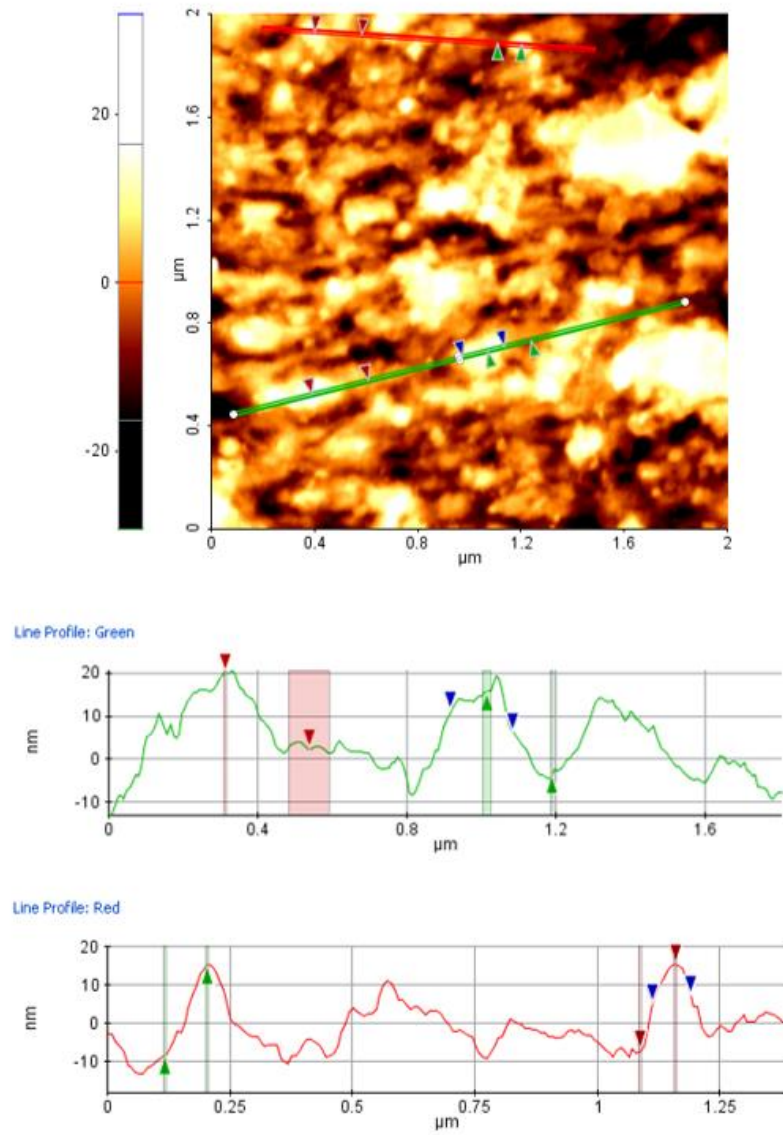


Figure 5.16: AFM scan of lapping plate after charging

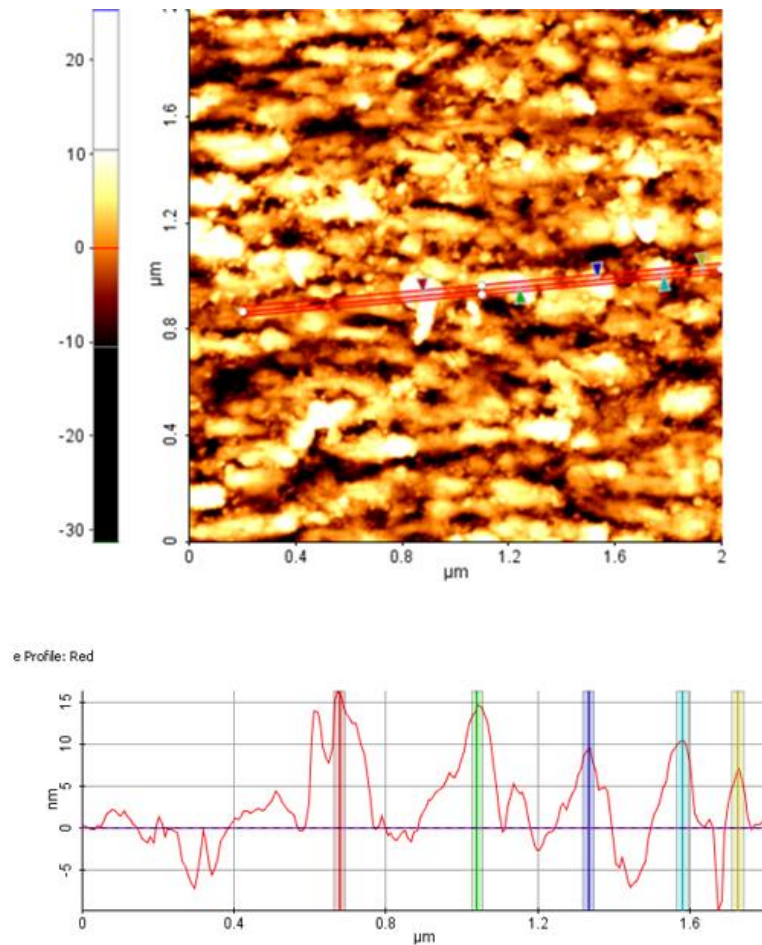


Figure 5.17: AFM scan of lapping plate after 20 minutes of lapping

จุฬาลงกรณ์มหาวิทยาลัย
CHULALONGKORN UNIVERSITY

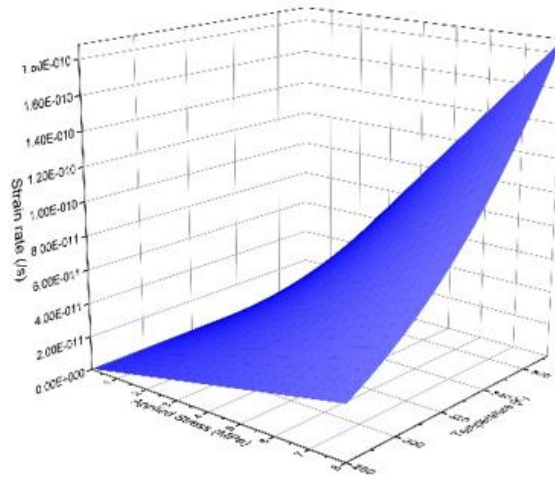
5.3 Lapping plate model

Creep equation, $\dot{\epsilon} = A\sigma^n \exp\left(-\frac{Q}{RT}\right)$, can be constructed from the experiments data above by substituting parameters back in order to find k constant or material constant. There are two regions which are low stress region and high stress region. Subsequently, there are two equations that can be applied in lapping and charging process as can be seen from figure 4.28 and 4.29 that there is a transition in slope around 8 MPa which also indicated that there is a change in creep mechanism. Creep equations are:

$$\dot{\epsilon} = (5 \times 10^{-9}) \sigma^1 \exp\left(-\frac{4,000}{RT}\right)$$

$$\dot{\epsilon} = (5 \times 10^{-9}) \sigma^8 \exp\left(-\frac{9,000}{RT}\right)$$

a)



b)

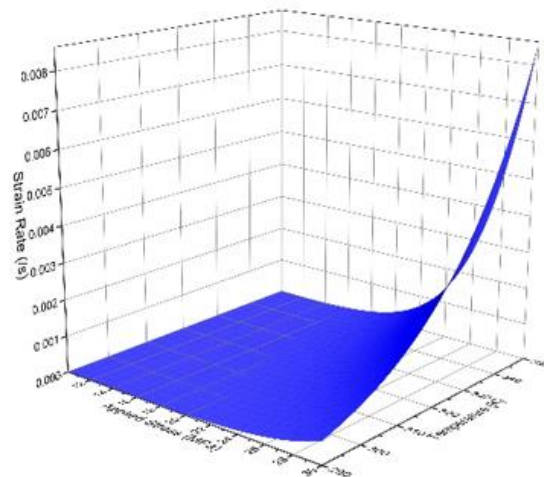


Figure 5.18: Plot of creep equation in a) low stress region and b) high stress region

Figure 5.18 shows plot of creep equation show relationship between strain rate, applied stress and temperature. This demonstrates that temperature is a critical factor in both low and high stress region. However, 18 kg force is applied during charging process. Stress during charging can be calculated with the assumption that charging blade is fully in contact with lapping plate. The calculated stress is 0.057 MPa which is in the low stress region hence the low stress region creep equation is valid during charging process.

5.4 Model Validation

According to the study of lapping plate evolution, the indirect measure of strain of lapping plate during charging is shown in figure 5.11a. Strain rate during charging is calculated since groove depth before charging is 6 μm whereas groove depth after charging is roughly around 5.2 μm . Therefore, strain rate during charging is 3.7×10^{-5} /s. Substituting this strain rate during charging into low stress region creep equation, stress is calculated as 6.08 MPa which is fall in the transition region. This evidence indicates that there is other factor that could also affect strain during charging process such as lubricant. From this calculation, it is also demonstrated that the current applied load generated creep in the mechanism that fall under low stress region. However, only a small increase in applied load or other factor that affect the stress could cause the change in creep mechanism to high stress region creep where the stress and temperature has much greater effect on strain rate.

Mr. Thanachai Boonchuduang had studied effect of varied charging parameter on diamond density which is shown in figure 5.19 and can be explained by low stress region creep equation. From the experiments, charging time was double but the diamond density was not affected. This is because diamond density has reached steady state after 40 minutes of charging. Charging force was reduced, which is equivalent to decrease in stress. From the equation, as stress is lower, strain rate will be lower as well.

Hence there will be lower diamond movement which cause more diamond to stay embedded on the lapping plate.

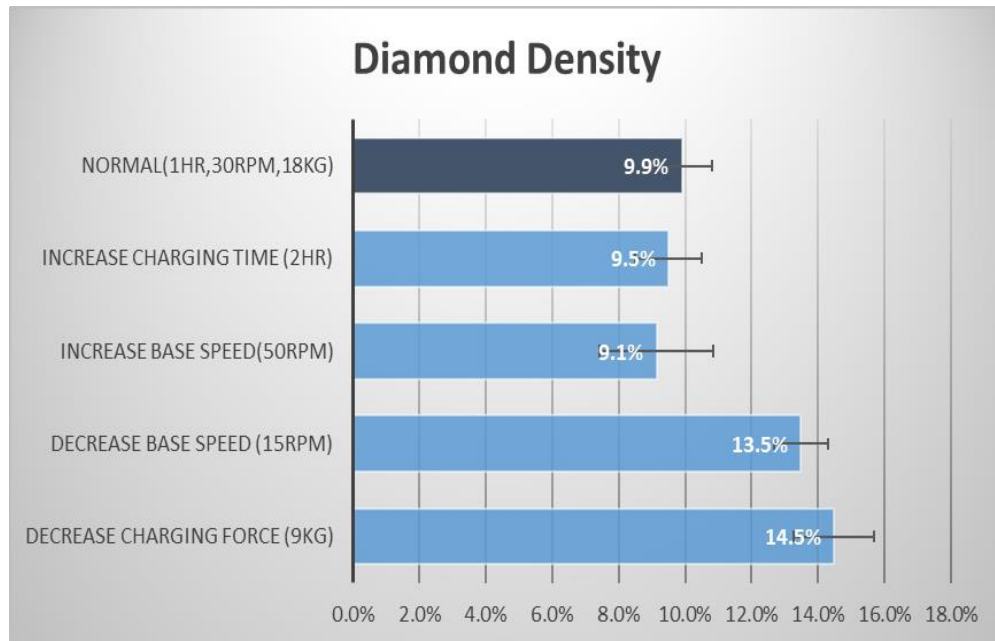


Figure 5.19: Diamond density with varied charging process parameter

(*data from Mr. Thanachai Boonchuduang)

Chapter 6

Conclusion

Tin-based alloy has regained its attention in the past decades for solder application and microelectronics industry since lead-contained solder has been precluded in many industries due to its health issues. Sn-Bi alloys has gain interests due to its low processing temperature, good bonding properties with metal and comparable mechanical properties with lead-contained solder. The low Bi contents was being investigated since the Bi atoms could allow the improvement of mechanical property and creep resistance. The results from conventional creep and indentation creep showed that the alloy had a typical multiple stress-dependent creep mechanism. The main mechanism at low stress region is glide dislocation while the dislocation pipe diffusion is corresponding to high stress region in creep behavior with the stress transition range of 7-10 MPa.

Metallic glasses have remarkable chemical, mechanical and physical properties. Composite of amorphous and crystalline have attracted considerable attention in order to gain most of its. They can be produced by partially crystallize the amorphous. This leads to better mechanical properties depending on the phase that was devitrified. The investigation of amorphous devitrification allows prediction and control phase stability. Cu-Zr binary system have great potentials since it is a good glass former and consists of various metastable and stable phases that could diversify property of the composite. Phase transformation during devitrification was observed and presented in table 6.1.

Information from creep deformation study can be further applied to the industrial problem. As they can mathematically explain many phenomena in wide range of applications. Understanding atomic diffusion and their mechanisms allow a systematic modification of lapping parameters for optimum results. From creep equation, stress is equivalent to charging force or lapping force while strain could be considered as movement of the plate material. As we know that during charging process, lapping plate

material is preferred to be moving for maximum diamond density, on the other hand, during lapping process, lapping material is preferred to be minimized its movement with the purpose of holding the diamonds. These relationships can be explained by creep equations.

$$\dot{\epsilon} = (5 \times 10^{-9})\sigma \exp\left(-\frac{4000}{RT}\right)$$

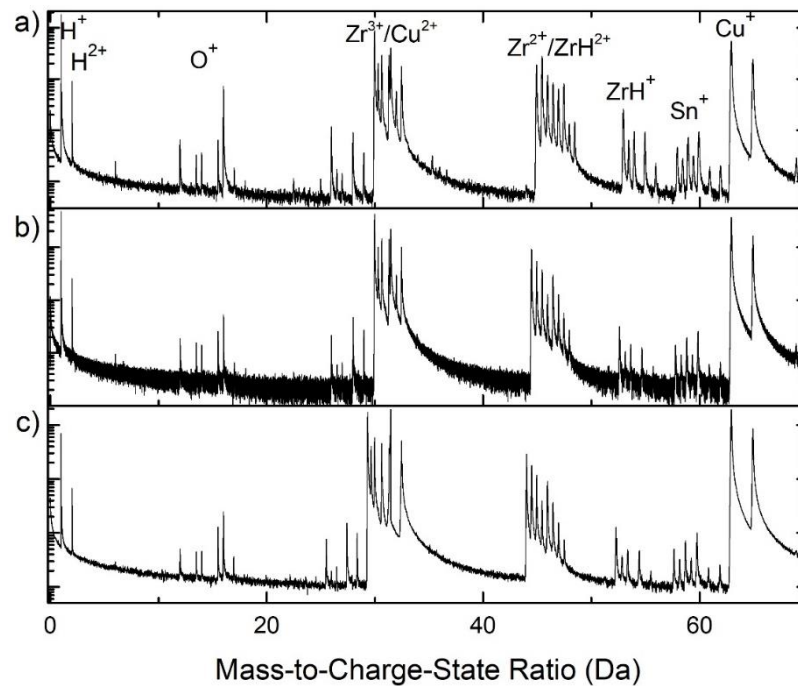
$$\dot{\epsilon} = (5 \times 10^{-9})\sigma^8 \exp\left(-\frac{9000}{RT}\right)$$

		TEM	APT	Phase Diagram
$\text{Cu}_{64}\text{Zr}_{36}$	T2	-	$\text{Cu}_{10}\text{Zr}_7$ Cu_8Zr_3	
	T3	$\text{Cu}_{10}\text{Zr}_7$ Cu_8Zr_3	$\text{Cu}_{10}\text{Zr}_7$ Cu_8Zr_3 CuZr_5Sn_3	$\text{Cu}_{10}\text{Zr}_7$ Cu_8Zr_3
$\text{Cu}_{56}\text{Zr}_{44}$	T2	-	$\text{Cu}_{10}\text{Zr}_7$	
	T3	CuZr $\text{Cu}_{10}\text{Zr}_7$ CuZr_2	$\text{Cu}_{10}\text{Zr}_7$ Cu_8Zr_3	$\text{Cu}_{10}\text{Zr}_7$ CuZr_2
$\text{Cu}_{50}\text{Zr}_{50}$	T2	-	CuZr	
	T3	$\text{Cu}_{10}\text{Zr}_7$ CuZr_2 CuZr_5Sn_3	CuZr CuZr_2 CuZr_5Sn_3	$\text{Cu}_{10}\text{Zr}_7$ CuZr_2

Table 6.1: Observed phase during devitrification under different techniques

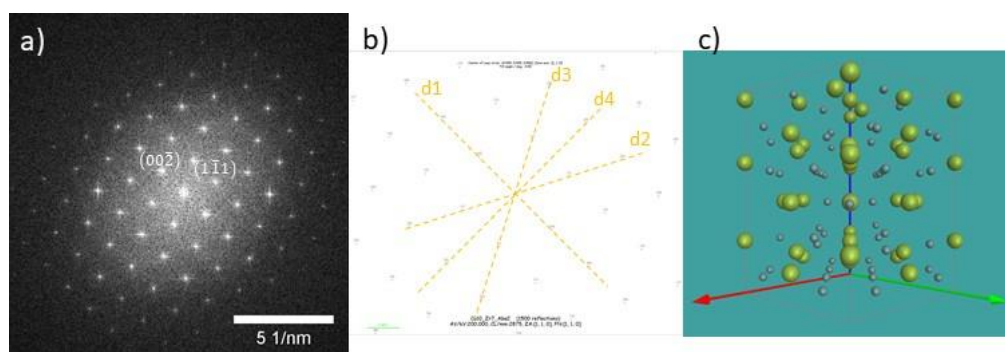
Chapter 7

Appendix



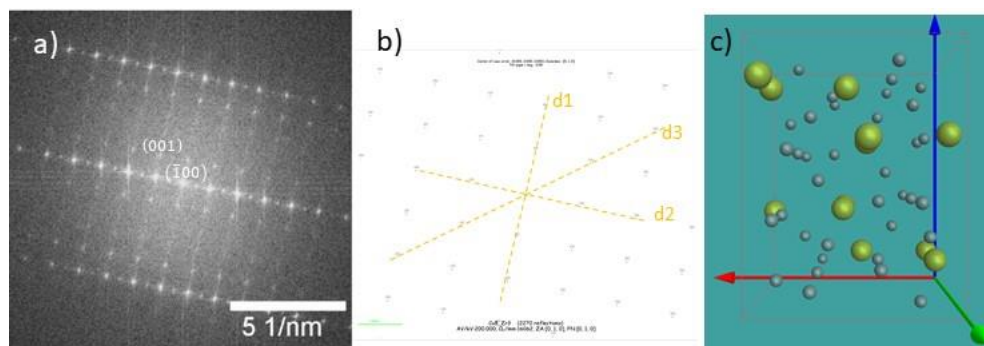
S1. Normalized mass spectra of a) $Cu_{64}Zr_{36}$ b) $Cu_{56}Zr_{44}$ c) $Cu_{50}Zr_{50}$ annealing at 823 K (T_3)

The normalized mass spectra obtained using LEAP are displayed. The mass spectra in figure S1a), b) and c) are from $Cu_{64}Zr_{36}$, $Cu_{56}Zr_{44}$ and $Cu_{50}Zr_{50}$, respectively. There are three main ionic species, H^+ , Zr^+ , $^{63}Cu^+$, Sn^+ , and ZrH^+ . The mass spectrum was manually fitted within the IVAS platform. The peak ranges were defined as the entire visible peak or adjusted manually for the long-tail-peaks. There are two crossover of the peak range which is an overlap between Zr and Cu at 30 Da and overlap between Zr and ZrH at 45 Da.



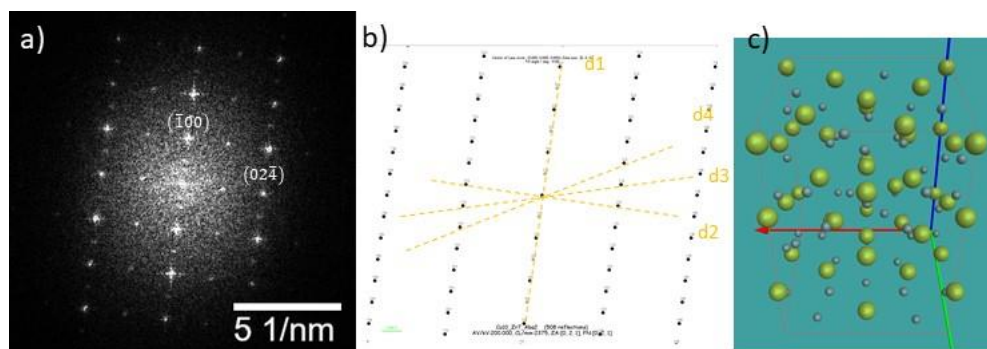
a)	AVG distance (1/nm)	real space (nm)	ratio	ratio	difference in angle
d1	1.59	0.63	d4/d1	1.91	90.37
d2	1.68	0.60	d3/d1	1.07	62.72
d3	1.71	0.59	d2/d1	1.05	62.23
d4	3.04	0.33			
b)					
d1	1.74	0.57	d4/d1	1.83	90.37
d2	1.81	0.55	d3/d1	1.02	62.02
d3	1.77	0.57	d2/d1	1.04	62.28
d4	3.19	0.31			

Figure S2 is a calculated FFT of HRTEM corresponding to figure 3.7d). while figure S2b) shows the simulated SAED pattern of $\text{Cu}_{10}\text{Zr}_7$ on [010] zone axis. C) shows the simulated atomic structure. Table a) show the measurement from FFT and b) show the measurement from the simulated SAED pattern.



a)	AVG distance (1/nm)	real space (nm)	ratio	ratio	difference in angle
d1	0.91	1.04	d4/d1		
d2	1.20	0.83	d3/d1	1.62	39.28
d3	1.56	0.64	d2/d1	1.25	89.49
b)					
d1	1.30	0.77	d4/d1		
d2	1.31	0.77	d3/d1	1.43	43.95
d3	1.86	0.54	d2/d1	1.00	89.52

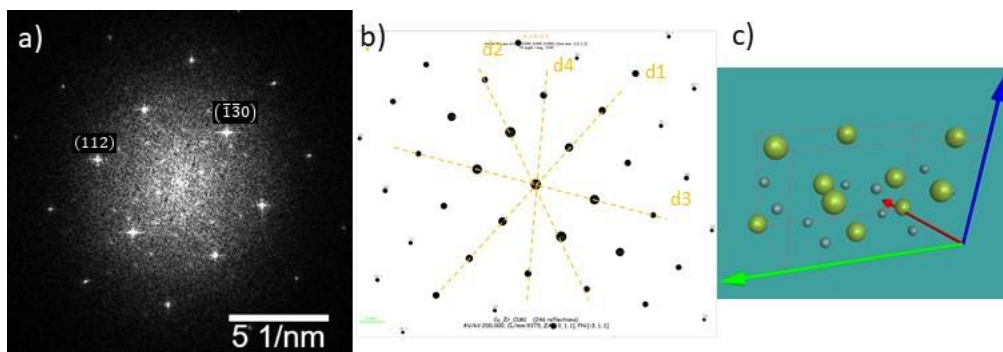
Figure S3a) is a calculated FFT of HRTEM corresponding to figure 3.7e) while figure S3b) shows the simulated SAED pattern of Cu_8Zr_3 on [010] zone axis. C) shows the simulated atomic structure. Table a) show the measurement from FFT and b) show the measurement from the simulated SAED pattern.



a)	AVG distance (1/nm)	real space (nm)	ratio	ratio	difference in angle
d1	1.08	0.93	d4/d1	4.11	60.81
d2	3.86	0.26	d3/d1	3.76	74.25
d3	4.04	0.25	d2/d1	3.59	90.36
d4	4.42	0.23			

b)	AVG distance (1/nm)	real space (nm)	ratio	ratio	difference in angle
d1	1.10	0.91	d4/d1	4.11	60.62
d2	3.98	0.25	d3/d1	3.75	74.45
d3	4.14	0.24	d2/d1	3.60	89.71
d4	4.54	0.22			

Figure S4a) is a calculated FFT of HRTEM corresponding to the right area in figure 3.10d) while figure S4b) shows the simulated SAED pattern of $\text{Cu}_{10}\text{Zr}_7$ on [021] zone axis. C) shows the simulated atomic structure. Table a) show the measurement from FFT and b) show the measurement from the simulated SAED pattern.



a)	AVG distance (1/nm)	real space (nm)	ratio	ratio	difference in angle
d1	3.51	0.29	d4/d1	1.78	38.34
d2	4.12	0.24	d3/d1	1.26	61.58
d3	4.41	0.23	d2/d1	1.17	69.61
d4	6.25	0.16			
b)					
d1	3.88	0.26	d4/d1	1.77	36.90
d2	4.59	0.22	d3/d1	1.22	62.28
d3	4.71	0.21	d2/d1	1.18	67.72
d4	6.87	0.15			

Figure S5a) is a calculated FFT of HRTEM corresponding to the left area in figure 3.10d) while figure S5b) shows the simulated SAED pattern of CuZr on $[\bar{3}11]$ zone axis. C) shows the simulated atomic structure. Table a) show the measurement from FFT and b) show the measurement from the simulated SAED pattern.

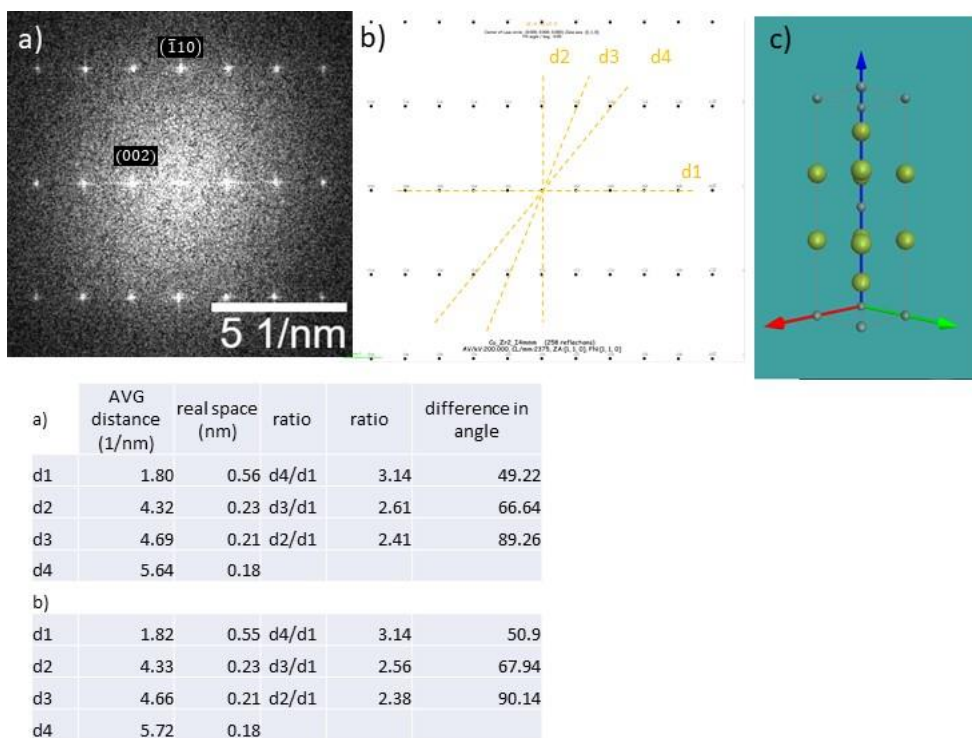
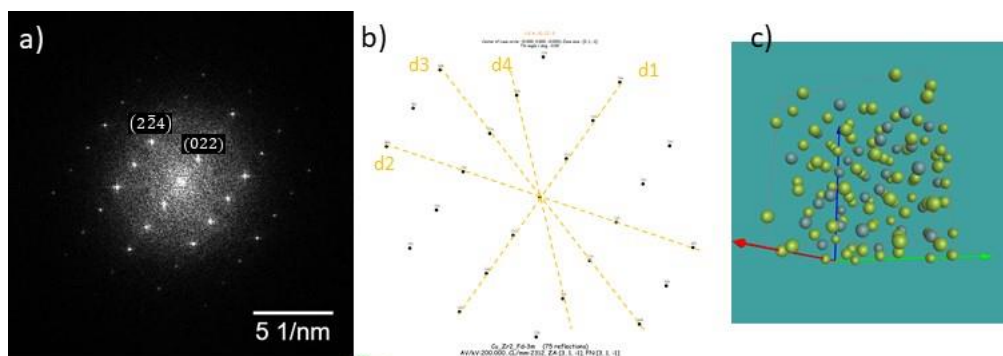
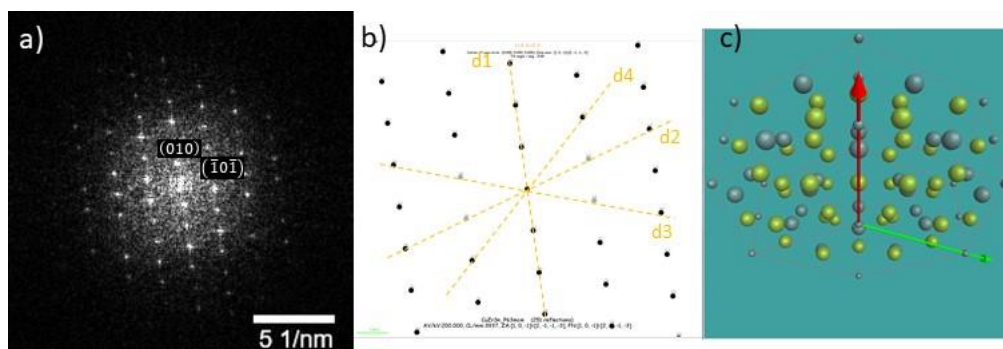


Figure S6a) is a calculated FFT of HRTEM corresponding to the right area in figure 3.10e) while figure S6b) shows the simulated SAED pattern of CuZr_2 on [110] zone axis. C) shows the simulated atomic structure. Table a) show the measurement from FFT and b) show the measurement from the simulated SAED pattern.



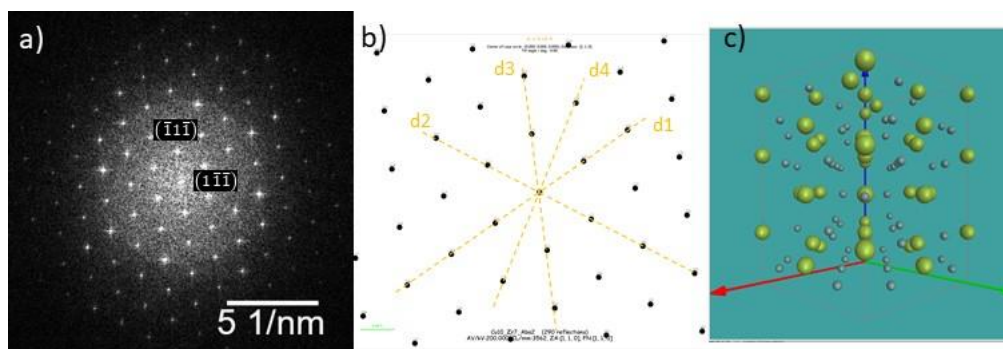
a)	AVG distance (1/nm)	real space (nm)	ratio	ratio	difference in angle
d1	1.84	0.54	d4/d1	2.16	48.42
d2	3.14	0.32	d3/d1	1.75	74.03
d3	3.22	0.31	d2/d1	1.70	72.49
d4	3.99	0.25			
b)					
d1	2.45	0.41	d4/d1	2.17	48.48
d2	4.13	0.24	d3/d1	1.70	73.47
d3	4.16	0.23	d2/d1	1.68	72.74
d4	5.33	0.19			

Figure S7a) is a calculated FFT of HRTEM corresponding to the right area in figure 3.12d) while figure S7b) shows the simulated SAED pattern of CuZr_2 on $[31\bar{1}]$ zone axis. C) shows the simulated atomic structure. Table a) show the measurement from FFT and b) show the measurement from the simulated SAED pattern.



a)	AVG distance (1/nm)	real space (nm)	ratio	ratio	difference in angle
d1	1.36	0.74	d4/d1	2.13	46.01
d2	2.18	0.46	d3/d1	1.61	72.27
d3	2.19	0.46	d2/d1	1.60	71.45
d4	2.89	0.35			
b)					
d1	1.38	0.73	d4/d1	2.07	45.8
d2	2.22	0.45	d3/d1	1.62	72
d3	2.23	0.45	d2/d1	1.61	72
d4	2.86	0.35			

Figure S8a) is a calculated FFT of HRTEM corresponding to the left area in figure 3.12d) while figure S8b) shows the simulated SAED pattern of CuZr_5Sn_3 on $[10\bar{1}]$ zone axis. C) shows the simulated atomic structure. Table a) show the measurement from FFT and b) show the measurement from the simulated SAED pattern.



	AVG distance (1/nm)	real space (nm)	ratio	ratio	difference in angle
a)					
d1	1.61	0.62	d4/d1	1.78	32.58
d2	1.68	0.60	d3/d1	1.06	62.34
d3	1.71	0.58	d2/d1	1.04	62.11
d4	2.86	0.35			
b)					
d1	1.56	0.64	d4/d1	1.89	32.65
d2	1.70	0.59	d3/d1	1.16	62.80
d3	1.81	0.55	d2/d1	1.09	62.80
d4	2.95	0.34			

Figure S9a) is a calculated FFT of HRTEM corresponding to the left area in figure 3.12e) while figure S9b) shows the simulated SAED pattern of $\text{Cu}_{10}\text{Zr}_7$ on [110] zone axis. C) shows the simulated atomic structure. Table a) show the measurement from FFT and b) show the measurement from the simulated SAED pattern.

		TEM	Frequency distribution	Proximity histogram
$\text{Cu}_{63}\text{Zr}_{36}$	T_2	-	$\text{Cu}_{10}\text{Zr}_7$ Cu_8Zr_3	$\text{Cu}_{10}\text{Zr}_7$ Cu_8Zr_3
	T_3	$\text{Cu}_{10}\text{Zr}_7$ Cu_8Zr_3	$\text{Cu}_{10}\text{Zr}_7$ Cu_8Zr_3	$\text{Cu}_{10}\text{Zr}_7$ Cu_8Zr_3 CuZr_5Sn_3
$\text{Cu}_{56}\text{Zr}_{44}$	T_2	-	$\text{Cu}_{10}\text{Zr}_7$	$\text{Cu}_{10}\text{Zr}_7$
	T_3	CuZr $\text{Cu}_{10}\text{Zr}_7$ CuZr_2	$\text{Cu}_{10}\text{Zr}_7$	$\text{Cu}_{10}\text{Zr}_7$ Cu_8Zr_3
$\text{Cu}_{50}\text{Zr}_{50}$	T_2	-	CuZr	CuZr
	T_3	$\text{Cu}_{10}\text{Zr}_7$ CuZr_2 CuZr_5Sn_3	CuZr	CuZr CuZr_2 CuZr_5Sn_3



REFERENCES

1. Telford, M., *The case for bulk metallic glass*. *Materials Today*, 2004. 7(3): p. 36-43.
2. Löffler, J.F., *Bulk metallic glasses*. *Intermetallics*, 2003. 11(6): p. 529-540.
3. Xu, D., et al., *Bulk metallic glass formation in binary Cu-rich alloy series – Cu_{100-x}Zr_x (x=34, 36, 38.2, 40 at.%) and mechanical properties of bulk Cu₆₄Zr₃₆ glass*. *Acta Materialia*, 2004. 52(9): p. 2621-2624.
4. Ray, R., B.C. Giessen, and N.J. Grant, *New non-crystalline phases in splat cooled transition metal alloys*. *Scripta Metallurgica*, 1968. 2(6): p. 357-359.
5. Altounian, Z., T. Guo-hua, and J.O. Strom-Olsen, *Crystallization characteristics of Cu-Zr metallic glasses from Cu₇₀Zr₃₀ to Cu₂₅Zr₇₅*. *Journal of Applied Physics*, 1982. 53(7): p. 4755-4760.
6. Buschow, K.H.J., *Short-range order and thermal stability in amorphous alloys*. *Journal of Physics F: Metal Physics*, 1984. 14(3): p. 593-607.
7. Wang, D., et al., *Bulk metallic glass formation in the binary Cu-Zr system*. *Applied Physics Letters*, 2004. 84(20): p. 4029-4031.
8. Inoue, A. and W. Zhang, *Formation, Thermal Stability and Mechanical Properties of Cu-Zr and Cu-Hf Binary Glassy Alloy Rods*. *MATERIALS TRANSACTIONS*, 2004. 45(2): p. 584-587.
9. Wang, N., et al., *The thermodynamic re-assessment of the Cu-Zr system*. *Calphad*, 2006. 30(4): p. 461-469.
10. Okamoto, H., *Cu-Zr (Copper-Zirconium)*. *Journal of Phase Equilibria and Diffusion*, 2008. 29(2): p. 204-204.
11. Shen, L., P. Septiwerdani, and Z. Chen, *Elastic modulus, hardness and creep performance of SnBi alloys using nanoindentation*. *Materials Science and Engineering: A*, 2012. 558: p. 253-258.
12. Gault, B., *A Brief Overview of Atom Probe Tomography Research*. *Applied Microscopy*, 2016. 46(3): p. 117-126.

13. Shen, L., et al., *Creep behaviour of eutectic SnBi alloy and its constituent phases using nanoindentation technique*. Journal of Alloys and Compounds, 2013. **574**: p. 98-103.
14. Shen, L., et al., *Nanoindentation creep of tin and aluminium: A comparative study between constant load and constant strain rate methods*. Materials Science and Engineering: A, 2012. **532**: p. 505-510.
15. Callister, W.D., *Materials Science And Engineering: An Introduction*. 2007: John Wiley & Sons. 840.
16. Schuh, C., et al., *Thermal-cycling creep of γ -TiAl-based alloys*. Intermetallics, 2000. **8**: p. 339-343.
17. Fischer-Cripps, A.C., *A simple phenomenological approach to nanoindentation creep*. Materials Science and Engineering: A, 2004. **385**: p. 74-82.
18. *Nanoindentation Lecture 1 Basic Principle*. PowerShow.
19. Fischer-Cripps, A.C., *Critical review of analysis and interpretation of nanoindentation test data*. Surface and Coatings Technology, 2006. **200**(14): p. 4153-4165.
20. Fischer-Cripps, A.C., *The IBIS handbook of nanoindentation*. 2009, Forestville, NSW: Fischer-Cripps Laboratories.
21. Doerner, M.F. and W.D. Nix, *A method for interpreting the data from depth-sensing indentation instruments*. Journal of Materials Research, 1986. **1**(4): p. 601-609.
22. Schuh, C.A., *Nanoindentation studies of materials*. Materials Today, 2006. **9**(5): p. 32-40.
23. Panich*, N. and S. Yong, *Improved Method to Determine the Hardness and Elastic Moduli using Nano-Indentation*. CURRENT APPLIED SCIENCE AND TECHNOLOGY, 2005. **5**(2): p. 483-492.
24. Oliver, W.C. and G.M. Pharr, *Measurement of hardness and elastic modulus by instrumented indentation: Advances in understanding and refinements to methodology*. Journal of Materials Research, 2004. **19**(1): p. 3-20.

25. Li, X. and B. Bhushan, *A review of nanoindentation continuous stiffness measurement technique and its applications*. *Materials Characterization*, 2002. **48**(1): p. 11-36.
26. Mayo, M.J. and W.D. Nix, *A micro-indentation study of superplasticity in Pb, Sn, and Sn-38 wt% Pb*. *Acta Metallurgica*, 1988. **36**(8): p. 2183-2192.
27. Dean, J., et al., *A critical assessment of the "stable indenter velocity" method for obtaining the creep stress exponent from indentation data*. *Acta Materialia*, 2014. **80**: p. 56-66.
28. Raman, V. and R. Berriche, *An investigation of the creep processes in tin and aluminum using a depth-sensing indentation technique*. *Journal of Materials Research*, 1992. **7**(3): p. 627-638.
29. Kim, Y.-J. and D.N. Seidman, *Atom-Probe Tomographic Analyses of Hydrogen Interstitial Atoms in Ultrahigh Purity Niobium*. *Microscopy and Microanalysis*, 2015. **21**(3): p. 535-543.
30. Kwon, O.-J., et al., *Formation of amorphous phase in the binary Cu–Zr alloy system*. *Metals and Materials International*, 2006. **12**: p. 207-212.
31. Altounian, Z., et al., *The influence of oxygen and other impurities on the crystallization of NiZr₂ and related metallic glasses*. *Journal of Applied Physics*, 1987. **61**(1): p. 149-155.
32. Chang, H.J., et al., *Observation of artifact-free amorphous structure in Cu–Zr-based alloy using transmission electron microscopy*. *Materials Science and Engineering: A*, 2005. **406**(1): p. 119-124.
33. Kneller, E., Y. Khan, and U. Gorres, *The Alloy System Copper-Zirconium*. *Z. Metallkunde*, 1986. **77**(43): p. 152-163.
34. Apreutesei, M., et al., *Zr–Cu thin film metallic glasses: An assessment of the thermal stability and phases' transformation mechanisms*. *Journal of Alloys and Compounds*, 2015. **619**: p. 284-292.
35. Kalay, I., M. J. Kramer, and R. E. Napolitano, *Crystallization Kinetics and Phase Transformation Mechanisms in Cu₅₆Zr₄₄ Glassy Alloy*. *Metallurgical and Materials*

- Transactions A, 2015. **46**.
36. Freed, R.L. and J.B. Vander Sande, *The metallic glass Cu₅₆Zr₄₄: Devitrification and the effects of devitrification on mechanical properties*. Acta Metallurgica, 1980. **28**(1): p. 103-121.
 37. Poettgen, R., *ChemInform Abstract: The Stannide Zr₅CuSn₃*. Cheminform, 2010. **28**.
 38. Zhou, S.H. and R.E. Napolitano, *Phase stability for the Cu–Zr system: First-principles, experiments and solution-based modeling*. Acta Materialia, 2010. **58**(6): p. 2186-2196.
 39. Wei, R., et al., *Formation of CuZr-based bulk metallic glass composites containing nanometer-scale B2-CuZr phase through sub-T_g annealing*. Journal of Alloys and Compounds, 2014. **617**: p. 699-706.
 40. Cui, X., et al., *Study of the reversible intermetallic phase: B2-type CuZr*. Intermetallics, 2013. **36**: p. 21-24.
 41. Kalay, I., M. J. Kramer, and R.E. Napolitano, *High-Accuracy X-Ray Diffraction Analysis of Phase Evolution Sequence During Devitrification of Cu₅₀Zr₅₀ Metallic Glass*. Metallurgical and Materials Transactions A, 2011. **42**: p. 1144-1153.
 42. Cullinan, T., et al., *Kinetics and Mechanisms of Isothermal Devitrification in Amorphous Cu₅₀Zr₅₀*. Metallurgical and Materials Transactions A, 2015. **46**(2): p. 600-613.
 43. Yedla, N., et al., *Effect of nano-crystallization on the plasticity in Cu–Zr amorphous binary alloys*. Intermetallics, 2010. **18**: p. 2419-2424.
 44. Braga, M.H., et al., *Experimental liquidus points and invariant reactions in the Cu–Zr system*. 1998.
 45. Fadonougbo, J.O., et al., *Nanometer-scale phase separation and formation of delta ZrH₂ in Cu–Zr binary amorphous alloys*. Journal of Alloys and Compounds, 2017. **721**: p. 646-652.
 46. Freed, R.L. and J.B. Vander Sande, *A study of the crystallization of two non-crystalline Cu–Zr alloys*. Journal of Non-Crystalline Solids, 1978. **27**(1): p. 9-28.

47. Wen, D.D., et al., *Correlation of the heredity of icosahedral clusters with the glass forming ability of rapidly solidified Cu_xZr_{100-x} alloys*. Journal of Non-Crystalline Solids, 2015. **427**: p. 199-207.
48. Dong, Q., et al., *A comparative study of glass-forming ability, crystallization kinetics and mechanical properties of $Zr_{55}Co_{25}Al_{20}$ and $Zr_{52}Co_{25}Al_{23}$ bulk metallic glasses*. Journal of Alloys and Compounds, 2019. **785**: p. 422-428.
49. Petrzhik, M., V. Molokanov, and E. Levashov, *On conditions of bulk and surface glass formation of metallic alloys*. Journal of Alloys and Compounds, 2017. **707**: p. 68-72.
50. Huang, Y., et al., *Cooling rate effect of nanomechanical response for a Ti-based bulk metallic glass*. Journal of Non-Crystalline Solids, 2010. **356**(20): p. 966-970.
51. Tao, M., et al., *Deformation and crystallization of Zr-based amorphous alloys in homogeneous flow regime*. Journal of Materials Research, 2010. **25**(6): p. 1137-1148.
52. Lu, J., G. Ravichandran, and W.L. Johnson, *Deformation behavior of the $Zr_{41.2}Ti_{13.8}Cu_{12.5}Ni_{10}Be_{22.5}$ bulk metallic glass over a wide range of strain-rates and temperatures*. Acta Materialia, 2003. **51**(12): p. 3429-3443.
53. Wang, G.Y., et al., *The influence of Pd on tension-tension fatigue behavior of Zr-based bulk-metallic glasses*. International Journal of Fatigue, 2010. **32**(3): p. 599-604.
54. González, S., et al., *Deformation and strain rate sensitivity of a Zr-Cu-Fe-Al metallic glass*. Materials Science and Engineering: A, 2011. **528**(9): p. 3506-3512.
55. Mihaylov, L., et al., *Nanoporous metallic structures by de-alloying bulk glass forming Zr-based alloys*. Intermetallics, 2018. **98**: p. 148-153.
56. Zhu, S., et al., *Zr-based bulk metallic glass composite with in situ precipitated nanocrystals*. Journal of Alloys and Compounds, 2014. **586**: p. 155-158.
57. Wang, D., H. Tan, and Y. Li, *Pinpoint the Best Glass Forming Alloy by Microstructure Study in $Cu_8Zr_3-Cu_{10}Zr_7$ Eutectic System of Cu-Zr Binary System*. Journal of Metastable and Nanocrystalline Materials, 2005. **24-25**: p. 287-290.

58. Zhang, S., S. Ye, and P. Yu, *Novel dealloying structures and ageing behaviors of Cu-Zr metallic glass ribbons*. Journal of Non-Crystalline Solids, 2017. **458**: p. 61-64.
59. Dong, D. and C. Dong, *Composition interpretation procedures of bulk metallic glasses via example of Cu₆₄Zr₃₆*. Journal of Non-Crystalline Solids, 2017. **460**: p. 125-129.
60. Weinberg, M.C., *A test of the johnson-mehl-avrami equation*. Journal of Crystal Growth, 1987. **82**(4): p. 779-780.
61. Peixoto, E.B., et al., *Study of the dynamic of crystallization of an amorphous Fe₄₀Ni₄₀P₁₄B₆ ribbon through Johnson-Mehl-Avrami model*. Journal of Alloys and Compounds, 2018. **731**: p. 1275-1279.
62. Keryvin, V., et al., *Thermal stability and crystallisation of a Zr₅₅Cu₃₀Al₁₀Ni₅ bulk metallic glass studied by in situ ultrasonic echography*. Intermetallics, 2002. **10**(11): p. 1289-1296.
63. Mattern, N., et al., *Structural behavior of CuxZr_{100-x} metallic glass (x=35-70)*. Journal of Non-Crystalline Solids, 2008. **354**(10): p. 1054-1060.
64. Wu, Y.L., et al., *Melting and crystallization of colloidal hard-sphere suspensions under shear*. Proceedings of the National Academy of Sciences, 2009. **106**(26): p. 10564-10569.
65. Theisen, E.A., et al., *Transient behavior of the planar-flow melt spinning process*. Chemical Engineering Science, 2010. **65**(10): p. 3249-3259.
66. Thompson, K., et al., *In situ site-specific specimen preparation for atom probe tomography*. Ultramicroscopy, 2007. **107**(2-3): p. 131-139.
67. Li, L. and W.H. de Jeu, *Shear-Induced Smectic Ordering in the Melt of Isotactic Polypropylene*. Physical Review Letters, 2004. **92**(7): p. 075506.
68. Lohwongwatana, B., J. Schroers, and W.L. Johnson, *Strain Rate Induced Crystallization in Bulk Metallic Glass-Forming Liquid*. Physical Review Letters, 2006. **96**(7): p. 075503.
69. Mattern, N., et al., *Phase separation in Ni₇₀Nb_{30-x}Y_x glasses*. Intermetallics,

2010. **18**(10): p. 1842-1845.
70. Gray, R.A., et al., *Crystallization of molecular liquids through shear-induced nucleation*. Proceedings of the Royal Society of London. Series A: Mathematical and Physical Sciences, 1995. **448**(1932): p. 113-120.
71. Onuki, A., *Phase transitions of fluids in shear flow*. Journal of Physics: Condensed Matter, 1997. **9**(29): p. 6119-6157.
72. Schroers, J., et al., *Gold based bulk metallic glass*. Applied Physics Letters, 2005. **87**(6): p. 061912.
73. Way, C., et al., *Shear rate dependence of viscosity and configurational entropy of the Zr_{41.2}Ti_{13.8}Cu_{12.5}Ni_{10.0}Be_{22.5} metallic glass forming liquid*. Journal of Alloys and Compounds, 2007. **434-435**: p. 88-91.
74. Chen, C.-W. and W.-S. Hwang, *A three-dimensional fluid flow model for puddle formation in the single-roll rapid solidification process*. Applied Mathematical Modelling, 1995. **19**(12): p. 704-712.
75. Budhani, R.C., T.C. Goel, and K.L. Chopra, *Melt-spinning technique for preparation of metallic glasses*. Bulletin of Materials Science, 1982. **4**(5): p. 549-561.
76. Hui, X.D., et al., *Transient heat transfer and fluid dynamics during the melt spinning process of Fe₇₈Si₉B₁₂Mo amorphous alloy*. Science and Technology of Advanced Materials, 2001. **2**(1): p. 265-270.
77. Sun, Z. and H.A. Davies, *Computer modelling of ribbon formation in the melt spinning of crystalline metals*. Materials Science and Engineering, 1988. **98**: p. 71-74.
78. Kim, J.M., et al., *Transient solutions of the dynamics of film casting process using a 2-D viscoelastic model*. Journal of Non-Newtonian Fluid Mechanics, 2005. **132**(1): p. 53-60.
79. Kissinger, H.E., *Reaction Kinetics in Differential Thermal Analysis*. Analytical Chemistry, 1957. **29**(11): p. 1702-1706.
80. Ruitenberg, G., *Applying Kissinger analysis to the glass transition peak in*

- amorphous metals*. Thermochemica Acta, 2003. **404**(1): p. 207-211.
81. Yang, Y.J., et al., *Crystallization kinetics of a bulk amorphous Cu–Ti–Zr–Ni alloy investigated by differential scanning calorimetry*. Journal of Alloys and Compounds, 2006. **415**(1): p. 106-110.
 82. Liu, F., et al., *Nucleation, growth and impingement modes deduced from isothermally and isochronally conducted phase transformations: Calorimetric analysis of the crystallization of amorphous Zr50Al10Ni40*. Acta Materialia, 2010. **58**(19): p. 6542-6553.
 83. Qiao, J.C. and J.M. Pelletier, *Crystallization kinetics in Cu46Zr45Al7Y2 bulk metallic glass by differential scanning calorimetry (DSC)*. Journal of Non-Crystalline Solids, 2011. **357**(14): p. 2590-2594.
 84. Peng, C., et al., *Crystallization kinetics of Zr60Cu25Fe5Al10 bulk metallic glass*. Journal of Non-Crystalline Solids, 2014. **405**: p. 7-11.
 85. Cheng, S., et al., *Non-isothermal crystallization kinetics of Zr41.2Ti13.8Cu12.5Ni10Be22.5 amorphous alloy*. Thermochemica Acta, 2014. **587**: p. 11-17.
 86. Cui, X., et al., *Phase competition of Cu64Zr36 and its effect on glass forming ability of the alloy*. Crystal Research and Technology, 2013. **48**(1): p. 11-15.
 87. Mridha, S., et al., *Evolution of atomic distribution during devitrification of bulk metallic glass investigated by atom probe microscopy*. Materials Letters, 2015. **158**: p. 99-103.
 88. Sohn, S.W., et al., *Phase separation in bulk-type Gd–Zr–Al–Ni metallic glass*. Intermetallics, 2012. **23**: p. 57-62.
 89. Tanner, L.E. and R. Ray, *Phase separation in Zr□Ti□Be metallic glasses*. Scripta Metallurgica, 1980. **14**(6): p. 657-662.
 90. Ren, Y.L., et al., *Phase separation and plastic deformation in an Mg-based bulk metallic glass*. Journal of Alloys and Compounds, 2010. **493**(1): p. L42-L46.
 91. Lai, T., H. Yin, and M.L. Lind, *The hydrogen permeability of Cu–Zr binary amorphous metallic membranes and the importance of thermal stability*. Journal of

- Membrane Science, 2015. **489**: p. 264-269.
92. Paglieri, S.N., et al., *Hydrogen permeability, thermal stability and hydrogen embrittlement of Ni-Nb-Zr and Ni-Nb-Ta-Zr amorphous alloy membranes*. Journal of Membrane Science, 2011. **378**(1): p. 42-50.
 93. Rubanov, S. and P.R. Munroe, *FIB-induced damage in silicon*. Journal of Microscopy, 2004. **214**(3): p. 213-221.
 94. Andrzejczuk, M., et al., *TEM characterization of the artefacts induced by FIB in austenitic stainless steel*. Journal of Microscopy, 2010. **237**(3): p. 439-442.
 95. Belz, J., et al., *Direct investigation of (sub-) surface preparation artifacts in GaAs based materials by FIB sectioning*. Ultramicroscopy, 2016. **163**: p. 19-30.
 96. Chang, Y., et al., *Ti and its alloys as examples of cryogenic focused ion beam milling of environmentally-sensitive materials*. Nature Communications, 2019. **10**.
 97. Hanlon, S.M., et al., *A solution to FIB induced artefact hydrides in Zr alloys*. Journal of Nuclear Materials, 2019. **515**: p. 122-134.
 98. Dolph, M.C. and C. Santeufemio, *Exploring cryogenic focused ion beam milling as a Group III-V device fabrication tool*. Nuclear Instruments and Methods in Physics Research Section B: Beam Interactions with Materials and Atoms, 2014. **328**: p. 33-41.
 99. McMinn, A., E.C. Darby, and J.S. Schofield, *The Terminal Solid Solubility of Hydrogen in Zirconium Alloys*. Zirconium in the Nuclear Industry: Twelfth International Symposium, 2000.
 100. Zuzek, E., et al., *The H-Zr (hydrogen-zirconium) system*. Bulletin of Alloy Phase Diagrams, 1990. **11**(4): p. 385-395.
 101. Kim, S.-D., J.-S. Kim, and J. Yoon, *Phase analysis of hydride blister in zirconium alloy*. Journal of Alloys and Compounds, 2018. **735**: p. 2007-2011.
 102. Wang, X., et al., *New insight into the intrinsic instability of fcc ZrH₂ by energy-resolved local bonding analysis*. RSC Advances, 2016. **6**(23): p. 19150-19154.
 103. Sha, G., et al., *Hydrogen-induced decomposition of Zr-rich cores in an Mg₆Zn_{0.6}Zr_{0.5}Cu alloy*. Acta Materialia, 2012. **60**(15): p. 5615-5625.

104. *Atom Probe Microscopy* | Baptiste Gault | Springer.
105. Ding, R. and I.P. Jones, *In situ hydride formation in titanium during focused ion milling*. Journal of Electron Microscopy, 2011. **60**(1): p. 1-9.
106. Wnuk, J.D., et al., *Electron Induced Surface Reactions of the Organometallic Precursor Trimethyl(methylcyclopentadienyl)platinum(IV)*. The Journal of Physical Chemistry C, 2009. **113**(6): p. 2487-2496.
107. Yan, F., et al., *Atomic-scale investigation of hydrogen distribution in a TiMo alloy*. Scripta Materialia, 2019. **162**: p. 321-325.
108. Carpenter, G.J.C., et al., *In Situ Hydride Formation in Zirconium and Titanium during Ion Milling*. Microscopy and Microanalysis, 1995. **1**(4): p. 175-184.
109. Carpenter, G.J.C., *The precipitation of γ -zirconium hydride in zirconium*. Acta Metallurgica, 1978. **26**(8): p. 1225-1235.
110. Lumley, S.C., et al., *The thermodynamics of hydride precipitation: the importance of entropy, enthalpy and disorder*. Acta Materialia, 2014. **79**: p. 351-362.
111. Kolli, R.P., *Controlling residual hydrogen gas in mass spectra during pulsed laser atom probe tomography*. Advanced Structural and Chemical Imaging, 2017. **3**(1).
112. Chang, Y., et al., *Characterizing solute hydrogen and hydrides in pure and alloyed titanium at the atomic scale*. Acta Materialia, 2018. **150**: p. 273-280.
113. Sato, H. and S. Zaefferer, *A study on the formation mechanisms of butterfly-type martensite in Fe-30% Ni alloy using EBSD-based orientation microscopy*. Acta Materialia, 2009. **57**(6): p. 1931-1937.
114. Şahin, O., et al., *Mechanical characterization for β -Sn single crystals using nanoindentation tests*. Materials Characterization, 2008. **59**(4): p. 427-434.
115. Chudoba, T. and F. Richter, *Investigation of creep behaviour under load during indentation experiments and its influence on hardness and modulus results*. Surface and Coatings Technology, 2001. **148**(2): p. 191-198.
116. Kölemen, U., *Analysis of ISE in microhardness measurements of bulk MgB₂ superconductors using different models*. Journal of Alloys and Compounds, 2006. **425**(1): p. 429-435.

117. Nix, W.D. and H. Gao, *Indentation size effects in crystalline materials: A law for strain gradient plasticity*. Journal of the Mechanics and Physics of Solids, 1998. **46**(3): p. 411-425.
118. Sadrabadi, P., K. Durst, and M. Göken, *Study on the indentation size effect in CaF₂: Dislocation structure and hardness*. Acta Materialia, 2009. **57**(4): p. 1281-1289.
119. Franke, O., J.C. Trenkle, and C.A. Schuh, *Temperature dependence of the indentation size effect*. Journal of Materials Research, 2010. **25**(7): p. 1225-1229.
120. Song, Ho G., J. John W. Morris, and F. Hua, *Anomalous Creep in Sn-Rich Solder Joints*. MATERIALS TRANSACTIONS, 2002. **43**(8): p. 1847-1853.
121. Reinikainen, T. and J. Kivilahti, *Deformation behavior of dilute SnBi(0.5 to 6 at. pct) solid solutions*. Metallurgical and Materials Transactions A, 1999. **30**(1): p. 123-132.
122. Bonar, L.G. and G.B. Craig, *Activation Energy for Creep of Tin*. Canadian Journal of Physics, 1958. **36**(11): p. 1445-1449.
123. Saad, G., F. Abd El-Salam, and M.T. Mostafa, *Dependence of creep rate on grain diameter in Sn-0.5at.%Bi alloy*. Surface Technology, 1984. **22**(1): p. 73-79.
124. Abd El-Rehim, A.F., *Effect of grain size on the primary and secondary creep behavior of Sn-3 wt.% Bi alloy*. Journal of Materials Science, 2008. **43**(4): p. 1444-1450.
125. Khalifa, B.A., M.R. Nagy, and R. Afify, *Microstructure changes and steady state creep characteristics in the superplastic Sn-5wt.% Bi alloy during transition*. Egypt Journal of Solids, 2006. **29**(1): p. 101-119.
126. Abd El-Rehim, A.F., *Effect of structure transformation on the creep characteristics of Sn-3wt% Bi alloy*. Journal of Alloys and Compounds, 2007. **440**(1): p. 127-131.
127. Oliver, W.C. and G.M. Pharr, *An improved technique for determining hardness and elastic modulus using load and displacement sensing indentation experiments*. Journal of Materials Research, 1992. **7**(6): p. 1564-1583.
128. Phani, P.S. and W.C. Oliver, *A direct comparison of high temperature*

- nanoindentation creep and uniaxial creep measurements for commercial purity aluminum*. Acta Materialia, 2016. 111: p. 31-38.
129. Fujiwara, M. and M. Otsuka, *Indentation creep of β -Sn and Sn-Pb eutectic alloy*. Materials Science and Engineering: A, 2001. 319-321: p. 929-933.
 130. Marques, V.M.F., et al., *Nanomechanical characterization of Sn-Ag-Cu/Cu joints—Part 2: Nanoindentation creep and its relationship with uniaxial creep as a function of temperature*. Acta Materialia, 2013. 61(7): p. 2471-2480.
 131. Mohamed, F.A. and T.G. Langdon, *Creep behaviour in the superplastic Pb-62% Sn eutectic*. The Philosophical Magazine: A Journal of Theoretical Experimental and Applied Physics, 1975. 32(4): p. 697-709.
 132. Sreejith, P.S. and B.K.A. Ngoi, *Material removal mechanisms in precision machining of new materials*. International Journal of Machine Tools and Manufacture, 2001. 41(12): p. 1831-1843.
 133. Cho, B.-J., et al., *On the mechanism of material removal by fixed abrasive lapping of various glass substrates*. Wear, 2013. 302(1): p. 1334-1339.
 134. Tanaka, H., et al., *Mechanical Characterization of Lapping Plate Materials in Diamond Charging Process*. Advanced Materials Research, 2010.
 135. Gagliardi, J.J., et al., *A case for 2-body material removal in prime LED sapphire substrate lapping and polishing*. Journal of Manufacturing Processes, 2013. 15(3): p. 348-354.
 136. Mayén-Mondragón, R., et al., *Statistical characterization of the lapping plate surface morphology evolution in a diamond charging process*. Measurement Science and Technology, 2008. 19(6): p. 065706.



จุฬาลงกรณ์มหาวิทยาลัย
CHULALONGKORN UNIVERSITY

VITA

NAME	เชษฐวิภาดา ยิบยีนธรรม
DATE OF BIRTH	8 ตุลาคม 2530
PLACE OF BIRTH	กรุงเทพ



จุฬาลงกรณ์มหาวิทยาลัย
CHULALONGKORN UNIVERSITY



จุฬาลงกรณ์มหาวิทยาลัย
CHULALONGKORN UNIVERSITY